INFN ISTITUTO NAZIONALE DI FISICA NUCLEARE
Laboratori Nazionali di Frascati

FRASCATI PHYSICS SERIES

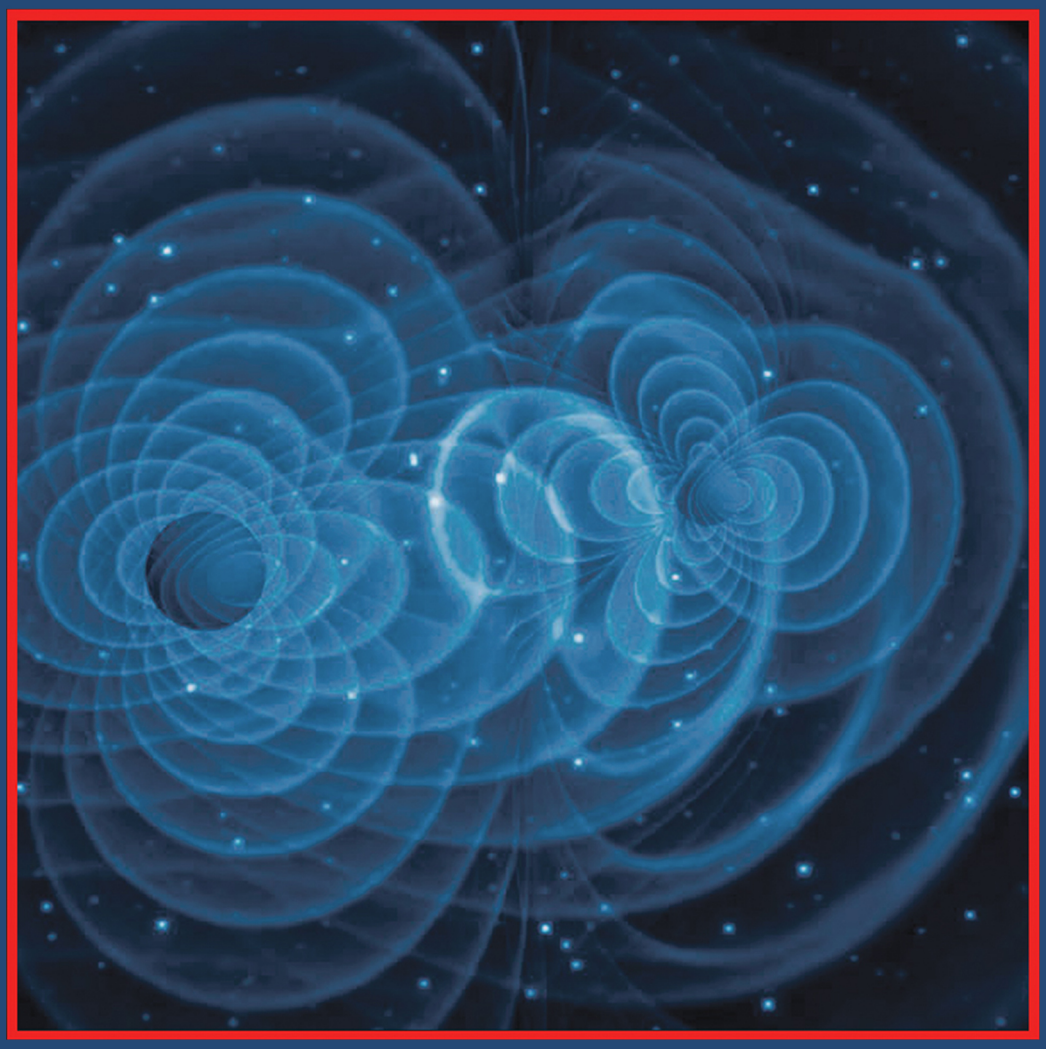

Sixth Young Researcher Workshop "Physics Challenges in the LHC Era" 2018

Editor:

Gennaro Corcella

FRASCATI PHYSICS SERIES

Series Editor
Paola Gianotti

Technical Editor
Lia Sabatini

Cover by Claudio Federici

Volume LXVII

Istituto Nazionale di Fisica Nucleare – Laboratori Nazionali di Frascati
Divisione Ricerca
Ufficio Biblioteca e Documentazione Scientifica
P.O. Box 13, I-00044 Frascati Roma Italy
email: library@lists.lnf.infn.it

ISBN 978-88-86409-68-1

Sixth Young Researcher Worshop
"Physics Challenges in the LHC Era"
May 2018

PREFACE

The Sixth Young Researcher Workshop 'Physics Challenges in the LHC Era' took place on May 7th and 10th, 2018, during the XIX edition of the Spring School 'Bruno Touschek' in Nuclear, Subnuclear and Astroparticle Physics, which was held at INFN, Laboratori Nazionali di Frascati (LNF).

The LNF Young Researcher Workshop series started in 2009 and has now become an appointment where graduate students and young postdocs in theoretical and experimental physics have a pretty unique opportunity to present their work to an audience made of both junior and experienced researchers.

The 2018 edition featured talks of very high quality, covering a wide spectrum of topics. From the experimental viewpoint, we had presentations on the KLOE and PADME experiments at LNF, the Mu2e project at Fermilab, the ATLAS apparatus at the Large Hadron Collider (CERN), and even talks on the applications of cyclotrons and detectors to medical physics and on the Italian-Chinese space mission CSES. From the theory side, we heard of the phenomenology of dark photons, leptonic dipole moments, QCD axions in flavour models, unintegrated gluon distributions in the proton. Most of the talks have been summarized in the contributions published in these proceedings, which often represent, especially for the youngest students, the first peer-reviewed publication in their career as a sole author.

Before concluding, I wish to warmly thank all co-organizers of the XIX LNF Spring School, the School secretary, the lecturers and, above all, the fellows who gave presentations and livened up the Young Researcher Workshop.

Frascati, October 5, 2018

Gennaro Corcella
(Chairman of the 6th Young Researcher Workshop)

CONTENTS

Frascati Physics Series Vol. 67 (2018)
6th Young Researcher Workshop 'Physics Challenges in the LHC Era'
May 7 and 10, 2018

THE KLOE-2 EXPERIMENT AT DAΦNE

Xiaolin Kang on behalf of the KLOE-2 Collaboration
INFN - Laboratori Nazionali di Frascati, Via E. Fermi 40, 00044 Frascati (RM), Italy
E-mail: Xiaolin.Kang@lnf.infn.it

Abstract

From November 2014 to March 2018, the KLOE-2 experiment has collected more than 5 fb^{-1} of data at DAΦNE. The experiment has a wide physics program ranging from tests of discrete symmetries and studies of light unflavored mesons to searches for light-mass dark-matter candidates and $\gamma\gamma$ physics. In this report, an overview including the performances of the KLOE-2 detector, the data-taking conditions and some of the ongoing analyses, including the measurement of the $K_S \to \pi e \nu$ charge asymmetry and the running QED coupling constant, will be given.

1 Introduction

The KLOE-2 experiment, operated at the INFN e^+e^- DAΦNE ϕ factory, is a continuation of the KLOE [1] experiment with the inclusion of some new sub-detectors allowing for a larger physics program. From November 2014 to March 2018, the KLOE-2 detector has completed its data-taking campaign and collected ∼5.5 fb^{-1} at the ϕ meson peak. The record performance of $2.38 \times 10^{32} cm^{-2} s^{-1}$ peak luminosity and 14.3 pb^{-1} maximum daily delivered integrated luminosity have been achieved with the innovative crab-waist collision scheme. While the best daily integrated luminosity collected by KLOE-2 is 11.9 pb^{-1}. Full time evolution of data delivery and collection is shown in Fig. 1.

The experiment has a wide physics program [2] ranging from tests of discrete symmetries, CKM tests and studies of light unflavored mesons decays to searches for dark-matter candidates with light masses and gamma-gamma physics exploiting dedicated taggers, and search for physics beyond the Standard Model. The KLOE-2 data sample, together with the KLOE one, sums up to ∼ 8 fb^{-1} acquired data, corresponding to 2.4×10^{10} ϕ decays, which allow the accurate analysis of several decays, in particular the tests of the CPT symmetry and of quantum coherence, using entangled neutral kaons with an unprecedented precision.

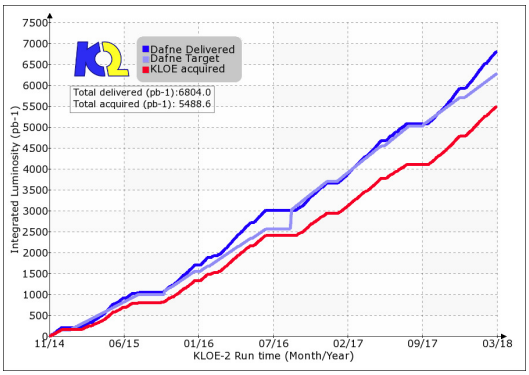

Figure 1: *Time evolution of the DAΦNE data delivery during the KLOE-2 data-taking campaign. The dark blue line represent the integrated luminosity delivered, the light blue line represent the target luminosity fixed to achieve KLOE-2 goal of 5 fb^{-1} by the end of KLOE-2 physics run, while the red curve is the corresponding amount of integrated luminosity acquired.*

2 The KLOE-2 Detector

The original KLOE detector is composed of a large cylindrical drift chamber (DC) [3] surrounded by a lead-scintillating fiber electromagnetic calorimeter (EMC) [4]. The DC has a momentum resolution of $\sigma_{P\perp}/P_\perp \sim 0.4\%$ for tracks with polar angle $\theta > 45°$ and a spatial resolution of $\sim$0.15 mm in $r-\phi$ and $\sim$ 2 mm in z. The EMC has a energy resolution of $\sigma_E/E \sim 5.7\ \%/\sqrt{E}$ (GeV) and an excellent time resolution of $\sigma_t \sim 54(ps)/\sqrt{E}(\mathrm{GeV})\oplus 100\ ps$. A superconducting coil around the EMC provides a 0.52 T axial magnetic field.

The following upgrades have been made for the KLOE-2 detector. Two pairs of electron-positron taggers have been installed for $\gamma\gamma$ physics: a small LYSO crystal calorimeter matrix, the Low Energy Tagger (LET) inside the KLOE-2 apparatus and a plastic scintillator hodoscope, the High Energy Tagger (HET), along the beam lines outside KLOE-2 detector. To increase the acceptance two new calorimeters have been developed. A pair of LYSO crystal calorimeters (CCALT) have been installed near the interaction region to cover the low-θ range. A pair of tile calorimeters (QCALT) cover the quadrupoles inside the KLOE-2 detector and along the beam pipe to improve the angular coverage for particles coming from the active volume of the DC (e.g. K_L decay). A multilayer cylindrical GEM tracker (Inner Tracker, IT) has been installed to improve the vertex reconstruction capabilities near the interaction region. This is the first use of the GEM technology with a cylindrical geometry in a high-energy experiment.

3 Charge asymmetry for $K_S \to \pi e\nu$

The semileptonic decays of K_S are a powerful tool in the study of discrete symmetries [5]. In particular the charge asymmetries for physical states K_S and K_L can be defined as:

$$A_{S,L} = \frac{\Gamma(K_{S,L} \to \pi^- e^+ \nu) - \Gamma(K_{S,L} \to \pi^+ e^- \bar{\nu})}{\Gamma(K_{S,L} \to \pi^- e^+ \nu) + \Gamma(K_{S,L} \to \pi^+ e^- \bar{\nu})}. \quad (1)$$

They are sensitive to CP and CPT violation effects. At first order they can be expressed as [6]:

$$A_{S,L} = 2[Re(\epsilon_K) \pm Re(\delta_K) - Re(y) \pm Re(x_-)], \quad (2)$$

with $Re(\epsilon_K)$ and $Re(\delta_K)$ implying T and CPT violation in the $K^0 - \bar{K^0}$ mixing, respectively, $Re(y)$ and $Re(x_-)$ implying CPT violation in $\Delta S = \Delta Q$ and $\Delta S \neq \Delta Q$ decay amplitudes [7], respectively, and all parameters implying CP violation. If the CPT symmetry holds then the two asymmetries are expected to be identical $A_S = A_L = 2Re(\epsilon_K) \simeq 3 \times 10^{-3}$, and each of them accounts for the CP impurity in the mixing physical state.

The difference and sum of A_S and A_L allow to test possible violations of the CPT symmetry, either in the decay amplitudes or in the mass matrix. The measurement of the difference $A_S - A_L = 4[Re(\delta_K) + Re(x_-)]$ is of particular importance as a test of CPT. Violation effects in a quantum gravity scenario and their observation would definitely constitute an unambiguous signal of a New Physics framework. The sum $A_S + A_L = 4[Re(\epsilon_K) - Re(y)]$ can be used to extract the CPT-violating parameter $Re(y)$ once the measured value of $Re(\epsilon_K)$ is provided as input.

At present, the most precise measurement of A_L has been performed by the KTeV collaboration, which gives $A_L = (3.322 \pm 0.058_{stat} \pm 0.047_{syst}) \times 10^{-3}$ [8]. While the first measurement of A_S has been performed by the KLOE collaboration with a data sample corresponding to about 410 pb^{-1} of data, which gives $A_S = (1.5 \pm 9.6_{stat} \pm 2.9_{syst}) \times 10^{-3}$ [9], KLOE-2 updated this analysis recently using a 1.63 fb^{-1} data sample collected at the ϕ resonance peak [10].

The charge asymmetry for the short-lived kaon can be defined by:

$$A_S = \frac{N^+/\epsilon^+ - N^-/\epsilon^-}{N^+/\epsilon^+ + N^-/\epsilon^-}, \tag{3}$$

where N^+ and N^- are the number of $K_S \to \pi^- e^+ \nu$ and $K_S \to \pi^+ e^- \bar{\nu}$ decays, respectively, while ϵ^+ and ϵ^- are the corresponding analysis efficiencies, estimated using Monte Carlo (MC) simulations and the $K_L \to \pi e \nu$ control sample.

The signal yields are estimated by fitting the $M^2(e)$ data distributions [1] with the superposition of the corresponding simulated ones for signal and background with free normalization and accounting for a finite size of the Monte Carlo sample. The comparison of the $M^2(e)$ distributions are shown in Fig. 2. The fits yield 34579 ± 251 $K_S \to \pi^- e^+ \nu$ and 36874 ± 255 $K_S \to \pi^+ e^- \bar{\nu}$ events, respectively, which corresponds to $A_S = (-4.8 \pm 5.7_{stat} \pm 2.6_{syst}) \times 10^{-3}$.

Due to the similar analysis schemes, parts of the systematical uncertainty of both KLOE measurements related to the applied cuts are correlated. Taking this information into account, the combined result of the reported measurement and previous results is: $A_S = (-3.7 \pm 5.0_{stat} \pm 2.6_{syst}) \times 10^{-3}$, which should supersede the previous KLOE measurements [9].

Using the A_L and $Re(\delta_K)$ measurements from PDG ($Re(\delta_K) = (2.51 \pm 2.25) \times 10^{-4}$) [11] and the KLOE measurement of $Re(\epsilon_K)$ ($Re(\epsilon_K) = (1.596 \pm 0.013) \times 10^{-3}$) [12], the $Re(x_-)$ and $Re(y)$ parameters can be extracted:

$$Re(x_-) = (-2.0 \pm 1.4) \times 10^{-3},$$

$$Re(y) = (1.7 \pm 1.4) \times 10^{-3},$$

which are in agreement with previous results and are the most precise results to date. Improvements are expected in the future with the analysis of the additional 5.5 fb^{-1} collected by KLOE-2.

[1] For decays $K \to \pi e \nu$, $M^2(e)$ is defined as $M^2(e) = [E(K) - E(\pi) - E(\nu)]^2 - |\vec{p}(e)|^2$, with $E(\nu) = |\vec{p}(K) - \vec{p}(e) - \vec{p}(\pi)|$.

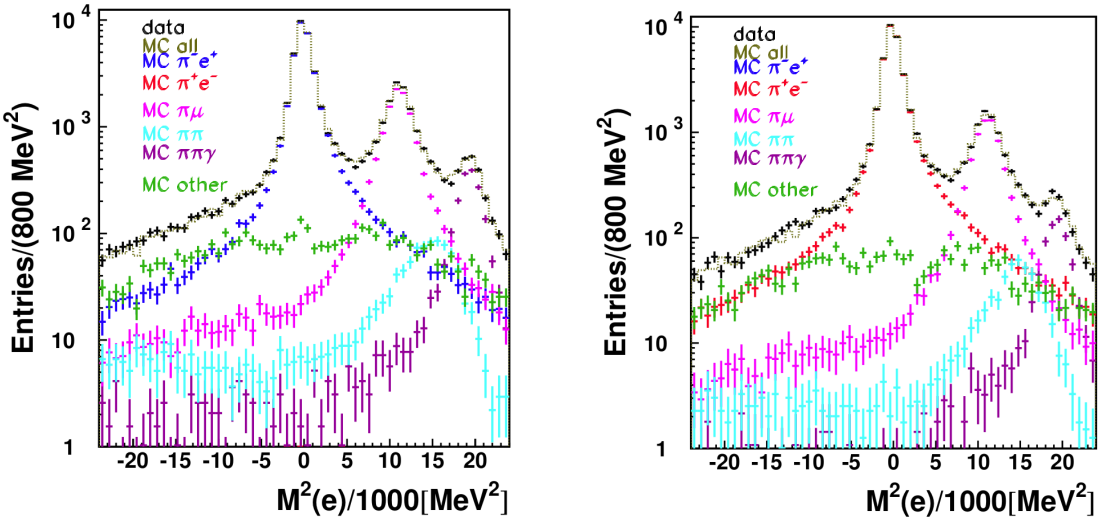

Figure 2: *Data (black points) and MC simulation of the $M^2(e)$ variable for both final charge states ($\pi^+e^-\bar{\nu}$-left plot and $\pi^-e^+\nu$-right plot).*

4 Measurement of the running $\alpha_{em}(s)$

The QED coupling constant is predicted and observed [13] to increase with rising momentum transfer, which can be understood as a result of the screening of the bare charge caused by the polarized cloud of virtual particles. The vacuum-polarization (VP) effects can be absorbed in a redefinition of the fine-structure constant, making it s dependent:

$$\alpha(s) = \frac{\alpha(0)}{1 - \Delta\alpha(s)}, \tag{4}$$

where s is the momentum transfer squared of the reaction. The shift $\Delta\alpha(s)$ in terms of the vacuum polarization function $\Pi'_\gamma(s)$ is a sum of the lepton (e, μ, τ) contributions, the contribution from the five quark flavors (u, d, s, c, b), and the contribution of the top quark (which can be neglected at low energies) [14]. The leptonic contributions can be calculated with very high precision in QED using perturbation theory [15]. However, due to the non-perturbative behavior of the strong interaction at low energies, perturbative QCD only allows one to calculate the high-energy tail of the hadronic (quark) contributions. In the lower-energy region the hadronic contribution can be evaluated through a dispersion integral over the measured $e^+e^- \to$ hadrons cross-section:

$$\Delta\alpha_{had}(s) = -\frac{\alpha(0)s}{3\pi} Re \int_{m_\pi^2}^{\infty} ds' \frac{R_{had}(s')}{s'(s' - s - i\epsilon)}, \tag{5}$$

where $R_{had}(s)$ is defined as the cross section ration $R_{had}(s) = \frac{e^+e^- \to \gamma^* \to hadrons}{e^+e^- \to \gamma^* \to \mu^+\mu^-}$.

Based on an integrated luminosity of 1.7 fb^{-1} data sample collected at the ϕ-meson mass, the analysis yields a measurement of the running of the effective QED coupling constant $\alpha(s)$ in the time-like region $0.6 < \sqrt{s} < 0.975$ [16]. The strength of the coupling constant is measured as a function of the momentum transfer of the exchanged photon $\sqrt{s} = M_{\mu\mu}$, where $M_{\mu\mu}$ is the $\mu^+\mu^-$ invariant mass. The value of $\alpha(s)$ is extracted from the ratio of the measured differential cross section for the process

$e^+e^- \to \mu^+\mu^-\gamma(\gamma)$, with the photon emitted in the initial state (ISR), with respect to the corresponding cross section obtained from MC simulations, with the coupling set to the constant value $\alpha(s) = \alpha(0)$:

$$\left|\frac{\alpha(s)}{\alpha(0)}\right|^2 = \frac{d\sigma_{data}(e^+e^- \to \mu^+\mu^-\gamma(\gamma))|_{ISR}/d\sqrt{s}}{d\sigma^0_{MC}(e^+e^- \to \mu^+\mu^-\gamma(\gamma))|_{ISR}/d\sqrt{s}}. \quad (6)$$

The experimental ISR $\mu^+\mu^-\gamma$ cross section is obtained from the observed number of events (N_{obs}) and the background estimate (N_{bckg}) as:

$$\frac{d\sigma_{data}(e^+e^- \to \mu^+\mu^-\gamma(\gamma))}{d\sqrt{s}}|_{ISR} = \frac{N_{obs} - N_{bckg}}{\Delta\sqrt{s}} \cdot \frac{(1-\delta_{FSR})}{L \cdot \epsilon(\sqrt{s})}, \quad (7)$$

where $(1-\delta_{FSR})$ is the correction applied to remove the final-state radiative (FSR) contribution, L is the integrated luminosity and ϵ is the detection efficiency, which is estimated from $\mu^+\mu^-\gamma$ MC simulations.

From Eqs. 6 and 7 the running of the effective QED coupling constant $\alpha(s)$ can be extracted. By setting in the MC generator the electromagnetic coupling to the constant value $\alpha(0)$, the hadronic contribution to the photon propagator, with its characteristic $\rho - \omega$ interference structure, is clearly visible in the data-to-MC ratio, as shown in Fig. 3, together with the prediction from the alphaQED code [17]. For comparison, the prediction with constant coupling (no running) and with only lepton pairs contributing to the running of $\alpha(s)$ is given.

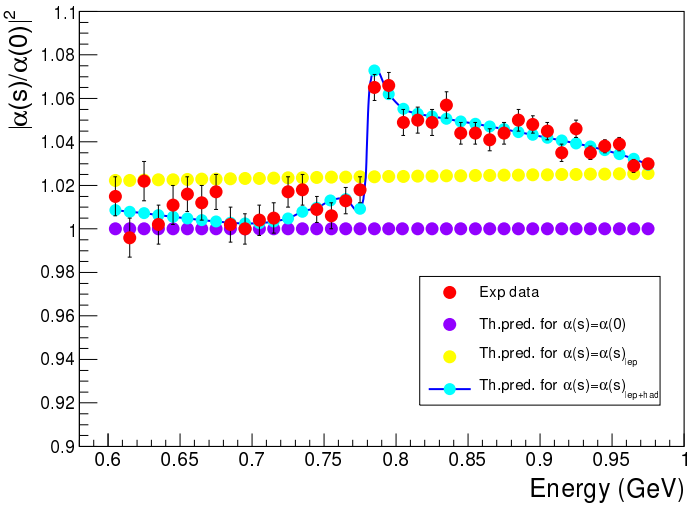

Figure 3: *The square of the modulus of the running $\alpha(s)$ in units of $\alpha(0)$ compared with the prediction as a function of the dimuon invariant mass. The red points are the KLOE data with statistical errors; the violet points are the theoretical prediction for a fixed coupling $\alpha(s) = \alpha(0)$; the yellow points are the prediction with only virtual lepton pairs contributing to the shift $\Delta\alpha(s) = \Delta\alpha(s)_{lep}$, and finally the points with the solid lines are the full QED prediction with both lepton and quark pairs contributing to the shift $\Delta\alpha(s) = \Delta\alpha(s)_{lep+had}$.*

In the contribution to the running of α, the imaginary part is usually neglected. This is a good approximation as the contribution from the imaginary part of $\Delta\alpha$ enters at order $O(\alpha^2)$ compared to $O(\alpha)$ for the real part, and is suppressed [18]. However, the imaginary part should be taken into account in the presence of resonances like the ρ meson, where the cross section is measured with an accuracy better than 1%. The imaginary part of the shift $\Delta\alpha(s)$ can be related to the total cross section $\sigma_{tot}(e^+e^- \to$

$\gamma^* \to anything$), via the precise relation $Im(\Delta\alpha) = -\frac{\alpha}{3}R(s)$, with $R(s) = \sigma_{tot}/[4\pi|\alpha(s)|^2]/(3s)$. In the energy region around the ρ-meson, the hadronic cross section are dominant by the $\pi\pi$ contribution. Then the real part can be extracted as $Re(\Delta\alpha(s)) = 1 - \sqrt{|\alpha(s)/\alpha(0)|^2 - (Im\Delta\alpha)^2}$. The extracted results are shown in Fig. 4 and compared with the prediction provided by the alphaQED package for $\Delta\alpha = \Delta\alpha_{lep}$ and $\Delta\alpha = \Delta\alpha_{lep+had}$.

By fitting $Re(\Delta\alpha)$ with the sum of the leptonic and hadronic contributions, which is parametrized as a sum of the $\rho(770)$, $\omega(782)$ and $\phi(1020)$ resonance components and a non-resonant term, the branching ratio of $\omega \to \mu^+\mu^-$ is extracted:

$$BR(\omega \to \mu^+\mu^-) = (6.6 \pm 1.4_{stat} \pm 1.7_{syst}) \times 10^{-5},$$

which is comparable to the value $(9.0 \pm 3.1) \times 10^{-5}$ from PDG [11].

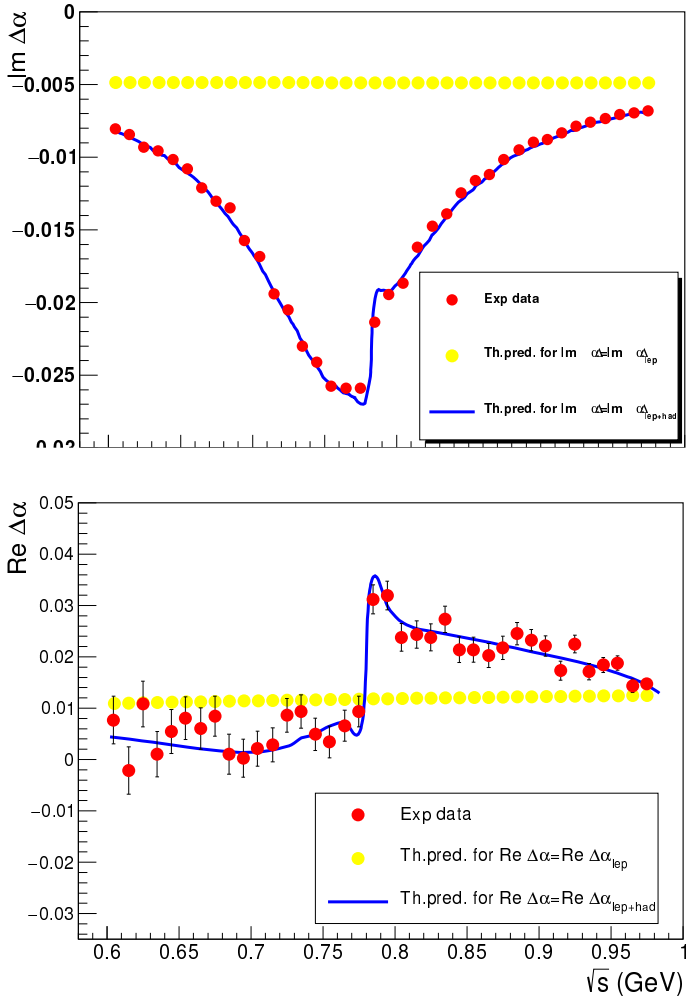

Figure 4: *The imaginary and real parts of $\Delta\alpha$ extracted from the KLOE data (red points) compared with the prediction provided by alphaQED when $\Delta\alpha = \Delta\alpha_{lep}$ (yellow points) and $\Delta\alpha = \Delta\alpha_{lep+had}$ (solid lines).*

5 Summary

Till March 2018, the KLOE/KLOE-2 experiments have completed their missions successfully and collected about 8 fb^{-1} of data at the ϕ-meson peak. Using the KLOE data, we have achieved many precision results on tests of discrete symmetries, studies of the light unflavored mesons, and searches for light-mass dark-matter candidates, which are planned to be extended with the KLOE-2 higher statistics.

6 Acknowledgements

We warmly thank our former KLOE colleagues for the access to the data collected during the KLOE data-taking campaign. We thank the DAΦNE team for its effort in maintaining low-background running conditions and their collaboration during all data taking. We want to thank our technical staff: G.F. Fortugno and F. Sborzacchi for their dedication in ensuring efficient operation of the KLOE computing facilities; M. Anelli for his continuous attention to the gas system and detector safety; A. Balla, M. Gatta, G. Corradi and G. Papalino for electronics maintenance; C. Piscitelli for his help during major maintenance periods. This work was supported in part by the Polish National Science Centre through the Grants No. 2013/11/B/ST2/04245, 2014/14/E/ST2/00262, 2014/12/S/ST2/00459, 2016/21/N/ST2/01727, 2016/23/N/ST2/01293, 2017/26/M/ST2/00697.

References

1. The KLOE Collaboration, The KLOE Detector Technical Proposal, LNF-93/002, 1993; S. Bertolucci (KLOE Collaboration), A Status Report of KLOE at DAΦNE, in Proc. 19th International Symposium on Lepton and Photon Interactions at High Energies, Stanford, USA, 1999, hep-ex/0002030.
2. G. Amelino-Camelia *et al* (KLOE Collaboration), Eur. Phys. J. **C 68**, 619 (2010); https://agenda.infn.it/conferenceDisplay.py?confId=11722.
3. M. Adinolfi *et al* (KLOE Collaboration), Nucl. Instrum. Methods **A 488**, 51 (2002).
4. M. Adinolfi *et al* (KLOE Collaboration), Nucl. Instrum. Methods **A 482**, 364 (2002).
5. M. Hayakawa and A. I. Sanda, Phys. Rev. **D 48**, 1150 (1993).
6. L. Maiani *et al*, in The Second DAΦNE Physics Handbook, Istituto Nazionale di Fisica Nucleare, 1995.
7. F. Niebergall *et al*, Phys. Lett. **B 49**, 103 (1974).
8. A. Alavi-Harati *et al* (KTeV Collaboration), Phys. Rev. Lett. **88**, 181601 (2002).
9. F. Ambrosino *et al* (KLOE Collaboration), Phys. Lett. **B 636**, 173 (2006).
10. A. Anastasi *et al* (KLOE-2 Collaboration), waiting for submission.
11. M. Tanabashi *et al* (Particle Data Group), Phys. Rev. **D 98**, 030001 (2018).
12. F. Ambrosino *et al* (KLOE collaboration), J. High Energy Phys. **12**, 11 (2006).

13. A. B. Arbuzov, D. Haidt, C. Matteuzzi, M. Paganoni, L. Trentadue, Eur. Phys. J. **C 34**, 267 (2004);
G. Abbiendi *et al* (OPAL Collaboration), Eur. Phys. J. **C 45**, 1 (2006);
M. Acciarri *et al* (L3 Collaboration), Phys. Lett. **B 476**, 40 (2000);
S. Odaka *et al* (VENUS Collaboration), Phys. Rev. Lett. **81**, 2428 (1998);
I. Levine *et al* (TOPAZ Collaboration), Phys. Rev. Lett. **78**, 424 (1997).

14. F. Jegerlehner, J. Phys. G: Nucl. Part. Phys. **29**, 101 (2003).

15. M. Steinhauser, Phys. Lett. **B 429**, 158 (1998);
C. Sturm, Nucl. Phys. **B 874**, 698 (2013).

16. A. Anastasi *et al* (KLOE-2 Collaboration), Phys. Lett. **B 767**, 485 (2017).

17. F. Jegerlehner, alphaQED package [version April 2012]; See also F. Jegerlehner, Nuovo Cim. **C 034S1**, 31 (2011); F. Jegerlehner, Nucl. Phys. Proc. Suppl. **162**, 22 (2006).

18. S. Actis *et al*, Eur. Phys. J. **C 66**, 585 (2010).

Frascati Physics Series Vol. 67 (2018)
6th Young Researcher Workshop 'Physics Challenges in the LHC Era'
May 7 and 10, 2018

DARK MEDIATOR RESULTS IN KLOE/KLOE-2

Elena Pérez del Río
LNF-INFN Via E. Fermi 40, 00044 Frascati, Italy
for the KLOE-2 collaboration

Abstract

In the last years, searches for a fifth force to explain many astrophysical observations and the g-2 anomaly have been performed. The carrier of this force, a new boson also called *dark photon*, intermediary between the Dark Matter particles and the Standard Model, has been searched by the KLOE experiment by investigating the Phi-Dalitz decay into the eta meson, the direct production of the dark boson from continuum and the Higgsstrahlung process, where it is produced together with a *dark Higgs*. Constraints in the coupling strength of this new force have been set for a large mass range. The newest analysis combines the KLOE data to significantly improve the sensitivity in the mass region where the *dark photon* mixes with the rho meson. This work intends to serve as a small overview of the new KLOE searches for the dark photon, with an update in the coupling-constant limits from the combined analysis of the KLOE data. New analyses will profit from the KLOE-2 data, which will allow to improve the sensitivity of all exploited processes by a factor of 2. Moreover, new models are going to be investigated with the KLOE-2 sample, which has collected more than 5 fb^{-1} in the past 3 years.

1 Introduction

The Standard Model (SM), although being the most complete theoretical framework at present, does not provide a definitive model of all elementary particles. In particular, observations as the 511 keV gamma-ray signal from the galactic center [1], the CoGeNT results [2], the DAMA/LIBRA annual modulation [3, 4], the total e^+e^- flux [5, 6, 7, 8] and the muon magnetic discrepancy a_μ are examples of possible physics beyond the SM. Extensions of the SM [9, 10, 11, 12, 13] claim to explain the afore-mentioned anomalies by means of dark matter models, with a Weakly Interacting Massive Particle (WIMP) belonging to a secluded gauge sector. The new gauge interaction would be mediated by a new

vector gauge boson, the U boson or dark photon, which could interact with the photon via a kinetic-mixing term ϵ^2. A U boson, with mass of $\mathcal{O}(1\text{GeV})$ and ϵ in the range of $10^{-2} - 10^{-7}$, could be observed in e^+e^- colliders via different processes: $e^+e^- \to U\gamma$, $V \to P\gamma$ decays, where V and P are vector and pseudoscalar mesons, and $e^+e^- \to h'U$, where h' is a Higgs-like particle responsible for the breaking of the hidden symmetry. In the following, many of these searches, carried out with the KLOE detector, are described.

2 The KLOE detector at DAϕNE

The KLOE detector experiment operates in Frascati, at the DAΦNE ϕ-factory [14]. It consists of three main parts, a cylindrical drift chamber (DC) [15] surrounded by an electromagnetic calorimeter (EMC) [16], all embedded in a magnetic field of 0.52 T, provided along the beam axis by a superconducting coil located around the calorimeter. The EMC energy and time resolutions are $\sigma_E/E = 5.7\%/\sqrt{E[\text{GeV}]}$ and $\sigma_t(E) = 57$ ps$/\sqrt{E[\text{GeV}]} \oplus 100$ ps, respectively. The EMC consist of a barrel and two end-caps of lead/scintillating fibers, which cover 98% of the solid angle. The all-stereo drift chamber, 4m in diameter and 3.3m long, operates with a light gas mixture (90% helium, 10% isobutane). The position resolutions are $\sigma_{xy} \sim 150$ μm and $\sigma_z \sim 2$ mm. The momentum resolution $\sigma_{p\perp}/p_\perp$ is better than 0.4% for large-angle tracks.

3 U-boson search in $e^+e^- \to U\gamma$ with $U \to \mu^+\mu^-$

The U boson was also searched in the process $e^+e^- \to U\gamma$ with $U \to \mu^+\mu^-$, in a sample of 239.3 pb^{-1} of data collected in 2002 [22]. The expected signal would show up as a narrow resonance in the di-muon mass spectrum.

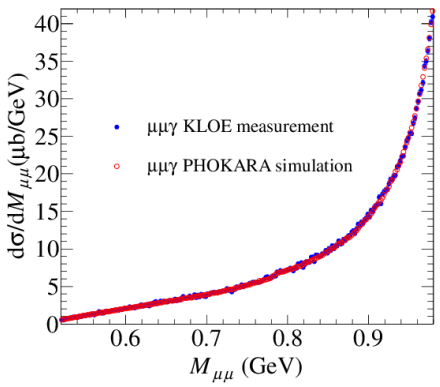

Figure 1: Di-muon invariant mass distributions $M_{\mu\mu}$. Comparison of data (full blue circles) and simulation (open red circles).

Since no resonant peak was observed (see Fig. 1), the so-called CLs technique was used to estimate the number of U-boson signal events excluded at 90% confidence level, N_{CLs} and then the limit on the kinetic mixing parameter,

$$\epsilon^2 = \frac{\alpha_D}{\alpha_{EM}} = \frac{N_{CLs}}{\epsilon_{eff}} \frac{1}{H \times I \times L_{integrated}}, \tag{1}$$

where ϵ_{eff} is the overall efficiency, I is the effective cross section, $L_{integrated}$ the integrated luminosity and H is the radiator function, which is extracted from the differential cross section, $d\sigma_{\mu\mu\gamma}/dM_{\mu\mu}$. A systematic uncertainty of about 2% was estimated. The 90% confidence level limit is shown in Fig. 3

4 U-boson search in $e^+e^- \to U\gamma$ with $U \to e^+e^-$

The study of the reaction $e^+e^- \to U\gamma$, $U \to e^+e^-$, is similar to the previously described analysis but with the characteristic that allows to investigate the low mass region close to the di-electron mass threshold [23].

The Fig. 2 compares the di-electron invariant mass with BABAYAGA-NLO Monte Carlo (MC) simulation [24], modified to allow the Bhabha radiative process to proceed only via the annihilation channel, in which the U-boson signal would possibly occur, showing an excellent agreement.

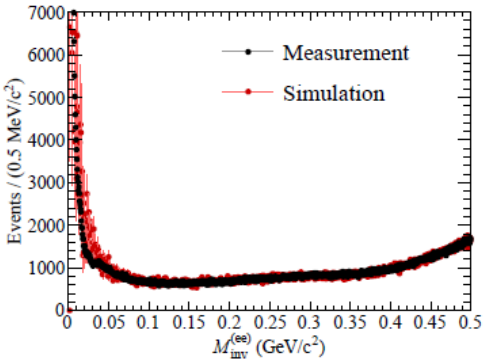

Figure 2: Di-electron invariant-mass distribution, M_{ee}, for the process $e^+e^- \to e^+e^-\gamma$ (black circles) compared to the MC simulated spectra (red circles).

The upper limit of the kinetic-mixing parameter as a function of m_U was evaluated with the CLs technique in an analogous way as the $e^+e^- \to \mu^+\mu^-\gamma$. The limit on the U-boson signal was evaluated at 90% confidence level and the limit on the kinetic parameter was calculated using equation (1). In this case the selection efficiency amounts to $\epsilon_{eff} \sim 1.5 - 2.5\%$ and the integrated luminosity corresponds to $L_{integrated} = 1.54\,\mathrm{fb}^{-1}$ from the 2004-2005 data campaign.

5 U-boson search in $e^+e^- \to h'U$ with $U \to \mu^+\mu^-$

A natural consequence of the massiveness of the U boson is the breaking of the U_D hidden symmetry according to a Higgs-like mechanism through an additional scalar particle, called h' or dark Higgs. The production cross section of the dark Higgsstrahlung process, $e^+e^- \to h'U$ with $U \to \mu^+\mu^-$, would be proportional to the product $a_D \times \epsilon^2$ [25]. Depending on the relative masses of the h' and the U boson there are two possible decay scenarios: if $m_{h'} > 2m_U$, the dark Higgs could decay via $h' \to UU \to 4l, 4\pi, 2l+2\pi$, where l denotes lepton. This scenario was studied by BaBar [26] and Belle [27] in recent experiments. If $m_{h'} < 2m_U$, then the dark Higgs would have a large lifetime and would escape any detection. This 'invisible' dark Higgs scenario has been the object of study by KLOE [28].

The analysis was performed on $1.65\,\mathrm{fb}^{-1}$ of data collected during 2004-2005 data campaign at a center of mass energy at the ϕ-peak, and on a data sample of $0.2\,\mathrm{fb}^{-1}$ at a center of mass energy of $\sim 1000\,\mathrm{MeV}$. The expected signal would show up as a sharp enhancement in the missing mass M_{miss}

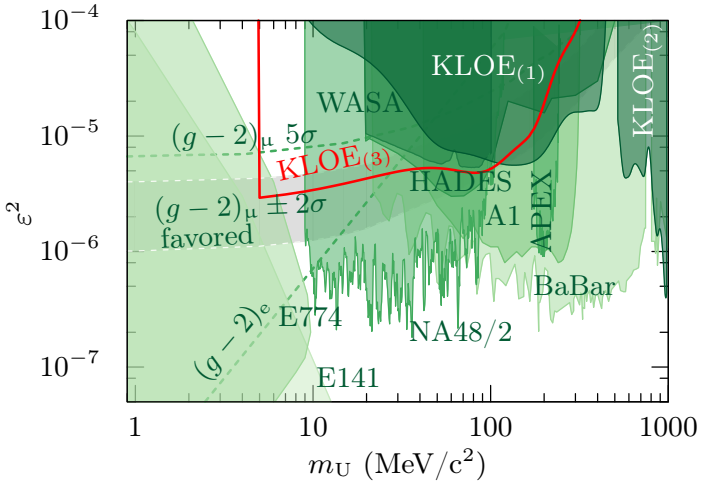

Figure 3: Exclusion limits on the kinetic-mixing parameter, ϵ^2, from KLOE (in red): KLOE$_1$, KLOE$_2$ and KLOE$_3$ correspond to the combined limits from the analysis of $\phi \to \eta e^+e^-$, $e^+e^- \to \mu^+\mu^-\gamma$ and $e^+e^- \to e^+e^-\gamma$, respectively. The results are compared with the limits from E141, E774 [29], MAMI/A1 [30], APEX [31], WASA [32], HADES [33], NA48/2 [34] and BaBar [35]. The grey band indicates the parameter space favored by the ($g_\mu - 2$) discrepancy.

versus the $\mu\mu$ invariant mass $M_{\mu\mu}$. No signal of the dark Higgsstrahlung process was observed and a Bayesian limit on the number of signal events, $N_{90\%}$, was derived for both samples separately. The product $\alpha_D \times \epsilon^2$ was then calculated according to

$$\alpha_D \times \epsilon^2 = \frac{N_{90\%}}{\epsilon_{eff}} \frac{1}{\sigma_{h'U}(\alpha_D\epsilon^2 = 1) \times L_{integrated}}, \tag{2}$$

with

$$\sigma_{h'U} \propto \frac{1}{s} \frac{1}{(1 - m_U^2/s)^2} \tag{3}$$

and where $\alpha_D \times \epsilon^2$ is assumed to be equal 1. A conservative 10% of systematic uncertainty was considered. The combined 90% confidence level limits for both on- and off-peak data samples are presented in Fig. 4, as a function of m_U (left) and of $m_{h'}$ (right). The limit values of $\alpha_D \times \epsilon^2$ of $10^{-9} - 10^{-8}$ at 90% confidence level translate into a limit on the kinetic parameter ϵ^2 of $10^{-6} - 10^{-8}$ ($\alpha_D = \alpha_{EM}$).

6 U-boson search in $e^+e^- \to U\gamma$ with $U \to \pi^+\pi^-$

The leptonic channels investigated previously lose sensitivity in the $\rho - \omega$ region due to the dominant branching fraction into hadrons. The effective coupling of the U boson is predicted to be given by the product of the virtual-photon coupling and the kinetic-mixing parameter $\epsilon^2 e F_\pi(q^2)$ [21]. The signal of the U boson would be then expected as a resonant peak in the di-pion invariant mass spectrum with initial state radiation (ISR) $\pi^+\pi^-\gamma$ events. For this search, a total integrated luminosity of 1.93 fb^{-1} was analyzed [36].

A very good description of the $\rho - \omega$ interference was achieved by a dedicated PHOKARA MC simulation including the Gounaris–Sakhurai pion form factor parameterization in Ref. [37]. In Fig. 5 one can observe the good agreement between MC predictions and data in the interference region, as well as

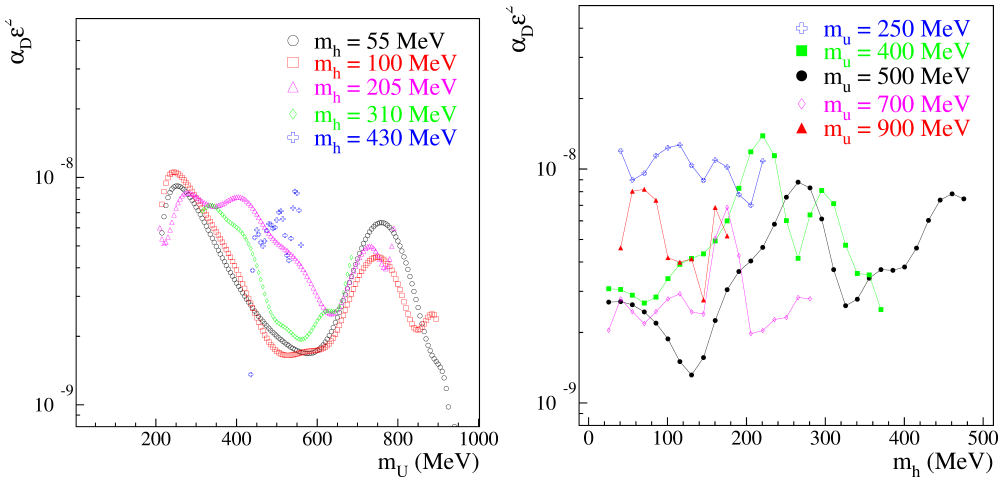

Figure 4: Combined 90% confidence level upper limits in $\alpha_D \times \epsilon^2$ as a function of m_U for different $m_{h'}$ values (**left**) and as a function of $m_{h'}$ for different m_U (**right**).

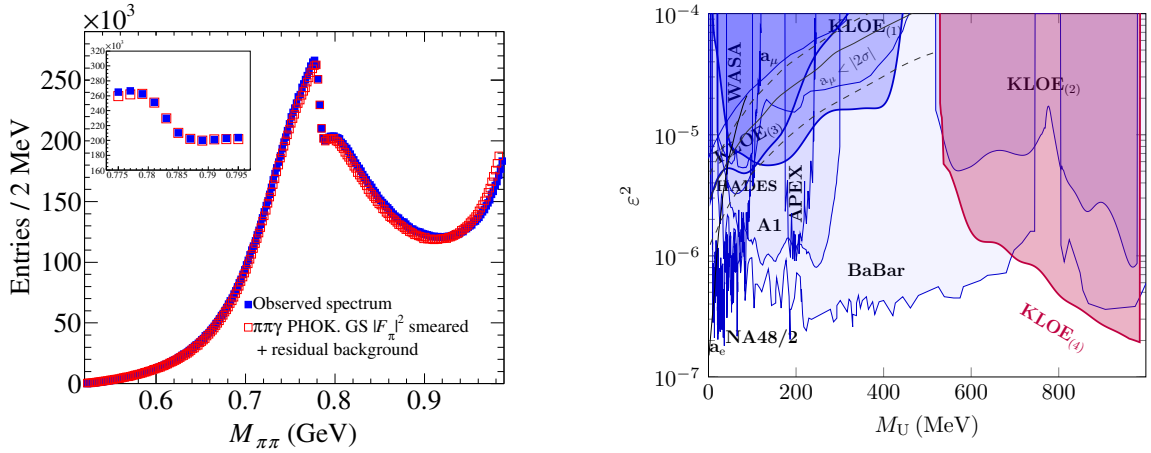

Figure 5: **Left:** Comparison of the measured data (blue squares) and simulation (red open squares) for the $M_{\pi\pi}$ invariant mass spectrum. **Right:** 90% CL upper limit exclusion plot for ϵ^2 as a function of the U-boson mass ($KLOE_{(4)}$). The limit is shown together with previous KLOE results as well as other experiments at the moment of publication.

no sign of a U-boson signal. No signal was observed and a limit at the 90% CL was set on the coupling factor ϵ^2 in the energy range between 527 and 987 MeV with a larger sensitivity than previous limits in the $\rho - \omega$ region and above, see Fig. 5.

7 Combined limit in the production of U decaying into $\mu^+\mu^-$ and $\pi^+\pi^-$

The search for the U boson in the decay into $\mu^+\mu^-$ has been extended by using the full KLOE statistics at $L_{int} = 1.93 fb^{-1}$, updating the analysis with a new estimate of the background, analogous to the one used for the $U \to \pi^+\pi^-$ search. This new search confirms the non existence of U-boson signal in the di-muon invariant mass spectrum. To increase the sensitivity in the region of the $\rho - \omega$ interference, both results on the 90% upper limit for $\mu\mu$ and $\pi\pi$ have been combined, giving the up-to-date most stringent

upper limit for the mixing parameter ϵ^2 in the U-boson mass region 519-987 MeV. The limit is shown in Fig. 6, together with the other most competitive limits in the region.

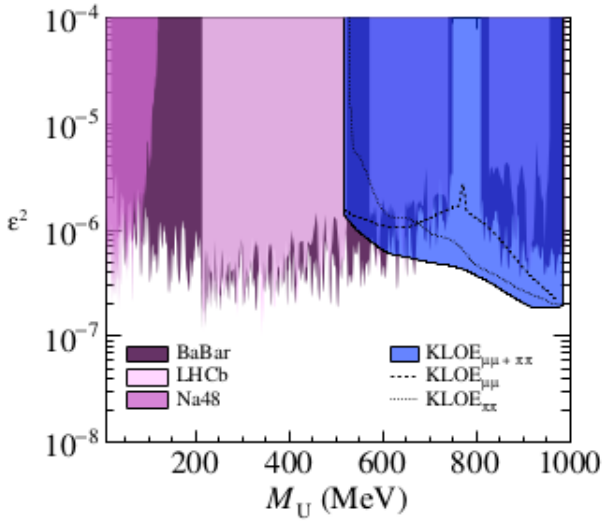

Figure 6: 90% CL exclusion plot for ϵ^2 as a function of the U-boson mass for the $e^+e^- \to U\gamma$ process. The $U \to \mu^+\mu^-$ limit (dashed line), the $U \to \pi^+\pi^-$ [36] constraint (solid line), and the $U \to \mu^+\mu^-$, $\pi^=\pi^-$ combination (blue area) at full KLOE statistics are presented in comparison with the competitive limits by BaBar [26], NA48/2 [34] and LHCb experiments [38].

8 Conclusions

The KLOE collaboration has extensively contributed to the U-boson searches by analyzing four different production processes. Up to now, no evidence for a U boson or dark Higgs boson was found and limits at the 90% confidence level were set on the kinetic-mixing parameter ϵ^2 in the mass range $5\,\text{MeV} < m_U < 987\,\text{MeV}$. Also, limits on $\alpha_D \times \epsilon^2$ at the 90% confidence level in the parameter space $2m_\mu < m_U < 1000\,\text{MeV}$, with $m_{h'} < m_U$, have been extracted from the search for the U boson in the dark Higgsstrahlung process. In the meantime, a new data campaign has been finalized with the KLOE-2 setup, which has collected more than $5\,\text{fb}^{-1}$ in the past three years. The new setup and the enlarged statistics could further improve the current limits on the dark coupling constant by at least a factor of two.

9 Acknowledgements

We warmly thank our former KLOE colleagues for the access to the data collected during the KLOE data-taking campaign. We thank the DAΦNE team for their efforts in maintaining low background running conditions and their collaboration during all data taking. We want to thank our technical staff: G.F. Fortugno and F. Sborzacchi for their dedication in ensuring efficient operation of the KLOE computing facilities; M. Anelli for his continuous attention to the gas system and detector safety; A. Balla, M. Gatta, G. Corradi and G. Papalino for electronics maintenance; C. Piscitelli for his help during major maintenance periods. This work was supported in part by the Polish National Science

Centre through the Grants No. 2013/11/B/ST2/04245, 2014/14/E/ST2/00262, 2014/12/S/ST2/00459, 2016/21/N/ST2/01727, 2016/23/N/ST2/01293, 2017/26/M/ST2/00697.

References

1. P. Jean et al., *Astrophys.* **407**, *L55 (2003).*
2. C. E. Aalseth, et al., *Phys. Rev. Lett.* **107**, *141301 (2011).*
3. R. Bernabei, et al., *Int. J. Mod. Phys.* **D13**, *2127 (2004).*
4. R. Bernabei, et al., *Eur. Phys. J.* **C56**, *333 (2008).*
5. J. Chang, et al. *Nature 456, 362 (2008).*
6. F. Aharonian, et al., *Phys. Rev. Lett.* **101**, *261104 (2008).*
7. F. Aharonian, et al., *Astron. Astrophys.* **508**, *561 (2009).*
8. A. A. Abdo, et al., *Phys. Rev. Lett.* **102**, *181101 (2009).*
9. B. Holdom, *Phys. Lett.* **B166**, *196 (1985).*
10. C. Boehm, P. Fayet, *Nucl. Phys.* **B683**, *219 (2004).*
11. P. Fayet, *Phys. Rev.* **D75**, *115017 (2007).*
12. M. Pospelov, A. Ritz, M.B. Voloshin, *Phys. Lett.* **B662**, *53 (2008).*
13. Y. Mambrini,*J. Cosmol. Astropart. Phys.* **1009**, *022 (2010).*
14. A. Gallo, et al., *DAFNE status report, Conf. Proc.* **C060626** *(2006) 604606.*
15. M. Adinolfi et al., *Nucl. Instrum. Methods* **A488**, *51 (2002)*
16. M. Adinolfi et al., *Nucl. Instrum. Methods* **A482**, *364 (2002)*
17. D. Babusci et al., *Phys. Lett.* **B706**, *251-255 (2012).*
18. D. Babusci et al., *Phys. Lett.* **B720**, *111-115 (2013).*
19. L. G. Landsberg, *Phys. Rep. 128,* **301** *(1985).*
20. G. C. Feldman, R. D. Cousins, *Phys. Rev.* **D57**, *3873 (1998).*
21. M. Reece, L.T. Wang, *JHEP* **07**, *51 (2009).*
22. D. Babusci et al., *Phys. Lett.* **B736**, *459-464 (2014).*
23. A. Anastasi, et al., *Physics Letters* **B750**, *633637 (2015).*
24. L. Barzé et all., *Eur. Phys. J.* **C71**, *1680 (2011).*
25. A. R. B. Batell, M. Pospelov,*Phys. Rev.* **D79**, *115008 (2009).*
26. J.P. Lees et al., *Phys. Rev. Lett.* **108**, *211801 (2012).*

27. Igal Jaegel for the Belle Collaboration, *Nucl. Phys. B (Proc. Suppl.)* **234**, *33-36 (2013).*

28. D. Babusci et al., *Phys.Lett.* **B747**, *365-372 (2015).*

29. J. D. Bjorken, et al., *Phys. Rev.* **D 80**, *075018 (2009).*

30. H. Merkel et al., *Phys. Rev. Lett.* [**112**, *221802 (2014).*

31. S. Abrahamyan et al., *Phys. Rev. Lett.* **107**, *191804 (2011).*

32. P. Adlarson et al., *Phys. Lett.* **B726**, *187 (2013).*

33. G. Agakishiev et al., *Phys. Lett.* **B731**, *265271 (2014).*

34. J.R. Batley et al., *Phys. Lett.* **B746**, *178185 (2015).*

35. J.P. Lees et al., *Phys. Rev. Lett.* **113**, *201801 (2014).*

36. A. Anastasi et al., *Phys. Lett.* **B757** *(2016) 356-361*

37. G. Gounaris, J.J. Sakurai, *Phys. Rev. Lett.* **21** *(1968) 244.*

38. S. Abrahamyan et al., *Phys. Rev. Lett.* **107** *(2011) 191804.*

Frascati Physics Series Vol. 67 (2018)
6th Young Researcher Workshop 'Physics Challenges in the LHC Era'
May 7 and 10, 2018

SEARCHING FOR DARK PHOTONS WITH THE PADME EXPERIMENT

C. Taruggi [1] [2] for the PADME collaboration
(1) Dipartimento di fisica, Università di Roma Tor Vergata - Roma, Italy
(2) Laboratori Nazionali di Frascati - Frascati (RM), Italy

Abstract

Despite cosmological evidences, the detection of dark matter (DM) has not produced any convincing evidence. For this reason, we can assume that the coupling between ordinary matter and DM is quite weak ($\epsilon \ll 1$). One of the most simple model that describes this weak coupling introduces a new symmetry $U(1)$ and a vector boson mediator A', called *dark photon* in analogy to the standard photon γ.
The PADME experiment will be held at Laboratori Nazionali di Frascati (LNF) to explore the coupling between ordinary matter and dark matter (DM) through the detection of Standard Model photons produced in the reaction $e^+e^- \to \gamma A'$. The measurement of the γ 4-momentum allows to reconstruct the missing-mass spectrum of the process, where the A' would appear as a peak. The experiment technique and its physical implications are described here.

1 Introduction

Cosmological evidences tell us that visible matter cannot explain the behaviour of many phenomena (galaxy rotation curves, gravitational lensing, CMB distribution...). Two roads can be followed to shed light on this problem: one leads to the change of gravitational laws, while the other leads to the existence of a new kind of matter, which does not produce radiation. Assuming that the present gravitational theory is correct, current observations tell us that we know only 4% of the Universe energy content [1]. According to cosmological theories, dark matter (DM) is about 23% of the total, and it interacts at least gravitationally with Standard Model (SM) particles.
In order to confirm this theoretical picture, experimental signals of DM should be detected. Many efforts have been done in this direction during the last decades, not without struggle. The difficulty to detect DM could be explained by the hypothesis that it lives in a different world with respect to SM particles. The DM world, that we can call *dark sector*, and the SM particles world could then be connected by

a fifth interaction. This new interaction would have a mediator, which can be a boson with different quantum numbers.
One of the most interesting feature of dark sector theories is that they can be used to explain other physical phenomena, besides DM's nature. For example, some dark sector theories contribute to understanding the muon g-2 anomaly [2)] and the ^{8}Be anomaly [3)].

2 Dark sector and dark photon

The simplest dark sector model introduces a U(1) symmetry, whose mediator is a vector boson A', that, in analogy with the standard photon, we call *dark photon* (DP). According to the dark sector model which one considers, there are different ways dark photon can be produced and decay. In this work, we take into exam DP production from e^+e^- interactions, so that we can have i) production from annihilation $e^+e^- \to A'\gamma$, ii) production from *bremsstrahlung* $e^-N \to e^-NA'$, iii) production from meson decays[1], like $\pi^0 \to A'\gamma$.
DP decay modes can be divided into visible and invisible ones. We have a *visible decay* when only SM particles would be in the final state: this would happen if DM particles with mass $m_{DM} \leq m_{A'}/2$ would not exist. In the opposite case, the final state would contain only DM particles, and we would have an *invisible decay*. Searching for visible or invisible decays leads to different dark photon properties (e.g. mass and coupling), meaning that different exclusion plots for $m_{A'}$ are obtained.

3 Detection of dark photons in PADME

The PADME experiment will study the annihilation process $e^+e^- \to A'\gamma$ induced by a positron beam impinging on atomic electrons of a nuclear target, and will explore the invisible decays of DP. The signature of this process will be given by a single γ in the detector. By knowing the beam properties and assuming the electron of the target at rest, the kinematics of the process is closed. That means that it is possible to evaluate the A' mass using the missing-mass technique. Calling P_{beam} the momentum of the positrons, P_e the momentum of the electrons and P_γ the momentum of the photon, we define:

$$M^2_{miss} = (P_{beam} + P_e - P_\gamma)^2 \tag{1}$$

as the missing mass of the annihilation process. The production of the A' would manifest as a peak at $m_{A'}$ in the missing-mass spectrum.

3.1 Main features of the experiment

PADME will be placed at the Beam Test Facility (BTF) of the Laboratori Nazionali di Frascati: the beam used by the experiment has an energy of 550 MeV, with 5000 e^+ per bunch (repetition rate is 50 Hz). The diamond target (~ 100 μm thick) allows to monitor the position of the beam interaction point, thanks to perpendicular graphite strips realized on both sides. After the interaction of the e^+ from the beam with the e^- of the target, the charged particles produced are deflected by a magnet (0.5 T) towards the veto's detectors. Neutral particles are free to reach the electromagnetic calorimeter (ECAL), made of 616 21 $\times$ 21 $\times$ 230 mm^3 BGO crystals. The shape of ECAL has a hole in the center, which allows the passage of *bremsstrahlung* radiation, that is detected by a Small Angle Calorimeter (SAC), which is

[1]Such mesons are produced in the e^+e^- reaction.

made of 25 $3 \times 3 \times 14$ cm^3 PbF_2 crystals (see Fig. 2 for a scheme of the experiment). The goal for the missing-mass resolution of ECAL is of the order of $2\%/\sqrt{E}$.

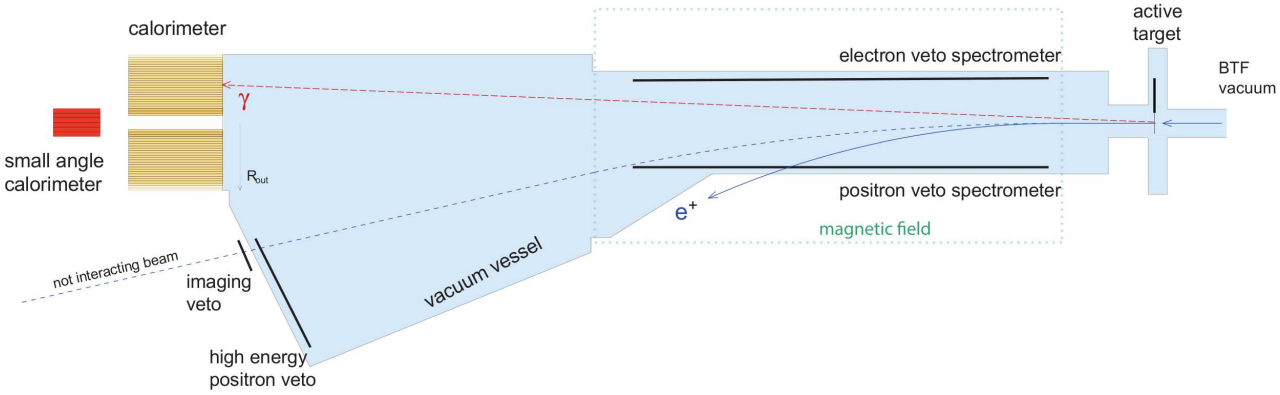

Figure 1: *A schematic picture of the PADME experiment.*

The signal that PADME will look for is represented by a single photon in the calorimeter. Other processes can mimic this signature, for example a SM annihilation in two photons, in which one of the two is lost, or a SM *bremsstrahlung* event with a lost e^+.
The main background contributions are given by $e^+e^- \to \gamma\gamma$, $e^+e^- \to \gamma\gamma(\gamma)$, $e^+N \to e^+N\gamma$ and pile-up. Background estimates and the possibility to reduce it have been investigated (see Fig. 2): background from pile-up gives an important contribution, but it can be rejected by making cuts on the missing mass and on the energy released in the calorimeter.

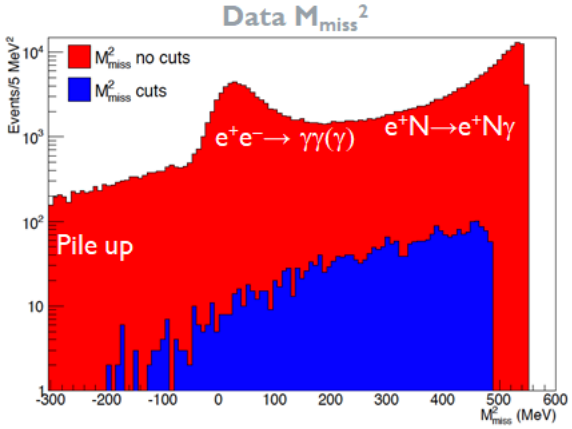

Figure 2: M^2_{miss} *for background events. Red: no selection cuts. Blue: all cuts are applied.*

Sensitivity studies have been performed using a GEANT4 simulation, with 2.5×10^{10} 550 MeV e^+

on target, extrapolated to 10^{13}. From these studies it emerged that PADME can explore, in a model-independent way, the mass range up to $m^2_{A'} = 2m_e E_{e^+}$ (red band in the plot in Fig. 3). With a beam energy of 550 MeV, we can reach $m_{A'} \leq 23.7$ MeV/c^2. Different beam energy allows to explore different mass regions.

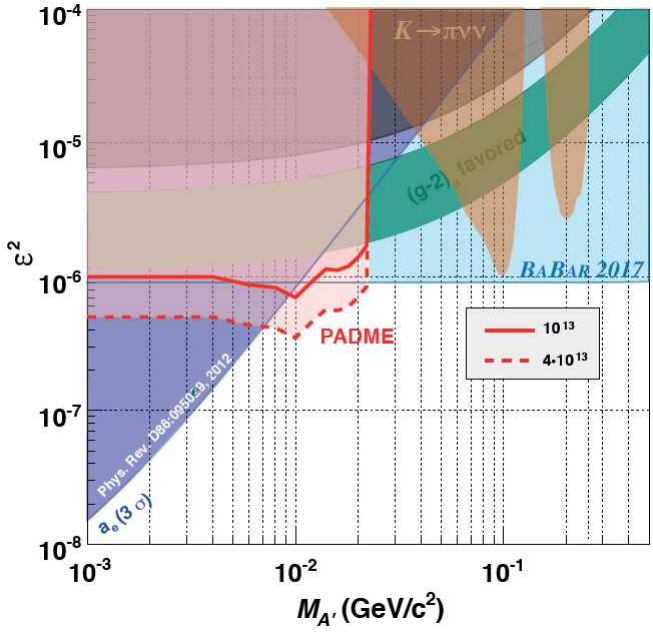

Figure 3: *Exclusion limits and prospects for the dark photon search at PADME.*

4 Conclusions

The PADME experiment will search for a dark photon (DP), as one of the possible mediators of a fifth interaction that connects our world to the so-called dark sector. PADME will study the invisible decay of DPs, via the annihilation process $e^+e^- \to A'\gamma$. The experiment will search for a DP with mass up to 23.7 MeV/c^2 (beam energy = 550 MeV). The data taking will start in September 2018 at LNF. The collaboration expect to collect $\sim 1 \times 10^{13}$ positrons on target in one/two years of data taking. The main components of the experiment are ready.
The collaboration expect a second physics run in 2019 at LNF.

5 Acknowledgements

The author gratefully acknowledge all the PADME collaboration.

References

1. Y. Akrami *et al* 2018 "Planck 2018 results. I. Overview and the cosmological legacy of Planck" arXiv:1807.06205.

2. M. Pospelov, Phys. Rev. D **80** 095002.

3. A. J. Krasznahorkay *et al* 2016 Phys. Rev. Lett. **116** 042501.

4. M. Raggi and V. Kozhuharov, Adv. High Energy Phys. 2014, 959802 (2014).

5. M. Raggi, V. Kozhuharov and P. Valente, EPJ Web Conf. **96**, 01025 (2015).

6. P. Valente *et al*, arXiv:1603.05651 [physics.acc-ph] (2016); INFN-16-04-LNF.

7. M. Raggi *et al*, Nucl. Instrum. Meth. A862, **31** (2017).

Frascati Physics Series Vol. 67 (2018)
6th Young Researcher Workshop 'Physics Challenges in the LHC Era'
May 7 and 10, 2018

AN ACTIVE DIAMOND TARGET FOR THE PADME EXPERIMENT

Federica Oliva on behalf of the PADME collaboration*
Dipartimento di Matematica e Fisica Ennio De Giorgi, Università del Salento and INFN, Sezione di Lecce, Italy

Abstract

PADME (Positron Annihilation into Dark Matter Experiment) [1] is a new experiment that is going to search for a dark photon produced in the annihilation between a positron of a bunched beam and an electron of a thin diamond target at the Beam Test Facility (BTF) of the INFN Laboratori Nazionali di Frascati (LNF).
Two diamond active target prototypes have been produced and assembled: one with laser made graphitic strip electrodes and the other one with more traditional CrAu strip electrodes. Currently, the active target with graphitic strips is under integration in the experiment. In this paper the physical motivation and the performance of the active diamond target of PADME are presented.

* P. Albicocco, F. Bossi, B. Buonomo, R. De Sangro, D. Domenici, G. Finocchiaro, L.G. Foggetta, A. Ghigo, P. Gianotti, G. Piperno, I. Sarra, B. Sciascia, T. Spadaro, E. Spiriti, E. Vilucchi (INFN, Laboratori Nazionali di Frascati), A.P. Caricato, F. Gontad, M. Martino, I. Oceano, F. Oliva, S. Spagnolo (INFN, Sezione di Lecce and Dip. di Matematica e Fisica, Università del Salento), C. Cesarotti, A. Frankenthal, J. Alexander (Department of Physics, Cornell University), G. Chiodini (INFN, Sezione di Lecce), F. Ferrarotto, E. Leonardi, F. Safai Tehrani, P. Valente (INFN, Sezione di Roma), S. Fiore (INFN, Sezione di Roma and ENEA), G. Georgiev (University of Sofia St. Kl. Ohridski and INFN, Laboratori Nazionali di Frascati), V. Kozhuharov (University of Sofia St. Kl. Ohridski, INFN, Laboratori Nazionali di Frascati, and Dip. di Fisica, Sapienza Università di Roma), B. Liberti, C. Taruggi (INFN, Laboratori Nazionali di Frascati and Università degli Studi di Roma Tor Vergata), G.C. Organtini, M. Raggi (INFN, Sezione di Roma and Dip. di Fisica, Sapienza Università di Roma), L. Tsankov (University of Sofia St. Kl. Ohridski).

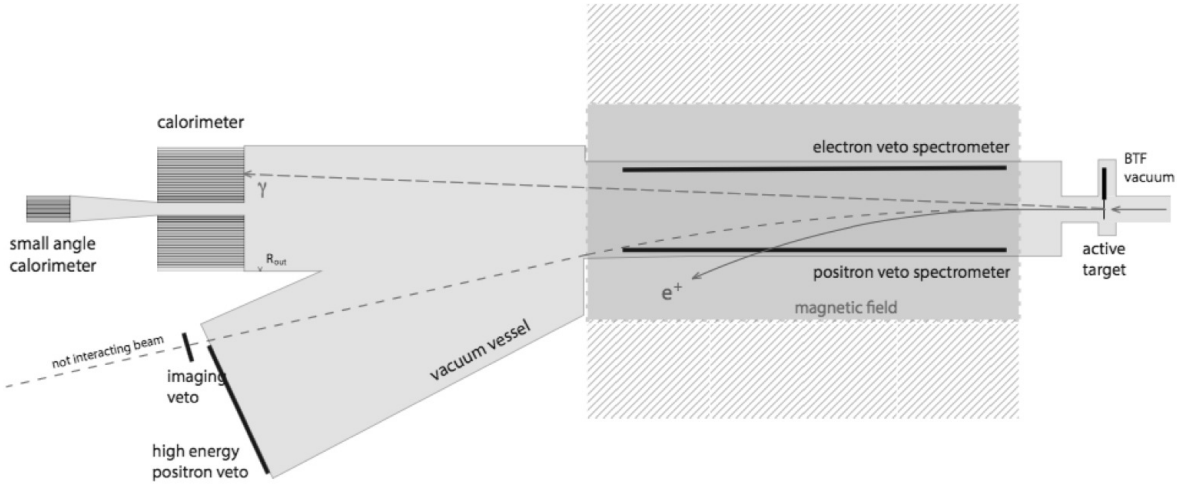

Figure 1: *Layout of the PADME experiment.*

1 The PADME experiment

The Standard Model (SM) of particle physics describes with high precision the strong, weak and electromagnetic interactions but not the dark matter puzzle. This issue is very important among the whole scientific community since the dark matter existence is demonstrated by cosmological and gravitational studies [2)]. The lack of experimental evidences of dark matter particle candidates at the electroweak scale has driven the attention to the idea of the existence of a dark sector only feebly interacting with the world which we know, through a neutral portal [3)]. One of the simplest model of dark sector is the one that introduces an additional symmetry $U(1)'$ to describe the interactions between dark particles. The corresponding gauge boson of the dark sector is the dark photon A'. Different experiments all over the world are searching this boson, both in the visible and invisible decay modes.
The PADME experiment will search for the dark photon A' in the process $e^+e^- \to \gamma A'$ using the missing-mass method, which is independent from the new gauge boson decay mode. The missing mass squared is reconstructed by the formula:

$$M^2{}_{miss} = (P_{e^+} + P_{e^-} - P_\gamma)^2, \tag{1}$$

where P_{e^+}, P_{e^-} and P_γ are the 4-momenta of the positron beam, of the target electron and of the emitted photon, respectively. PADME will use the 550 MeV positron beam of the Beam Test Facility (BTF) of the Laboratori Nazionali di Frascati (LNF) of INFN. According to the PADME design, the region of sensitivity is $M_{A'} \leq 23.7$ MeV/c^2 and $\epsilon^2 > 10^{-6}$, where $M_{A'}$ and ϵ are the dark photon mass and the $A'\gamma$ mixing parameter, respectively.
The PADME detector (Fig. 1) is made of a thin diamond target, a magnetic dipole, which bends the beam outside the experimental acceptance, a high resolution electromagnetic calorimeter (ECAL), a small angle electromagnetic calorimeter (SAC) capable to sustain a high rate, and a charged-particle veto system. The diamond target and the veto detectors will be hosted in the vacuum vessel.

2 The active diamond target for PADME

A thin diamond is a good candidate for the active target of the PADME experiment thanks to its low atomic number ($Z = 6$), that limits the Bremsstrahlung interactions ($\propto Z^2$), main source of background, with respect to annihilation ($\propto Z$). In addition, the choice of the active target is dictated by the possibility to improve the missing-mass resolution, if the target production point is measured with a precision < 1 mm.

2.1 The assembly of the detectors

The development of new detection techniques and materials is important to overreach the limit of traditional detectors. Chemical Vapor Deposition (CVD) diamond is a new material for particle detectors with many interesting properties, among which the high radiation hardness, a very useful feature in high-energy-physics experiments. CVD is a technique that takes advantage of the metastable synthesis of the diamond at low pressure, using mixtures of hydrocarbons (CO or CH4) and hydrogen in presence of plasma. Until now diamond detectors have been used especially as beam monitors, luminometers and dosimeters. The active diamond target of PADME is a 100 μm thick and 2×2 cm^2 large CVD polycrystalline diamond, produced by Applied Diamond Inc. (USA), with 19×19 strips on the front and back side in two orthogonal directions. Two sensors with different types of electrodes were made: one with graphitic strips and one with metallic strips. The more traditional metal contacts were obtained through thermal evaporation of Cr and Au layers directly from Applied Diamond.
Instead of this, an innovative graphitization process allows to obtain graphitic strips which are uniform on the surface by means of a laser. Laser irradiation of a particular wavelength on a limited area of the diamond wafer involves the transformation from diamond to graphite [4]. The ohmic graphitic contacts were realized by means of an excimer laser ArF (λ=193 nm) in the L3 Laboratory of Lecce. Both diamond detectors were precisely positioned with a micrometric XYZ and Θ handling system to two printed circuit boards (inner boards) and mechanically connected by spots of Araldite glue, previously deposited using a dispensing system equipped with a syringe. Each detector was assembled on the inner board with the horizontal strips (Y strips) on the front side and the vertical strips (X strips) on the back side. The inner board (see Fig. 2) provides the high voltage to each strip, which is AC coupled to the front-end. The electrical connections on the front side were realized by wire bonding between every golden Y strip pad of the inner board and each graphitic strip. A precision wire bonding machine at INFN in Perugia was used. The electrical connections on the back side were realized by filling special holes of the inner boards with a conductive glue. During this procedure the electric resistance was measured and final values < 1 Ω were reached. In Fig. 3 the front side and the back side of the detector with graphitic strips is shown, as mounted on the inner board. The front-end electronics chosen for the final experiment consists of two evaluation boards of the AMADEUS chip which are electrically connected to the inner board by two rigid connectors on both sides, to readout 16 X and 16 Y strips. The front-end electronics was turned-on in vacuum with a pressure of 10^{-6} mbar, to verify that the heating produced by power dissipation is limited and easily removed by the thermal path existing between the inner board and the aluminium holders. An external thermal imager through a ZnSe window, which is transparent to thermal radiation, helped to monitor the temperature. The highest temperature was observed at the location of a voltage regulator which reached the temperature of 36°C in vacuum (stable over 3h of operation), with a time constant of about 45 s, while it was operating at 25°C in Air. The assembly made of one inner board and two front-end boards is rigidly bound to a CF100 vacuum flange by a support frame machined from a single aluminium piece. A 50-pins feedthrough connector brings outside the electrical services, the calibration

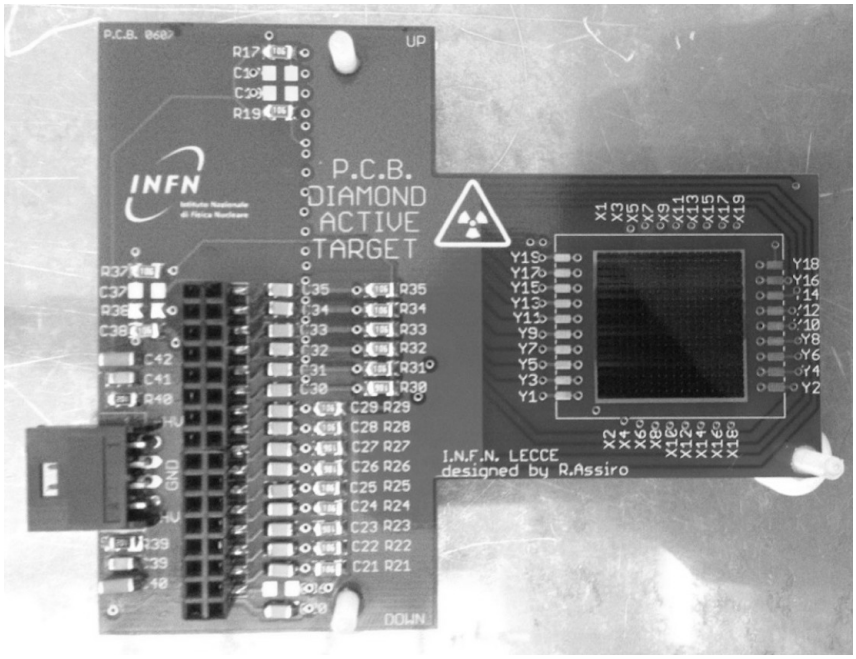

Figure 2: *Inner board of the active diamond target instrumented with the CVD diamond sensor with graphitic strips.*

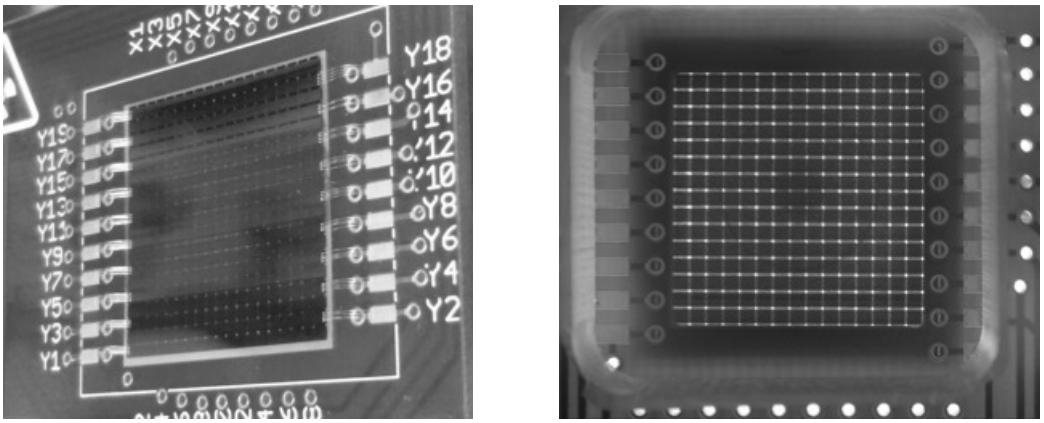

Figure 3: *Front (left) and back (right) sides of the CVD diamond sensor with graphitic strips.*

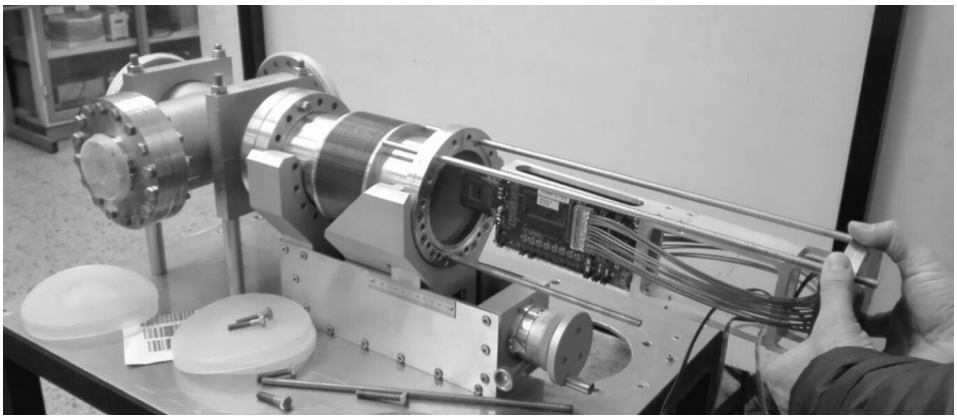

Figure 4: *Insertion test of the active diamond target into the linear positioning system connected to a vacuum-cross by a bellow.*

signal and the output signals. The target will be placed in the experiment by a linear positioning system and vacuum bellow using a vacuum-cross which intercepts the beam before the PADME vacuum vessel and the magnetic dipole (see Fig. 4).

2.2 DAQ and DCS system for the target

A DCS software based on ROOT has been designed to remotely control each instrument by means of an ethernet-GPIB interface. The diamond target front-end will be automatically calibrated in order to obtain the gain and the noise of each charge amplifier. This is going to be accomplished thanks to a GUI interface and analysis macros. During the calibration each signal is digitized at 1 GS/s by a CAEN digitizer DT5242. In addition, the DCS is integrated with the DAQ of the experiment and stores detector parameters and run information in MySQL database.
During the experiment the signal will be digitized at 1 GS/s with a CAEN digitizer V1742.

3 Beam Test of the first active diamond target prototype with graphitic strips

A first diamond sensor prototype with graphitic strips and same geometrical characteristics, but different thickness (50 μm), was tested in November 2015 using the $e^{\pm}$ beam of the DAΦNE Linac. The beam test was made using a bunch of positrons (or electrons) at a rate of 50 Hz, energy 450 MeV and average multiplicity of about 10000 particles. The mean multiplicity was checked by a lead-glass calorimeter placed beyond the target. Each strip of the target was readout by single-channel diamond amplifiers from CIVIDEC [5]. Some strips were connected to charge amplifiers, the others to voltage amplifiers. To test different kind of interconnections, the X strips, which gave the horizontal position, were electronically connected using wire bonding or silver paint; all the Y strips, which gave the vertical position, were connected with silver paint. Not all connections turned out to be working in the beam test: only 12 X and 10 Y strips delivered a signal. During the beam test the signals were digitized at 1 GS/s for normal runs and at 5 GS/s for timing measurements using a CAEN V1742. The beam test allowed to demonstrate the efficiency of a diamond detector with graphitic strips as beam monitoring. The data collected were used to reconstruct the beam profile in both views (X and Y) and also to characterize the detector by measuring the spatial and time resolution and the charge collection distance (CCD), the last

one being an important property of the material. The bias voltage of the target during the data taking was 150 V. Integrating each signal in a determinated time window was possible to evaluated the charge released on each strip. A preliminary calibration of each amplifier was strictly needed to evaluate the single gain of each amplifier. The root-mean-square of the distributions for the X and Y beam charge centroid gave an estimate of the spatial resolution, which was about 0.20 mm along X and about 0.32 mm along Y strips, much better than PADME requirement (<1 mm). In addition, a time resolution of 0.6 ns for the strip with the highest signal and an average charge collection distance of about 11 μm were also measured.

4 Conclusions

Two diamond detectors are ready to be integrated in the final detector of the experiment: one with graphitic strips and one, more traditional, with metal contacts. They are equipped with two 16-channel AMADEUS chips and both detectors have a 100 μm thickness. The diamond target is going to be installed in the experimental area in August and its front-end is going to be calibrated before PADME data taking.

5 Acknowledgements

This work is partly supported by the Italian Ministry of Foreign Affairs and International Cooperation (MAECI) under the grant PRG00226 (CUP I86D16000060005), the BG-NSF DN-08/14 from 12.2016, and the MoU SU LNF-INFN 70-06-497/07-10-2014 projects.

References

1. M. Raggi and V. Kozhuharov, *Proposal to search for a dark photon in positron on target collisions at DAΦNE linac*, Adv. High Energy Phys. **509**, 959802 (2014);

2. O. Adriani et al., [PAMELA Collaboration], *An anomalous positron abundance in cosmic rays with energies 1.5-100 GeV*, Nature **458**, 607 (2009);

3. J. Alexander et. al., *Dark Sectors 2016 Workshop: Community Report*, arXiv:1608.08632 [hep-ph] (2016);

4. M. De Feudis *et al.*, *Diamond graphitization by laser-writing for all-carbon detector applications*, Diam. Relat. Mater. **75**, 25-33 (2017);

5. R. Assiro *et al.*, *Performance of the diamond active target prototype for the PADME experiment at the DAΦNE BTF*, NIM A **898**, 105-110 (2018).

Frascati Physics Series Vol. 67 (2018)
6th Young Researcher Workshop 'Physics Challenges in the LHC Era'
May 7 and 10, 2018

ON SEARCH FOR DARK PHOTON AND ITS RESONANT PRODUCTION IN PADME EXPERIMENT

Anish Ghoshal
INFN, Laboratori Nazionali di Frascati, C.P. 13, I-00044 Frascati, Italy
Dipartimento di Matematica e Fisica, Università di Roma Tre, I-00146 Rome, Italy

Abstract

Positron beam-dump experiments like PADME can search for very narrow resonances coupled very weakly to e^+e^- pairs. In these proceedings, we summarize the 17 MeV dark-photon candidate as a solution to ^{8}Be anomaly and how it can be searched for in resonant production via e^+ annihilation in the target. Due to the continue loss of energy from soft-photon bremsstrahlung, in the first few radiation lengths of the dump a positron beam can continuously scan the parameter space.

1 Introduction

Observed dark matter (DM), neutrino masses, and the baryon asymmetry of the Universe (BAU), cannot be accounted for within the standard model (SM) of particle physics. Thus, physics beyond the Standard Model (BSM) corresponding to a whole new sector containing new particles as well as new interactions maybe required. If such a sector exists, there are two possible reasons why it has not been discovered yet: (i) the mass scale of the new particles, including the mediators of the new forces, is well above the energy scale reached so far in laboratory experiments; (ii) the mass scale is within experimental reach, but the couplings between the new particles and the SM are so feeble that the whole new sector has so far remained hidden. For the second scenario, the Standard Model of particle physics can naturally be extended with a light neutral vector particle with kinetic mixing to the photon field at low energy. This is both theoretically and phenomenologically motivated. Theoretically, most of the string theory constructions lead to a light neutral vector field with all the heavy modes integrated out. And phenomenologically, it is well-motivated to use the dark photon as a portal to connect DM to the SM. For MeV-scale dark photons, beam-dump experiments are proposed to the detect it directly by shooting electron or proton beams into a fixed target (review in Ref. [1)]). Sub-keV dark photons can be produced inside the stellar systems, where the chain

of nuclear reaction processes inside the center of the stars constrain the stellar lifetime, subsequently constraining the dark-photon parameters. For a sub-eV scale dark photon, it can also be produced and detected in labs via oscillations from a laser beam by what is known as "light-shining-through-the-wall" (LSW) experiments . Several proposals and many new ideas to hunt for new physics at the intensity frontier (see [2, 3] for recent reviews) have been proposed. Here we discuss our work [4] in which we have identified a resonant-production search mechanism for dark photons in beam-dump experiments. PADME in LNF is expected to search for this in the parameter range of the dark photon suitable to pose as a candidate for the ^{8}Be anomaly in the ATOMKI experiment. We present the model, the novel method and expected PADME sensitivity in this work. For other details regarding various thick target effects and analyses, refer to Carvajal's work [5] in the same LNF Spring School 2018 proceedings.

2 Dark Photon: Models and Search

The minimal extension of the SM gauge group by an additional the so called dark-photon (DP) or A'-boson, that is a massive gauge boson arising from a new $U(1)'$ symmetry, can be considered as a natural candidate for a super-weakly coupled new state, since its dominant interaction with the SM sector might arise solely from a mixed kinetic term in the following effective Lagrangian, well below the electroweak scale,

$$\mathcal{L} = -\frac{1}{4}F_{\mu\nu}^2 - \frac{1}{4}{F'}_{\mu\nu}^2 - \frac{\kappa}{2}F_{\mu\nu}F'^{\mu\nu} + \frac{m_{A'}^2}{2}{F'}_{\mu}F'^{\mu}, \tag{1}$$

$(\epsilon/2)F'_{\mu\nu}F^{\mu\nu}$ coupling the $U(1)'$ and QED field strength tensors, with values of ϵ naturally falling in a range well below 10^{-2}. For a massive $U(1)$ gauge boson, the mass term can be written as

$$\mathcal{L}_{\text{mass}} = \frac{1}{2}m_{A'}^2\left({A'}_{\mu} - \frac{\partial_\mu a}{m_{A'}}\right)^2 , \tag{2}$$

where a is the would-be Goldstone field. Depending on the mass generation mechanism SC (Stückelberg case) or HC (Higgs case) there may be an extra light scalar in the theory. In the Unitary gauge the mass term is:

$$\mathcal{L}_{\text{mass}} = \frac{1}{2}m_{A'}^2{A'}_{\mu}A'^{\mu}. \tag{3}$$

On the other hand, in the HC with the spontaneous symmetry breaking of the dark $U(1)$ field by the BSM Higgs (h'), additional terms of interactions between the Higgs and the dark photon come:

$$\mathcal{L}_{\text{int}} = e'm_{A'}h'{A'}_{\mu}^2 + \frac{1}{2}e'^2h'^2{A'}_{\mu}^2 , \tag{4}$$

where e' is the gauge coupling constant of the dark $U(1)$ group. However, here we consider no other BSM particles except the A'.

Lower limits on ϵ are obtained from electron beam-dump experiments at KEK and Orsay, which have been re-analyzed in Ref. [6]. This is observed to have the contextual mass range $m_{A'} \sim 17\,\text{MeV}$ and $\epsilon \gtrsim 7\times10^{-5}$. A stronger limit, $\epsilon \gtrsim 2\times10^{-4}$, was obtained in [7] from a re-analysis of the E141 experiment at SLAC [8]. However, for $m_{A'} \sim 17\,\text{MeV}$ the excluded region is very close to the kinematic limit of the sensitivity and the reach in mass has been overestimated as shown in [9]. Besides this, A' slightly heavier than the benchmark value of 17 MeV would in any case evade the E141 limit, so the bound is debatable. Conservatively, it is assumed that the corresponding region is still not excluded by any experiment.

Upper bounds on ϵ in the relevant A' mass range also exist, e.g., from the KLOE-2 experiment which has looked for $e^+e^- \to \gamma A'$, followed by $A' \to e^+e^-$, setting the limit $\epsilon < 2 \times 10^{-3}$ [10], while constraints from the anomalous magnetic moment of the electron yield $\epsilon < 1.4 \times 10^{-3}$ [11]. A competitive limit stems from BaBar searches [12] for $A' \to e^+e^-$ decays, but it is applicable for $m_{A'} > 20\,\mathrm{MeV}$. In summary, we concentrate on the range

$$7 \times 10^{-5} \leq \epsilon \leq 1.4 \times 10^{-3}\,, \tag{5}$$

as the window allowed for a 17 MeV A' decaying dominantly into e^+e^-. This corresponds to a DP width $2.0 \times 10^{-4} \leq \Gamma_{A'}/\mathrm{eV} \leq 8.1 \times 10^{-2}$.

3 ^{8}Be ATOMKI Anomaly

Discrepancies between SM predictions and experimental results, as for example the measured value of the muon anomalous magnetic moment [13], the value of the proton charge radius as measured in muonic atoms [14], or the anomaly observed in excited ^{8}Be nuclear decays by the Atomki collaboration [16] exist. This last anomaly is particularly relevant here since the new experimental technique discussed here appears remarkably well suited to test, at least in some region of the parameter space, the particle physics explanation involving a new gauge boson with mass $m_{A'} \sim 17\,\mathrm{MeV}$ kinetically mixed with the photon [17].

The anomaly consists in the observation of a bump in the opening-angle and invariant-mass distributions of electron-positron pairs produced in the decays of an excited ^{8}Be nucleus [16], which is unaccountable by known physics. The anomaly has a high statistical significance of 6.8σ which excludes the possibility of it being just a statistical fluctuation and is not solvable with more data. The shape of the excess (like that of resonance) is extraordinarily consistent with that of an a new particle with mass $m_{A'} = 17.0 \pm 0.2(\mathrm{stat}) \pm 0.5(\mathrm{sys})\,\mathrm{MeV}$ [16]. The strength of the A' coupling to e^+e^- pairs, parametrized as $\epsilon = \sqrt{\alpha'/\alpha}$, with α' the $U(1)'$ fine structure constant, is constrained by different experimental considerations. In the Atomki setup, $A' \to e^+e^-$ decays must occur in the few-cm distance between the target, where the ^{8}Be excited state is formed, and the detectors. This implies a lower limit $\epsilon/\sqrt{\mathrm{Br}(A' \to e^+e^-)} \gtrsim 1.3 \times 10^{-5}$ (we will always quote limits on ϵ leaving understood that they apply to its absolute value). In the following, we will assume for simplicity $\mathrm{Br}(A' \to e^+e^-) = 1$, if the A' decay with a non-negligible rate into invisible dark particles χ, with $m_\chi < m_{A'}/2$, the quoted limits need to be accordingly rescaled. Nonetheless in case the invisible decay channel becomes largely dominant, other limits should come into play. But such a discussion is beyond the scope of this work.

4 Search in PADME: Expected Sensitivity

The PADME experiment [18] at the DAΦNE LINAC Beam Test Facility (BTF) of the INFN Laboratori Nazionali di Frascati (LNF) has been designed to search for DP by using a positron beam impinging on a thin target of low atomic number. The signal for A' can be detected in the invisible channel by looking for a narrow bump in the spectrum of the missing mass measured in single-photon final states, originated via $e^+e^- \to \gamma A'$. The experiment uses a 100μm thick active target made of polycrystalline diamond ($Z = 6$). The low Z and very thin target are intended to minimize the probability of photon interaction inside the target since, in order to reconstruct accurately the missing mass. The PADME detector is able to detect photons and charged particles and it will be sensitive to invisible ($A' \to \chi\bar{\chi}$) as well as to visible ($A' \to e^+e^-$) DP decays.

Table 1: *Beam parameters for the Frascati BTF.*

	pot/yr	$E_{\min}$ (MeV)	$E_{\max}$ (MeV)
e^+	10^{18}	250	550
e^-	10^{18}	250	800

Collider searches for dark photons have been carried out in electron beam dump experiments (see [6]) for a review) assuming A'-strahlung as the leading production mechanism in electron-nucleon scattering which is a process of order α^3. Similarly, A' searches with positron beams can be considered via the process analogous to the usual QED process of positron annihilation off an atomic target electron with two final-state photons, where one photon is replaced by one A' corresponding to a process of $O(\alpha^2)$ order (Fig. 1).

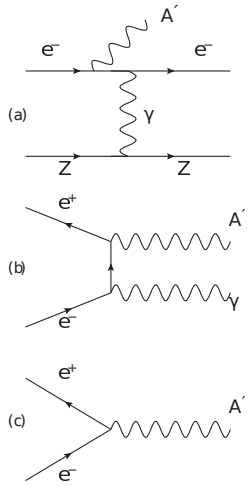

Figure 1: *A' production modes in fixed-target electron/positron beam experiments: (a) A'-strahlung in e^--nucleon scattering; (b) A'-strahlung in e^+e^- annihilation; (c) resonant A' production in e^+e^- annihilation.*

With the A' masses in the range $\gtrsim 1\,\mathrm{MeV}$, the process of resonant e^+e^- annihilation into on-shell A' production as shown in 1(c) is parametrically enhanced with respect to the previous two production channels due to it being $O(\alpha)$ process. A' production via resonance has the advantages that altogether suggest that it might be particularly convenient to operate the PADME (as well as other positron beam-dump experiments) positron beam fixed target experiment in a dedicated mode in order to search for A' via resonant production. The sensitivity of the PADME experiment to the production process $e^+e^- \to A' \to e^+e^-$needs the original thin diamond target be replaced by a tungsten target of several cms of length. This consequently absorbs most of the incoming positron beam and the related EM showers, leading to degrading sufficiently the energy of the residual emerging particles, so that the charged-particle backgrounds are gotten rid of. The A' produced in e^+e^- annihilation, if sufficiently long lived, will escape the dump without interacting, and will decay inside the downstream vacuum vessel, producing an e^+e^- pair of well defined energy. Moreover, the thick tungsten target thus allows to take advantage of the full beam intensity of 10^{18} pot/yr, since now the sufficiently long lived A' produced in e^+e^- annihilation,

will escape the dump. Thus straight-away we gain a five orders of magnitude with respect to the thin target running mode (electron full beam intensity is of 10^{13} pot/yr), see Table 1. There is yet another advantage envisaged for using a thick target: this provides an almost continuous energy loss for the incoming positrons propagating through the dump, and they can efficiently 'scan' in energy for locating very narrow resonances due to their radiative feedback. Simply put, a positron in the beam originally not oriented for resonant production (due to Gaussian beam distribution) may become suitable for resonance after bremsstrahlung energy loss.

Besides experiments with positron beams, resonant $e^+e^- \to A'$ annihilation must also be accounted for in a correct analysis of electron beam-dump experiments since, as is remarked in [19], positrons are abundantly produced in the electromagnetic (EM) showers inside the dump. This feature was recently exploited in [19] in re-analysing old results from the SLAC E137 experiment by including A' production via resonant annihilation (and, but less importantly, also A'-strahlung in annihilation). As a result, it was found that, due to the contribution of resonant A' production, the E137 data exclude a parameter-space region larger than it was previously thought [7, 6]. The extended excluded region corresponds to the area in light grey color towards the bottom of the plot in Fig. 2 . Hence, in analysing electron beam-dump data, A' production from annihilation of secondary positrons via the diagrams in Figs. 1 should be also accounted for.

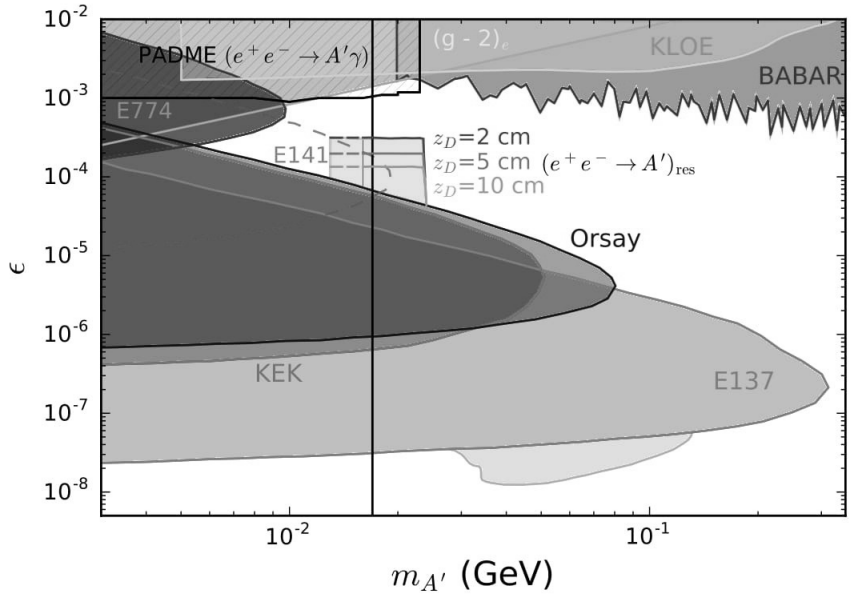

Figure 2: *a) In the figure, the vertical black line gives the location of the DP resonance at $m_{A'} = 17\,MeV$. The reach in A' mass might be: a viable window remains between the Orsay/KEK lines ($\epsilon \gtrsim 7 \cdot 10^{-5}$) and the $(g-2)_e$ line ($\epsilon \lesssim 1.4 \cdot 10^{-3}$). The black hatched region depicts the predicted sensitivity of PADME in thin target mode, that will search for DP via the $e^+e^- \to A'\gamma$ process. The limits assume 10^{13} pot/yr. The trapezoidal regions represent instead the constraints that PADME could set by running in thick target mode with 10^{18} pot/yr, and are respectively for tungsten targets of 10 cm, 5 cm and 2 cm of length, and neglecting backgrounds.*

The PADME spectrometers can detect e^+e^- pairs with good resolution for coincidence in time and momentum. Punch-through photons, produced via bremsstrahlung in the very first layers of the dump,

carrying a large fraction of the original beam energy, and converting in e^+e^- in the last millimeter or so, constitute the most dangerous background, but could be significantly suppressed with a plastic scintillator veto few mm thick. The invariant mass of the e^+e^- originating from photon conversion $m^2_{e^+e^-} = 0$ is very far from $m^2_{e^+e^-} \sim (17\,\mathrm{MeV})^2$ expected from resonant annihilation, so the background could be nicely eliminated via a suitable tracker for accurate e^+e^- invariant mass reconstruction.

In Fig. 2 we show the the current limits for DP searches assuming visible A' decays into e^+e^- pairs with 100% branching fraction and suppressed couplings to the proton. The BTF energy range for positron beams $250 \lesssim E_b/\mathrm{MeV} \lesssim 550$ corresponds to centre-of-momentum energies: $16 \lesssim E_{\mathrm{c.m.}}/\mathrm{MeV} \lesssim 23.7$. However, because of positron energy losses, the region at low $m_{A'}$ that can be explored extends to values smaller than 16 MeV, as indicated in the figure. Of course, in propagating well inside the dump, the beam gets degraded in energy, but these effects are not considered. Thus, we can expect that the experimental sensitivity could be extended down to $m_{A'}$ values lower than 16 MeV by no more than a few MeV. This well might still be sufficient to reach into the region where the E141 exclusion limits can be trusted.

The two PADME search modes are complementary, since they can set new bounds respectively in the regions of large $O(10^{-3})$ and small $O(10^{-4})$ values of the DP mixing parameter ϵ. With some intense and dedicated experimental efforts, the new regions in Fig. 2 could be explored in less than one year of running. In particular, the allowed window for the ^{8}Be DP could be sizeably reduced, or on the other hand its existence could be firmly confirmed.

5 Conclusions

The Frascati BTF can provide beams with energy between $250 - 550\,\mathrm{MeV}$ (positron beam). This range corresponds to the centre-of-momentum energy needed to produce via e^+e^- annihilation a resonance A' with $m_{A'} \sim 17\,\mathrm{MeV}$. So, we suggested this can also be designed in a new way to search for narrow resonances, and specifically for DP, coupled to e^+e^- pairs, via resonant production in e^+e^- annihilation. Moreover, this range of DP is also compatible with the DP invoked to explain the anomaly observed in ^{8}Be nuclear transitions [15, 16]. By exploiting this production process, the Frascati PADME experiment, presently under commissioning, will be able to reach well inside the interesting parameter space region, as shown in our results in Fig. 2. Before concluding, we point out that resonant $e^+e^- \to A'$ production can be relevant also for electron beam-dump experiments, since secondary positrons that could trigger the annihilation process are abundantly produced in EM showers. With this understanding, SLAC E137 data [19] data was re-analysed. Consequently, the previously excluded regions in [7, 6] got extended towards smaller ϵ values. PADME has started taking data from May 2018. For other details refer to Carvajal's work [5] in the same Frascati Spring School 2018 proceedings. The same strategy has been adopted to search for dark matter in lepton beam dump experiments [20]. In general, the basic idea is that the dark photon acts as a portal to the dark sector, so its main branching fraction is involved with light dark matter (BSM) fermions and can be searched with A' invisible decays.

6 Acknowledgements

We acknowledge the INFN-LNF theory group and the organizers of the Frascati Spring School seminars for the opportunity to present this work.

References

1. R. Essig *et al.*, "Working Group Report: New Light Weakly Coupled Particles,"

2. J. Alexander *et al.*, "Dark Sectors 2016 Workshop: Community Report,"

3. M. Battaglieri *et al.*, "US Cosmic Visions: New Ideas in Dark Matter 2017: Community Report,"

4. E. Nardi, C. D. R. Carvajal, A. Ghoshal, D. Meloni and M. Raggi, Phys. Rev. D **97** (2018) no.9, 095004 doi:10.1103/PhysRevD.97.095004

5. C.D.R.Carvajal"DP production in e + beam dump experiments via resonant e + e annihilation" LNF-Spring Proceeding 2018

6. Andreas et al.Phys. Rev. D **86** (2012), 095019 doi:10.1103/PhysRevD.86.095019

7. Bjorken et al.Phys. Rev. D **80** (2009), 075018 doi:10.1103/PhysRevD.80.075018

8. Riordan et al.Phys. Rev. Lett. **59** (1987), 755 doi:10.1103/PhysRevLett.59.755

9. Y. S. Liu and G. A. Miller, Phys. Rev. D **96**, no. 1, 016004 (2017) doi:10.1103/PhysRevD.96.016004

10. A. Anastasi *et al.*, Phys. Lett. B **750**, 633 (2015) doi:10.1016/j.physletb.2015.10.003

11. H. Davoudiasl, H. S. Lee and W. J. Marciano, Phys. Rev. D **89**, no. 9, 095006 (2014) doi:10.1103/PhysRevD.89.095006

12. J. P. Lees *et al.* [BaBar Collaboration], Phys. Rev. Lett. **113**, no. 20, 201801 (2014) doi:10.1103/PhysRevLett.113.201801 [arXiv:1406.2980 [hep-ex]].

13. T. Blum, A. Denig, I. Logashenko, E. de Rafael, B. Lee Roberts, T. Teubner and G. Venanzoni, "The Muon (g-2) Theory Value: Present and Future,"

14. R. Pohl et al. "Laser spectroscopy of muonic deuterium," Science 12 Aug 2016: Vol. 353, Issue 6300, pp. 669-673 DOI: 10.1126/science.aaf2468

15. A. J. Krasznahorkay *et al.*, Phys. Rev. Lett. **116**, no. 4, 042501 (2016) doi:10.1103/PhysRevLett.116.042501

16. A. J. Krasznahorkay *et al.*, EPJ Web Conf. **137**, 08010 (2017). doi:10.1051/epjconf/201713708010

17. J. L. Feng, B. Fornal, I. Galon, S. Gardner, J. Smolinsky, T. M. P. Tait and P. Tanedo, Phys. Rev. D **95**, no. 3, 035017 (2017) doi:10.1103/PhysRevD.95.035017

18. M. Raggi, V. Kozhuharov and P. Valente, EPJ Web Conf. **96**, 01025 (2015) doi:10.1051/epjconf/20159601025

19. L. Marsicano *et al.*, Phys. Rev. D **98**, 015031 (2018) doi:10.1103/PhysRevD.98.015031

20. L. Marsicano *et al.*, Phys. Rev. Lett. **121**, no. 4, 041802 (2018) doi:10.1103/PhysRevLett.121.041802 [arXiv:1807.05884 [hep-ex]].

Frascati Physics Series Vol. 67 (2018)
6th Young Researcher Workshop 'Physics Challenges in the LHC Era'
May 7 and 10, 2018

DARK-PHOTON PRODUCTION IN e^+ BEAM-DUMP EXPERIMENTS VIA RESONANT e^+e^- ANNIHILATION

Cristian David Ruiz Carvajal
Universidad de Antioquia, Instituto de Física, Calle 70 No. 52-21, Medellín, Colombia

Abstract

We explore the foreseeable sensitivity of the Frascati PADME experiment to searching, with the resonance annihilation technique, for the 17 MeV dark photon invoked to explain the ^{8}Be anomaly in nuclear transitions. This involves a positron beam-dump experiment where, due to the continue loss of energy from soft photon bremsstrahlung in the first few radiation lengths of the dump, the positron beam can continuously scan for resonant production of new resonances via e^+ annihilation off an atomic e^- in the target.

1 Introduction

Neutrino masses, the cosmological baryon asymmetry and dark matter (DM) are some experimental facts that remain unexplained within the fundamental physics framework known as the standard model (SM) of particle physics and call for physics beyond it. This might correspond to a whole new sector containing new particles, as well as new interactions. If such a sector exists, one possible reason why it has not been discovered yet is that the couplings between the new particles and the SM are so feeble that the whole new sector has so far remained hidden, even if the mass scale of the new particles, including the mediators of the new forces, is within the experimental reach. This scenario has triggered in recent years an increasing interest in many novel ideas to hunt for new physics at the intensity frontier. In particular, the so-called dark photon (DP) A', a massive gauge boson arising from a new $U(1)'$ gauge symmetry, can be considered as a natural candidate for a superweakly coupled new state because the dominant interaction with the SM sector might arise solely from a mixed kinetic term $(\epsilon/2)F'_{\mu\nu}F^{\mu\nu}$. The coupling ϵ between the $U(1)'$ and QED field strength tensors has values naturally falling in a range well below 10^{-2}, and constrained by different experimental considerations [1].

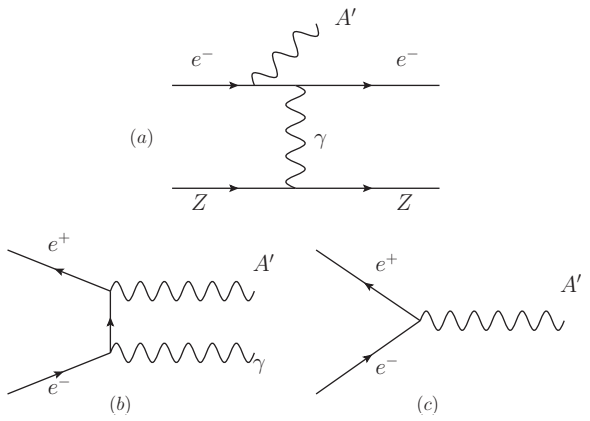

Figure 1: A' production modes in fixed target electron/positron beam experiments: (a) A-strahlung in e^--nucleon scattering; (b) A'-strahlung in e^+e^- annihilation; (c) resonant A' production in e^+e^- annihilation. Figure adapted from [4].

From the phenomenological point of view, light weakly-coupled new particles have been invoked to account for discrepancies between SM predictions and experimental results, such as, for example, the anomaly observed by the Atomki collaboration in the decay of excited ^{8}Be nuclei to the ground state [2]. This anomaly can be interpreted as due to the emission of a new boson with mass 17 MeV, i.e. the DP, in the decay $^8\mathrm{Be}^* \rightarrow {}^8\mathrm{Be} + A'$ followed by $A' \rightarrow e^+e^-$. This anomaly is particularly relevant since the new experimental technique that we are going to describe appears to be well suited to test (at least in some region of the parameter space) the particle physics explanation based on a new gauge boson with mass $m_{A'} \sim 17\,\mathrm{MeV}$, kinetically mixed with the photon [3].

2 Framework

2.1 The Beryllium Anomaly and DP constraints

The beryllium anomaly consists in the observation of a bump in the opening-angle and invariant-mass distributions of electron-positron pairs produced in the decays of excited ^{8}Be nucleus, which seems unaccountable by known physics. The anomaly has a statistical significance of 6.8σ which excludes the possibility that it arises as a statistical fluctuation. The shape of the excess is remarkably consistent with that expected if a new particle with mass $m_{A'} = 17.0 \pm 0.2(\mathrm{stat}) \pm 0.5(\mathrm{sys})\,\mathrm{MeV}$ is produced in these decays [2, 3]. In the Atomki setup, these decays must occur at a few-cm distance between the target, where the ^{8}Be excited state is formed, and the detectors. This implies a lower limit in the strength of the A' coupling to e^+e^- pairs given by $\epsilon \gtrsim 1.3 \times 10^{-5}$. Stronger limits than those imposed by the Atomki experimental setup are obtained from electron beam dump experiments and are showed in Fig. 3. From these limits we obtain $7 \times 10^{-5} \leq \epsilon \leq 1.4 \times 10^{-3}$ as the window allowed for a 17 MeV A' decaying dominantly into e^+e^- (visible decay) [4].

2.2 Beam dump experiments

Collider searches for DP have been carried out in fixed target experiments, which can be divided as:

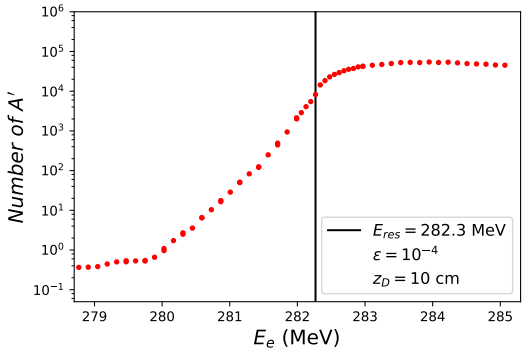

Figure 2: The number of DP decaying outside the dump as a function of the beam energy for $\epsilon = 10^{-4}$ and $z_D = 10\,\text{cm}$. The vertical line corresponds to the energy for resonant production of a 17 MeV DP [4].

1. Electron beam-dump experiments assuming A'-strahalung as the leading production mechanism in electron-nucleon scattering. Parametrically, this process is of order α^3 [5].

2. Positron beams where the production mechanism considered so far is analogous to the usual QED process of positron annihilation off an atomic target electron with two final state photons, where one photon is replaced by one A'. This corresponds to a process of $\mathcal{O}(\alpha^2)$ [6][1];

3. Resonant e^+e^- annihilation into on-shell A' which, being of $\mathcal{O}(\alpha)$, is parametrically enhanced with respect to the previous two production channels [4]. Besides experiments with positron beams, resonant annihilation must also be accounted for a correct analysis of electron beam dump experiments, since positrons are abundantly produced in the electromagnetic shower inside the dump [7];

These production mechanisms are depicted in Fig. 1(a-c), respectively. The last two are specific production processes considered in the PADME experiment at the DAΦNE LINAC Beam Test Facility (BTF) of the INFN Laboratori Nazionali di Frascati (LNF). This experiment is designed to search for DP by using a positron beam impinging on a thin (thick) target of low (high) atomic number. The experiment will use a 550 MeV positron beam impinging on a 100μm thin active target made of polycrystalline diamond ($Z = 6$) for the process 2 (Fig. 1(b)) and a tungsten target ($Z = 74$) of several cm of length (z_D =2, 5 and 10 cm) for the process 3 (Fig. 1(c)) [4].

2.2.1 *Resonant e^+e^- annihilation*

This new proposal to search for DP has several advantages that suggest that it might be particularly convenient to operate the PADME (as well as others) positron beam fixed target experiment in a dedicated mode in order to search for A' via resonant production. One of the advantages is due to the use of the thick target. In this case, it is possible to absorb most of the incoming positron beam, as well as the related electromagnetic showers, and in any case to degrade sufficiently the energy of the residual emerging particles, so that the background from charged particles can be easily deflected and disposed of. Also, the

[1]The A' can be detected in the invisible channel by searching for a narrow bump in the spectrum of the missing mass measured in single photon final states, originated via $e^+e^- \to \gamma A'$.

DP produced in e^+e^- annihilation, if sufficiently long-lived, will escape the dump without interacting and will decay inside the downstream vacuum vessel, producing an e^+e^- pair of well-defined energy. A second advantage is that using the thick target can provide an almost continuous energy loss for the incoming positrons propagating through the dump so that they can efficiently "scan" in energy for locating very narrow resonances [4]. In this scheme, we will estimate the sensitivity to the A' couplings that could be achieved with targets with $z_D = 2$, 5 and 10 cm in the PADME experiment. The number of detectable DP events is then given by (see reference [4] for more details):

$$N_{A'} = \frac{N_{e^+} N_0 X_0}{A} e^{-\frac{z_D}{\ell_\epsilon}} \int_0^{T=1} dt\, e^{\frac{X_0}{\rho \ell_\epsilon} t} \int_0^\infty dE_e \left[\int_0^\infty \mathcal{G}(E)\; I(E, E_e, t)\; dE \right] \sigma_{\rm res}(E_e)\,, \tag{1}$$

where $\mathcal{G}(E) = \mathcal{G}(E; E_b, \sigma_b)$ is a Gaussian that describes the energy distribution of positrons inside the BTF beam, with $250 \leq E_b/\text{MeV} \leq 550$ the nominal energy and $\sigma_b/E_b \sim 1\%$ the energy spread. $I(E, E_e, t) = \theta(E - E_e)[\log(E/E_e)]^{\frac{4}{3}t-1}/[E\,\Gamma(4t/3)]$ is the probability that a positron with initial energy E will have an energy E_e after traversing $t = \rho z/X_0$ radiation lengths (with ρ being the density of the material in g/cm^{-3} and $X_0 = 6.76\,\text{g/cm}^{-2}$ the unit radiation length in tungsten). $\ell_\epsilon \sim 3/(2m_e\alpha\epsilon^2)$ is the decay length of the DP, N_{e^+} the number of incident positrons, N_0 the Avogadro number, $A = 184$ the atomic mass of tungsten, and $\sigma_{\rm res}$ the resonant cross section given by (using the narrow width approximation):

$$\sigma_{\rm res}(E_e) = \sigma_{\rm peak} \frac{\Gamma_{A'}^2/4}{(\sqrt{s} - m_{A'})^2 + \Gamma_{A'}^2/4}\,, \tag{2}$$

where $s \simeq 2m_e E_e$, $\sigma_{\rm peak} \simeq 12\pi/m_{A'}^2$ and $\Gamma_{A'} \simeq \epsilon^2 \alpha m_{A'}/3$.

Taking into account Eq. (1) and assuming that the background remains constant when the beam energy is varied by a few MeV (as a consequence of the "scan" in energy), the background can be directly measured from the data and gives an estimate of the number of events created in the resonance annihilation mode. This is illustrated in Fig. 2 where we can see that when the beam energy is increased towards the resonance value (given by the vertical line) the number of produced e^+e^- pairs increases in a step-wise way up to a maximum, and then remains approximately constant with increasing energy, due to positron energy losses in the material, which drive their energy towards $E_{\rm res}$.

Effects of target e^- velocities

Inside materials, the electrons are not at rest and, in the case of large atomic numbers, like tungsten, can have large velocities. For positron annihilation in this type of materials, the center-of-mass energy can differ sizeably from what can be naively estimated in terms of the beam energy, energy spread, energy loss due to in-matter propagation, and assuming electrons at rest. Then, to take into account this fact, we consider the positron-annihilation probability distribution as a function of the electron momentum[2], $\mathcal{P}(v_e) = \left[1.015^{-v_e^2} + 1.112^{-2v_e} + \theta(v_e - 40)\, 3 \times 10^{-6+\frac{1}{v_e}}\right]/12$, replacing the Mandelstam variable s in Eq. (2) by [4]:

$$s(v_e, \chi) = 2m_e \left\{ E_e \left[1 - \mathcal{P}(v_e) v_e \frac{1}{2} s_\chi c_\chi \right] + m_e \right\}\,, \tag{3}$$

[2]Since annihilation with delocalized and weakly bound valence electrons, which contribute to the low-momentum part of the momentum distribution, is more likely than annihilation with the localized and tightly bound core electrons contributing to the high-momentum part (for more details see discussion about Fig. 3 in reference [4]).

$\epsilon \Big/ N_{A'}^{\rm prod}$	$E_{\rm res}$ $(v_e = 0)$	$E_{\rm res}$	$E_{\rm res} + 2\sigma_b$
1.0×10^{-3}	7.69×10^{11}	1.51×10^{11}	4.72×10^{11}
5.0×10^{-4}	1.81×10^{11}	3.79×10^{10}	1.17×10^{11}
1.0×10^{-4}	7.25×10^{9}	1.49×10^{9}	4.73×10^{9}

Table 1: Number of 17 MeV DP produced in the first radiation length of a tungsten target for three different values of ϵ. The second and third columns are for a beam energy tuned to the resonant value $E_{\rm res} = 282.3\,{\rm MeV}$, assuming the electron at rest and with the velocity distribution $\mathcal{P}(v_e)$, respectively. The last column, also including v_e effects, is for a beam energy $E_b = E_{\rm res} + 2\sigma_b$ [4].

where $c_\chi = \cos\chi$ accounts for the projection of $\vec{v}_e$ along the z-direction of the incoming positron and $s_\chi/2$ with $s_\chi = \sin\chi$ is the probability distribution for the angle χ. The cross section is also integrated over c_χ and $v_e \in [0, 0.06]$.

3 Results

Table 1 shows some results that illustrate how the number of DPs within the first radiation length of tungsten are modified when is considering v_e inside the target for different values of the parameter ϵ. The second column gives the results for a beam energy tuned at the resonant energy $E_{\rm res} = 282.3\,{\rm MeV}$, when the motion of the target electrons is neglected. Meanwhile, the third column gives the results obtained when the electron velocity is taken into account. From this table we can see that the shift due to the electron momentum has the effect of reducing the number of DPs produced by about a factor of five. The last column gives the results for a beam energy tuned above the resonance $E_b = E_{\rm res} + 2\sigma_b$. In this case, the number of DP is increased by about a factor of three regarding the number of DPs generated just at resonance. This is because of the "scan" in the positron energy inside the target.

In Fig. 3 the black hatched region depicts the forecasted sensitivity of PADME in thin target mode, which will search for DP via the $e^+e^- \to A'\gamma$ process. The light cyan trapezoidal regions represent the constraints that PADME could set by running in thick target mode, and are respectively for tungsten targets of 10 cm, 5 cm and 2 cm of length assuming zero background. The width of these regions spans the interval $16 \lesssim m_{A'}/{\rm MeV} \lesssim 23.7$ which corresponds to the Frascati BTF energy range for positron beams $250 \lesssim E_b/{\rm MeV} \lesssim 550$.

4 Conclusions

A new way to search for DPs, coupled to e^+e^- pairs, via resonant production in e^+e^- annihilation is suggested as an alternative method to test new physics at high intensity accelerators. This production mode together with the A'–strahlung in e^+e^- annihilation, are two complementary modes in the PADME experiment, since they can set new bounds in the regions of small $\mathcal{O}(10^{-4})$ and large $\mathcal{O}(10^{-3})$ values of the DP mixing parameter ϵ, respectively. With some intense and dedicated experimental efforts, the black-hatched region and the trapezoidal-shaped areas shown in Fig. 3 could be explored by the PADME experiment. In particular, the allowed window to produce, via resonant e^+e^- annihilation, the 17 MeV DP can be invoked to explain the ^{8}Be anomaly. A confirmation of the DP interpretation of the ^{8}Be anomaly (studying the inverse process $e^+e^+ \to A'$ at accelerators) at the intensity frontier, would possibly represent the discovery of a hidden sector and a particle physics breakthrough. The resonant $e^+e^- \to A'$ production can be relevant also in the case of electron beam dump experiments, since secondary positrons

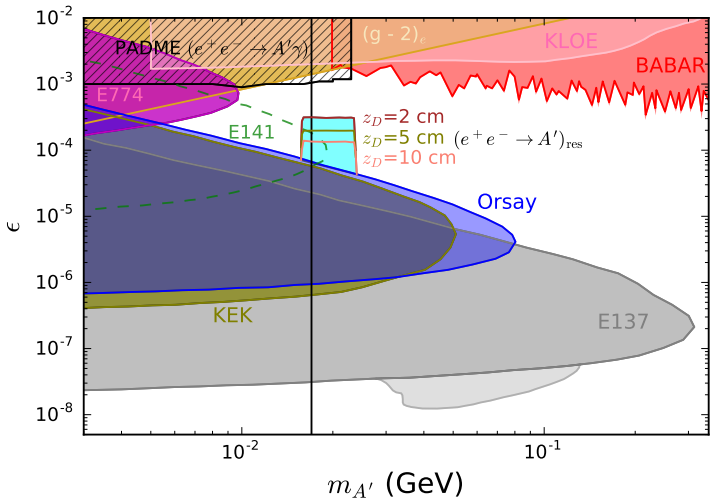

Figure 3: Limits on the DP kinetic mixing ϵ as a function of the mass $m_{A'}$ from different experiments. The region that could be excluded by PADME running in thin-target mode is hatched in black, while the three trapezoidal-shaped areas give the PADME reach in thick-target mode, respectively for a 10, 5 and 2 cm tungsten dump, assuming zero background [4].

that could trigger the annihilation process are abundantly produced in electromagnetic showers. This observation was recently exploited in a reanalysis of the SLAC E137 data which extend the previously excluded region towards smaller ϵ values, as is shown by the light gray area in Fig. 3 [7].

5 Acknowledgements

The author acknowledges COLCIENCIAS in Colombia (doctoral scholarship 727-2015) for financial support and the LNF Theory Group for hospitality and partial financial support to attend the XIX LNF Spring School "Bruno Touschek" in Nuclear, Subnuclear and Astroparticle Physics.

References

1. J. Alexander *et al.*, arXiv:1608.08632 [hep-ph]. B. Holdom, Phys. Lett. **166B**, 196 (1986).
2. A. J. Krasznahorkay *et al.*, Phys. Rev. Lett. **116**, 042501 (2016), A. J. Krasznahorkay *et al.*, EPJ Web Conf. **142**, 01019 (2017). A. J. Krasznahorkay *et al.*, EPJ Web Conf. **137**, 08010 (2017).
3. J. L. Feng, *et al.* Phys. Rev. D **95**, 035017 (2017).
4. E. Nardi, C. D. R. Carvajal, A. Ghoshal, D. Meloni and M. Raggi, Phys. Rev. D **97**, 095004 (2018).
5. J. D. Bjorken, R. Essig, P. Schuster and N. Toro, Phys. Rev. D **80**, 075018 (2009).
6. M. Raggi, V. Kozhuharov and P. Valente, EPJ Web Conf. **96**, 01025 (2015).
7. L. Marsicano *et al.*, Phys. Rev. D **98**, 015031 (2018), L. Marsicano *et al.*, Phys. Rev. Lett. **121**, 041802 (2018).

Frascati Physics Series Vol. 67 (2018)
6th Young Researcher Workshop 'Physics Challenges in the LHC Era'
May 7 and 10, 2018

FTK: AN HARDWARE BASED TRACKER FOR THE ATLAS EXPERIMENT

Simone Sottocornola
Universitá degli studi di Pavia - INFN sezione di Pavia

Abstract

During the Run-2 of the Large Hadron Collider (LHC) the instantaneous luminosity exceeds the nominal value of 10^{34} cm^{-2} s^{-1} with a 25 ns bunch crossing period and the number of overlapping proton-proton interactions per bunch crossing increases up to about 80. These conditions pose a challenge to the trigger system of the experiments that has to control rates while keeping a good efficiency for interesting physics events. In order to facilitate the use of tracks in the High Level Trigger, the ATLAS experiment planned the installation of a hardware processor dedicated to tracking: the Fast Tracker (FTK). It is designed to deliver full-scan tracks with p_T above 1 GeV to the ATLAS High Level Trigger system for every Level-1 (L1) accept. The Fast Tracker system will be massive, with about 8000 Associative Memory chips and 2000 field programmable gate arrays, providing full tracking with a rate up to 100 kHz and an average latency below 100 microseconds. This document provides an overview of the FTK system, as well as reports on the commissioning status.

1 Introduction

The first Large Hadron Collider data-taking period, concluded in 2012 using only a fraction of the full LHC potential, has already achieved fundamental successes, as the Higgs boson's discovery and the placement of strong limits on new physics phenomena. After a shutdown period of almost 2 years, the LHC has started with much higher instantaneous luminosity (see Fig. 1). In the Run-II period, it is providing 13 TeV collisions, almost twice the energy of the previous run, with an integrated luminosity of $\simeq 40$ fb^{-1} per year and, therefore, increasing the discovery potential of the experiments. The greater instantaneous luminosity, particularly after 2020, will provide an average number of simultaneous collisions (pileup) up to 80. In order to achieve the required online data reduction in the trigger and data acquisition system (TDAQ), essential to maintain the full discovery potential at such high luminosities and pileup (PU),

the LHC experiments need to increase the use of silicon detector information at the trigger level, reconstructing the track trajectories close to the interaction points, allowing the contribution of each pileup collision to be distinguished.
Because of its fine resolution and granularity, tracking information is critical for distinguishing which events triggered by L1 should be kept for further processing. However, extensive tracking in such environments is prohibitively expensive in terms of processing time per event or computing cores needed. Therefore, it is used sparingly for specific regions of interest (RoI), which have already been identified as potentially interesting by the Level-1 trigger and for full event tracking at low rates ($\simeq$ few kHz). This approach has limitations in several cases. First, there is a limit to either number or size of RoIs processed by the High Level Trigger (HLT), which forces additional non-tracking cuts to be applied, resulting in reduced efficiency or higher thresholds for the objects considered. Second, there are cases where global event information, such as the location of the hard-interaction vertex or number of primary vertices in the event, are useful for object selections or corrections to the other detector quantities. Both these problems are particularly critical for the trigger selection of signatures containing third generation fermions, such as τ or b-jets, for which tracking information is fundamental to keep the selection performances high.
In order to cope with these problems, the ATLAS experiment has decided to include, within the existing multilevel trigger architecture, an electronic system, the Fast TracKer (FTK) processor, designed to perform real-time full track reconstruction from the hits observed in the Inner Detector (ID).

2 The ATLAS trigger system

The trigger and data acquisition system (TDAQ) plays one of the most crucial roles in the whole experiment. Because of technology and resource limitations, only a part of the produced 4×10^7 events/s can be stored for further analysis, typically 1.5×10^3 events/s. In order to reduce the events rate while maintaining the maximum efficiency for the physics, data from events not physically interesting need to be rejected. Moreover, due to the trigger decision time which is much bigger than the 25 ns interval of bunch crossing, a multi-level data organization is required. In order to cope with such requirements, the ATLAS trigger system is composed of two levels: a hardware-based L1) trigger and a software-based High-Level trigger (HLT), as shown in Fig. 2 [2)]. The L1 trigger is implemented using custom-made electronics, while the HLT is almost entirely based on commercially available computers and networking hardware. The first level uses a limited amount of the total detector information, i.e. low granularity information from the muon spectrometer and the calorimeter system. It uses information coming from the muon tracks and electromagnetic and hadronic clusters to identify interesting regions of the detector containing high energy deposits, called regions of interest (RoI), and providing a rate reduction of a factor 400 in a latency time of 2.5μs. The High Level Trigger has instead access to the whole detector information within the regions defined by the first level, resulting in a final rate of up to about 2 kHz in a mean latency time of 200ms. The HLT selections are based on all the available detector information, at full granularity and precision. The HLT is based on a computing farm containing almost 2000 computers, called nodes, in which 40000 cores run the trigger code. If the HLT selection is successful, the full event is then reconstructed. All the data fragments coming from different detectors are collected in a single record, which is transferred to the Data Logger for its storage in the local disks.
Because of the long computational time required to reconstruct the tracks, in the current trigger system tracking information are only used at the HLT level for the RoI defined by the L1, and only for a subset of events. FTK will perform full track reconstruction on all the L1 accepted events, enabling the HLT to have access to tracks in the entire silicon detector at an earlier event selection stage, allowing a drastic

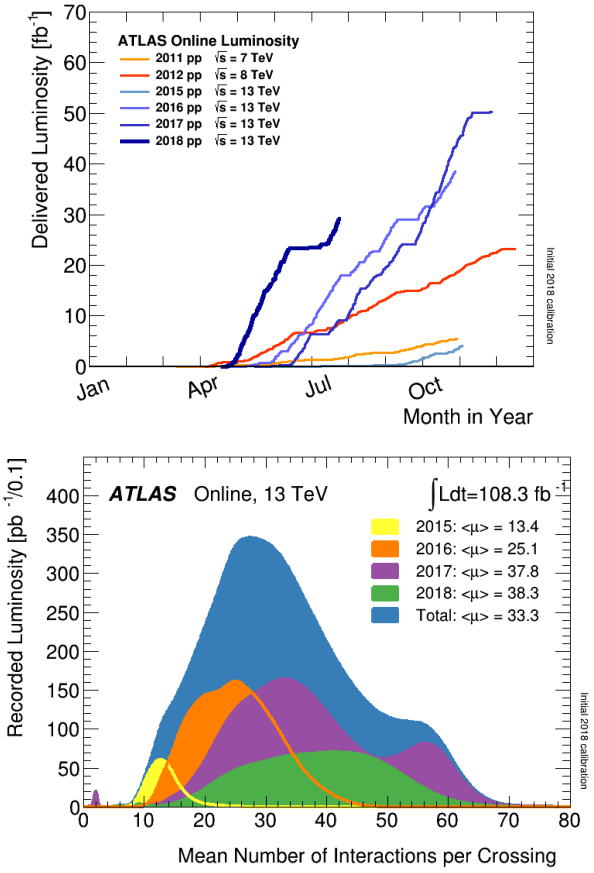

Figure 1: *Top) Luminosity delivered by the LHC from 2011 to 2018. Bottom) Mean number of interactions per Crossing from 2015 to 2018.* [1)]

increase in the trigger efficiency for a large group of different signatures.

3 FTK operational principle

The FTK system is composed of electronic boards of 6 different types, as shown in Figure 3. The Input Mezzanines (IM) and Data Formatter (DF) boards receive hits from twelve layers of the ATLAS Pixel and Semiconductor Tracker (SCT) detectors and groups them into clusters of nearby hits in order to reduce the data size. The clustered hits are then sorted into 64 regions and sent downstream for parallel processing. Upon entering the processing units, i.e. auxiliary board (AUX) and associative memory board (AMB) pairs, the hits are stored in full resolution, meaning they contain all of their original cluster information. While the full resolution hits are stored on input Field Programmable Gate Arrays (FPGA) in the processing units, the remaining FPGAs and application-specific integrated-circuit (ASIC) chips process the hits by grouping them in coarser resolution segments. During this courser resolution processing, the Pixel and SCT detectors are not viewed as individual modules, but groupings of modules called super-strips. For eight of the twelve layers, the processing units identify which super-strips the clustered hits belong to. The selected super-strips are then compared to Monte Carlo (MC) track patterns

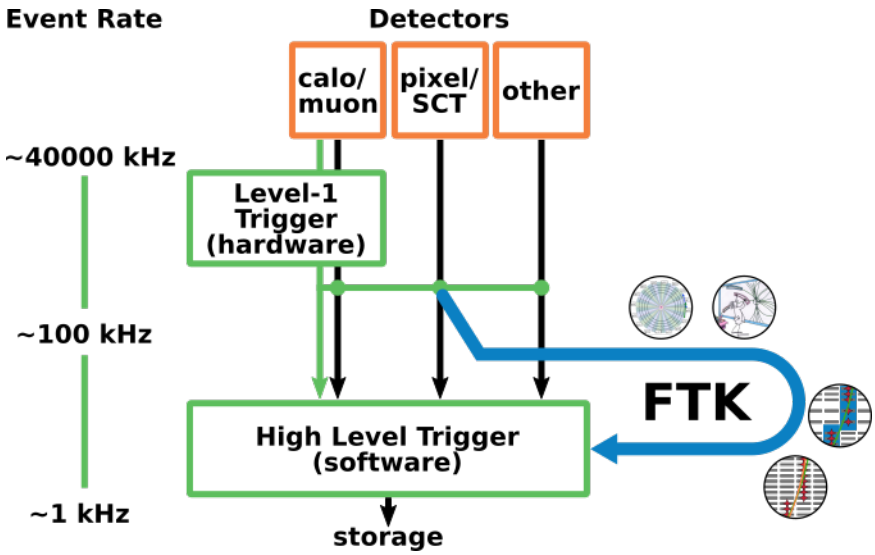

Figure 2: *Sketch of the ATLAS trigger system.*

stored in associative memories. In standard computer memory, once a user supplies a memory address, the RAM returns the data word in that address. By contrast, in associative memory the user inputs a data word and the entire memory is searched in order to find that word. Thus when the associative memory finds a MC track pattern that matches the selected super-strip, returns it and calls it a "road". For each road, the full-resolution hits stored on the PU-input FPGA are retrieved and a goodness of fit is determined using a χ^2 test for eight layers. The eight-layer tracks are then combined with the hits from the remaining four layers and a full twelve-layer track fit is performed inside the SSB boards. The twelve-layer tracks are then sent to the HLT via the FLIC boards.

4 FTK system architecture

Figure 4 depicts a sketch of the FTK architecture. As said in the previous section, FTK uses Associative Memory (AM) chips, which are custom designed ASICs, to perform pattern matching, along with numerous FPGAs for the detailed track fitting and other needed functionalities. Data from the ID Read-Out-Drivers (RODs) are transmitted to the FTK Input composed of IM and the mother DF boards. The IMs receive the data and perform one- or two-dimensional cluster finding in the SCT or in the Pixel/IBL detectors, respectively. The DFs reorganize the ID data into projective $\eta - \phi$ towers and distribute the cluster centroids to the respective Processing Units, where pattern matching and track fitting take place. The division of the FTK into $\eta - \phi$ towers is done to achieve maximum parallelization. In total, 64 $\eta - \phi$ towers are used; 16 in ϕ (azimuthal angle) and 4 in η (pseudorapidity $|\eta| < 2.5$). There are 8 $\eta - \phi$ towers in a crate, with a 10 overlap between neighboring crates in ϕ (same crate boards overlap is also present). Data Organizers (DO) on the AUX receive the hits coming from DFs and convert them to coarser resolution hits (the so-called Super Strips), which are appropriate for the pattern matching performed by the AM chips. The Associative Memory boards (AMB) contain roughly 8.2 million patterns each in the AM chips, corresponding to the possible combinations of Super Strips in the eight silicon layers. The AM is a massively parallel system in which all patterns see each silicon hit nearly simultaneously. As a

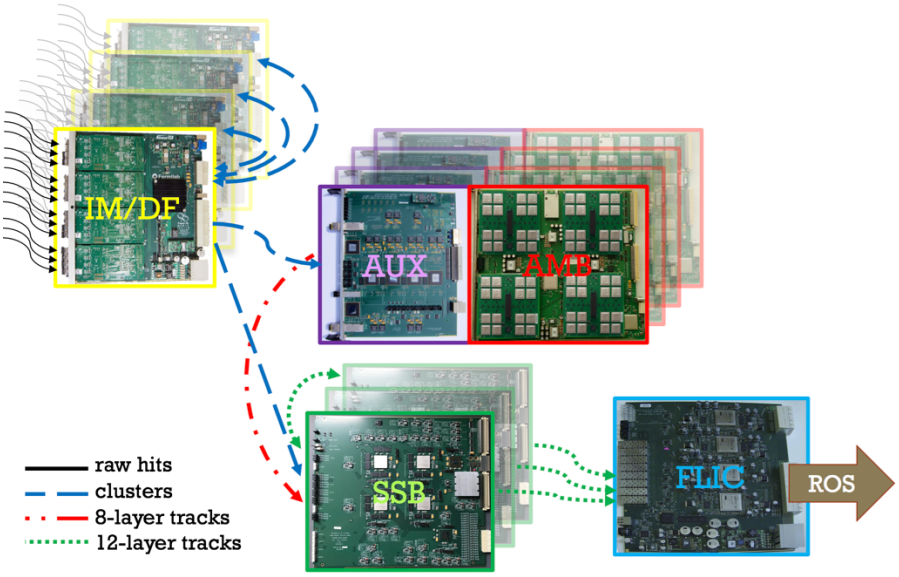

Figure 3: *Sketch of the internal dataflow of FTK. The lines represent the communication links between different boards.*

result, pattern recognition in FTK is completed shortly after the last hit has been transmitted from the ID RODs. The matched patterns are referred to as "roads" containing track candidates. When a pattern has seven or eight layers matched, the AM sends the road identifier back to the DO which fetches the associated full resolution hits and sends them, together with the road identifier, to the Track Fitter (TF). The TF has access to a set of constants for each detector sector, which consists of eight physical silicon modules, one for each layer. The TF calculates track parameters linearly based on these pre-calculated constants using the formula:

$$p_i = \sum_j c_{ij} x_j + q_j \qquad \forall i = 1...5, \tag{1}$$

where p_i represent the five track parameters, x_j are the cluster local coordinates and c_{ij}, q_j are the constants used in the linearized formula. After fitting in each road, duplicate track removal (the Hit Warrior or HW function) is carried out among those tracks which pass the χ^2 cut. When a track passes the first stage criteria, the road identifier and hits are sent to the Second Stage Boards (SSB). The SSBs receive from the DFs the cluster centroids in the four layers not used in the previous stage. The track is extrapolated into the four additional layers, nearby hits are found, and a full 12-layer fit is carried out. A minimum of three hits in these four layers is required. Duplicate track removal is again applied to the tracks that pass the χ^2 test, but now the tracks in all roads are used in the comparison. The SSBs also share track data with each other for $\eta - \phi$ overlap removal. There are three main functions running on different FPGAs: the Extrapolator that computes likely positions of hits in the other four SCT layers, the Track Fitter, that determines the helix parameters and the track quality χ^2 for road hits of all 12 silicon layers, and the Hit Warrior. SSB output tracks consisting of the hits on the track, the χ^2, the helix parameters, and a track quality word that includes the layers with a hit are sent to the FTK-to-Level2 Interface Crate (FLIC). The FLIC performs the look-up for the local FTK to global

ATLAS hit identifiers and sends them to the Readout System (ROS), sending them to the High Level Trigger via the ATLAS ReadOut System.

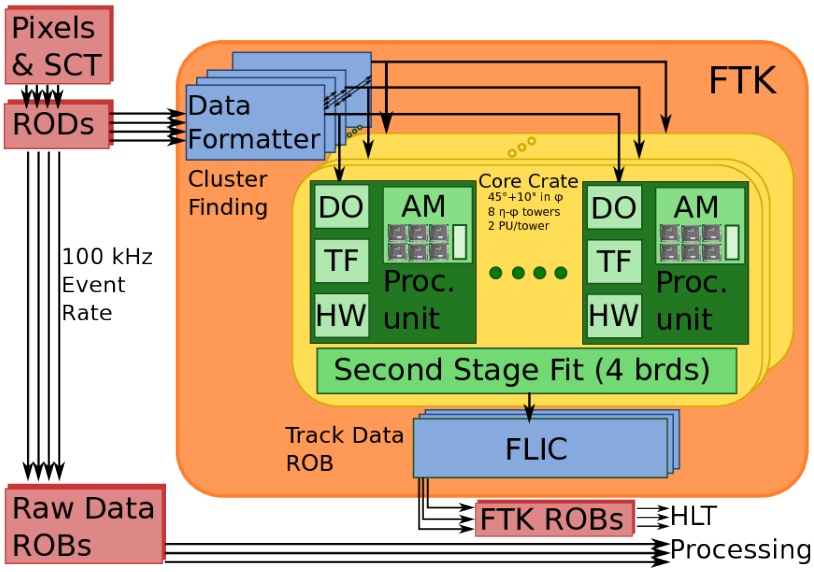

Figure 4: *Functional diagram of the FTK components. DF reorganizes hits coming from ID Read-Out Drivers and propagates it to the DO. The DO organizes hits for pattern matching and sends it to the AMB. Track Fitter calculates track parameters for patterns matched. Hit Warrior removes duplicate tracks. Second Stage Fit (on SSB) extrapolates tracks for twelve ID layers. FLIC re-formats FTK output to ATLAS global coordinates and sends it to Read OutBuffers.*

5 FTK expected performances

The tracks delivered from FTK to the HLT will have a very similar quality as the one achieved in the offline reconstruction, but with a much faster processing time. The latency of the FTK system is expected to be within 100 μs, leaving ample time for the tracks to be used as input to HLT algorithms. This will lead to a drastic increase of the trigger performances, particularly regarding the third-generation fermion selection.

Concerning b-jets, FTK is foreseen to enhance the trigger selection efficiency in three different areas. Firstly, FTK can improve upon the single-jet b-tagging performance in RoIs for which the current trigger system will run the b-tagging. Refitting the FTK tracks allows the ATLAS trigger system to have offline quality tracks at HLT-like latencies. The reduction in tails and improvement in resolution of the impact parameter provided by the refitted tracks (with respect to raw FTK tracks) will improve the b-tagging performance over the current HLT system. Fast tracking will also save and free CPU time allowing to run more advanced and time-consuming taggers. The second area concerns the reduction of the p_T thresholds on the b-tagged jets. The current system reduces the RoI-rate output from level-1 with a p_T cut as a first step. This brings the rate at a level at which the HLT tracking and b-tagging can be run. Running b-tagging on the full level-1 output rate first will allow lower thresholds, gaining acceptance for jets with $p_T \leq 50$ GeV, as shown in Figure 5 (top). Finally, FTK can improve the b-jet trigger by running full-scan b-jet finding and tagging, independently of the RoIs found by the level-1 processors. This will allow

b-tagging to be run for high-rate level-1 items and for arbitrarily low p_T thresholds, increasing signal acceptance.

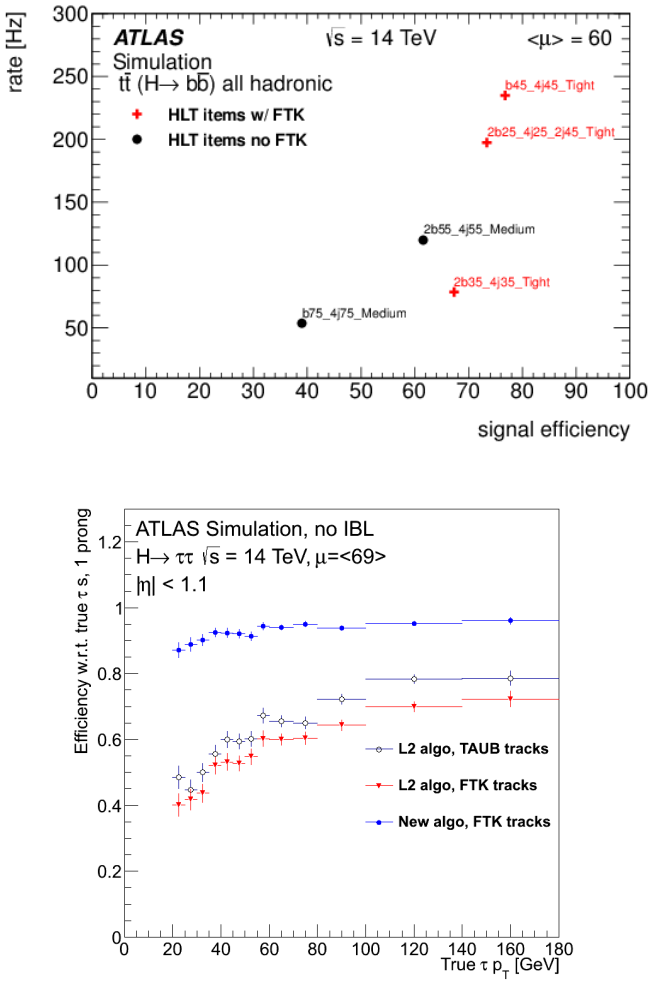

Figure 5: *Top) The plot summarizes the impact of the FTK b-tagging described in the FTK TDR* [4]*, updated to include the use of the IBL and the refit of FTK tracks. Bottom) Efficiency of the Level 2 algorithms with respect to true 1-prong τ p_T. Three working point are shown: black is the efficiency for the standard L2 algorithm, the red shows the efficiency for the Level 2 style algorithm using FTK tracks and the blue shows the efficiency for the FTK track-based algorithm.*

Concerning τ leptons, and in particular their hadronic decays, FTK will greatly improve the trigger performance, especially for low-p_T particles. Because the tracking information is not available at the level-1 selection stage, currently a calorimeter-based selection requiring a narrow isolated jet is used. The selection algorithms apply a severe calorimetric selection in order to reduce the RoI rate to a sustainable level for the tracking algorithms. This two-step approach produces a RoI reduction factor of 4-5, but results in a large signal-efficiency loss. The FTK system will provide tracks and primary vertices at the HLT input rate, allowing for a re-evaluation of the trigger strategy for both single-τ RoIs and complex multi-object signatures. Moreover, for the single-τ RoI, track information can also be used to pre-select

the hadronic τ-decay topology with a high enough rejection of the QCD background such that algorithms similar to the offline τ-identification algorithms could be run, as shown in Figure 5 (bottom). In multi-object signatures, the primary vertex information can be used to require that the objects are consistent with being produced at the same vertex, in order to decrease the effect of pile-up collisions.

6 Commissioning status

The FTK system is currently being commissioned. At the moment of this article all IM-DF boards, FLICs and AUX-AMB pairs are installed in their respective ATCA (Advanced Telecommunication Computing Architecture) and VME (Versa Module Europa) crates (while some of the SSB boards are still missing and will be delivered to CERN in the next months). The cabling of the boards has been completed, and the infrastructure installation, as well as the installation of the custom VME cooling system, are completed. The commissioning of the FTK system in this phase is focused on "Slices" (portion of the system composed by a single board per type). Since the beginning of this year FTK has two slices fully integrated in the ATLAS data-taking architecture which are regularly taking data. The first one, called "SliceA", is composed by a single FTK board per type and it is able to output 12-layer tracks. The data from this slice are written into the ATLAS event data stream. This year, for the first time, we were able to write the first 12-layer validated FTK tracks in the ATLAS data stream. The second Slice, called "Slice2", is composed by the three upstream boards and outputs 8-layer tracks. It is used to commission the upstream boards while the downstream ones are undergoing debugging. Work is also ongoing on the scaling up of the system. During this year we were able to establish successfully the intercommunication between a full shelf of DFs. The communication between multiple DFs and PUs was also achieved, starting with simulated data and finally with real data coming from the ATLAS Inner Detector. The scaling up of the FTK system has started from a third Slice, called "Slice47", which will be its seed. The plans for the 2018 are to be able to commission the so called "hemisphere", represented by the barrel part of the system, with the commissioning of the last part of the system to be carried out during the LHC Long Shutdown period.

References

1. https://twiki.cern.ch/twiki/bin/view/AtlasPublic/LuminosityPublicResultsRun2.
2. ATLAS collaboration, ATLAS detector and physics performance: Technical Design Report, CERN-LHCC-99-014.
3. ATLAS collaboration, ATLAS inner detector: Technical Design Report, CERN-LHCC-97-016.
4. ATLAS collaboration, Fast Tracker: Technical Design Report, CERN-LHCC-2013-007.

Frascati Physics Series Vol. 67 (2018)
6th Young Researcher Workshop 'Physics Challenges in the LHC Era'
May 7 and 10, 2018

CONSTRUCTION PROCEDURE AND FIRST TESTS OF THE SM1 TYPE MICROMEGAS CHAMBERS FOR THE NEW SMALL WHEEL WITHIN THE PHASE 1 UPGRADE OF THE FORWARD MUON SPECTROMETER OF THE ATLAS EXPERIMENT

G. Mancini on behalf of the ATLAS Muon Collaboration
LNF INFN, Frascati, Italy

Abstract

MICRO MEsh GASeous structure chambers, MicroMegas (MM), are an innovative design concept for Micro-Pattern Gaseous Detectors, designed in order to provide high performances, in terms of spatial resolution and efficiency, even with highly irradiated environments. These chambers have been chosen as new precision tracking detectors for the upgrade of the forward muon spectrometer of the ATLAS experiment. MM trapezoidal detector modules, with areas between 2 and 3 m^2, will be part of the two New Small Wheels (NSW) composing the innermost station of the ATLAS muon tracking forward system. MM detectors are composed by 4 read-out layers, two for the reconstruction of the precision coordinate and two with stereo reading ($\pm 1.5^\circ$) for the reconstruction of the second coordinate. MM chambers are designed to provide efficiency better than 95% per single plane at rate capability up to 15 kHz/cm^2, in presence of magnetic fields up to 0.3 T. The Istituto Nazionale di Fisica Nucleare (INFN) is deeply involved in the construction of these chambers and in their validation at the Cosmic Ray Stand (CRS) in the Frascati National Laboratories (LNF) of the INFN. Preliminary results on the validation method and tests performed on INFN SM1 prototype are presented.

1 Introduction and operating principles

The Micromegas chamber is made up of a read-out structure (anode) based on a Printed Circuit Board (PCB), a fine micro-mesh, which defines the separation between the conversion and the amplification region, and a cathode also based on a PCB [1)]. A schematic view of the working principle of a MM chamber is shown in Figure 1. These Micromegas (MM) chambers are filled with a gas mixture of Argon and Carbon Dioxide with a fraction of 93% - 7%, respectively, both in the conversion and amplification region. The read-out PCBs consist of photo-lithographically etched copper strips, on top of which an additional layer done with resistive strips on a kapton foil is glued. The resistive strips have a resistivity

of $\sim 10\ M\Omega/cm$ and are aligned with the read-out strips (300 μm wide); they have both a pitch of the order of 500 μm. The height of the conversion drift region ($E_{drift} \simeq 60\ kV/m$) and of the amplification region ($E_{read-out} \simeq 50\ MV/m$) are different and they are respectively 5 mm and 128 μm. Such a small amplification gap is guaranteed by the presence of insulating pillars with a diameter of 0.3 mm and a height of 128 μm, which keep at a constant distance the mesh from the top of the resistive layer. Th charged particle pass through the detector ionizes the gas in the conversion gap ($\sim 100\ pairs/cm$) and the produced electrons move towards the mesh. The electrons, passing through the mesh, produce an avalanche in the amplification region whose charge is collected on the resistive strips and read by the read-out strips (capacitively coupled to the resistive ones). This structure guarantees a high transparency of the micromesh and a fast ($\sim 100\ ns$) evacuation of positive ions produced in the avalanche through the micromesh. Two out of the four layers have strips parallel to the bases of the trapezoidal shaped MM (aiming for the precision coordinate reconstruction), while the others are inclined by $\pm 1.5°$, from which information on both the precision coordinate and the 2^{nd} coordinate can be obtained.

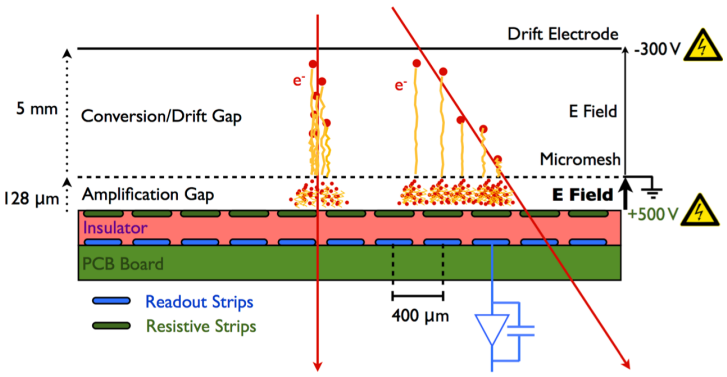

Figure 1: *Schematic view of the working principle of a MM chamber.*

2 The New Small Wheel (NSW): MM for the ATLAS upgrade

The NSW will replace the innermost station of the forward muon spectrometer in the end-cap region of the ATLAS detector [2]. The upgrade will give an improvement with respect to the performances of the current Small Wheel (SW) in terms of trigger and tracking efficiency in view of the increasing luminosity for the next LHC Runs (up to $5 - 7 \times 10^{34}\ cm^{-2}\ s^{-1}$). Two different detectors will be used for this purpose: Micromegas (aiming for precision tracking) and sTGCs (focused on the trigger). The NSW has a wheel-like structure and it is composed by 8 large sectors (LM) and 8 small ones (SM) and each sector is in turn made up of 4 MM modules (2 x 2 modules arranged one above the other) as shown in Figure 2 [3]. Four type of chambers are being constructed, namely LM 1-2, SM 1-2 whose production is distributed between several industries and institutes: Italy (SM1), Germany (SM2), France (LM1), Russia-Greece-CERN (LM2).

3 SM1 production scheme

The INFN group is responsible of the SM1 quadruplet construction. The main challenge of the construction of this type of chambers consists in observing the mechanical precision requirements made by the

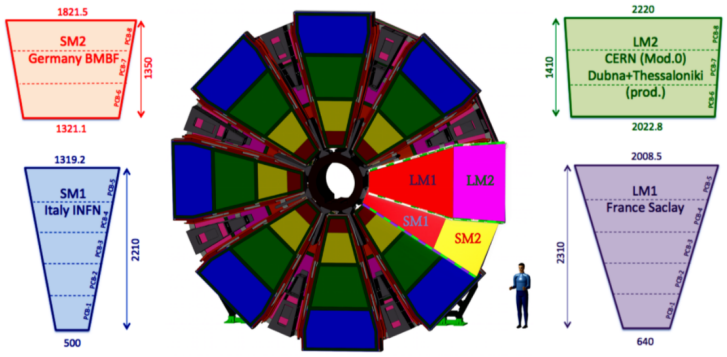

Figure 2: *Wheel-like structure of the NSW highlighting the 4 MM modules (LM 1-2, SM 1-2) and the construction sites.*

Table 1: *Total fraction of the panels being produced within the INFN NSW Consortium.*

	Fraction of the total produced
Drift panels (RM1)	50 / 96
Mesh Stretched (RM3)	39 / 128
Finalized Drift panels (LNF CR2)	26 / 96
RO panels - Eta (PV)	5 / 32
RO panels - Stereo (PV)	4 / 32
Quadruplets (LNF CR1)	3 / 32

ATLAS experiment. In particular, the constraints to be respected on the read-out strip alignment are very strong: within 30 μm in η (precision coordinate) and 80 μm in z axis which depends to the chamber planarity. As previously described, a single quadruplet is formed by 5 panels, 3 finalized drift panels [1] (2 outer and a central) and 2 read-out panels in order to define the four gas gaps of a quadruplet. Figure 3 shows the SM1 production scheme, together with a picture showing the vertical assembly. Table 1 shows the total fraction of the panels being produced up to now.

4 Preliminary results on first prototypes

The read-out electronics used for the prototypes is based on APV25+SRS modules operating at 40 MHz (final version will be VMM ASICs). The APV25 are 128 channels chips whose signal corresponds to the values of the collected charge for different time samplings. For each event and each channel, a total of 18 samples (every 25 ns for a total integration window of 450 ns), was recorded. The value of the charge and the time of arrival of the signal for each strip is obtained by performing a Fermi Dirac fit. Mod0 has been tested at the CERN H8 beam line of the SPS (π^+ beam at 180 GeV/c with a frequency between $1 - 500kHz$ and beam spot of 1×1 cm^2) using 5 Tmm chambers as external tracking chambers [2]. Pedestal has been subtracted from the collected charge and cross-talk effects between strips have been taken into account before the track hit reconstruction. From the measurements performed on Mod0 (at

[1] A drift panel is finalized when the previously stretched micro-mesh is glued on the bare drift panel.

[2] Bulk-type MM with resistive strips (10×10 cm^2 of active area, 150 μm strip width and 250 μm strip pitch) [4].

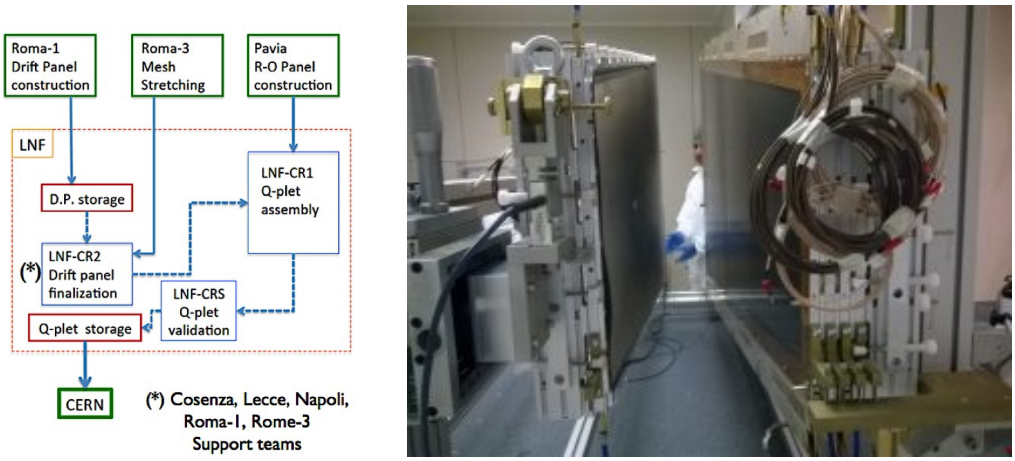

Figure 3: *The SM1 production scheme is reported (left) together with a picture showing the vertical assembly (right).*

CERN H8), the resolution on the precision coordinate is found to be 81 μm, while the resolution on the second coordinate is found to be 2.3 mm, both in agreement with the requirements of the chambers. Mod0 has also been tested with cosmic rays (at the cosmic ray stand at the LNF) using a tracking system composed of 2 Tmm. The measurements show an efficiency of the chamber higher than 95% per single layer, again well within the requirements. The same studies with cosmic rays were also carried out on the second prototype of SM1 (Mod 0.5) obtaining efficiency similar to those shown with Mod0. Results are shown in Figure 4.

5 Conclusions

MM chambers will be used after Long Shutdown 2 (LS2) for the precision tracking in the NSWs of the ATLAS experiment. The INFN group has been the first to construct 2 full size prototypes (SM1 Mod0 and Mod0.5) and the performances of those quadruplets have been found to be within expectations in terms of efficiency and resolution for perpendicular tracks. HV instability effects emerged on the first built chambers and have been largely solved by defining a proper cleaning procedure of the chamber before assembly. The assembly and test procedures have been validated and production has already started.

References

1. Y. Giomataris, P. Rebourgeard, J. Robert and G. Charpak, A High granularity position sensitive gaseous detector for high particle flux environments, Nucl. Instrum. Meth. A 376 (1996) 29.
2. ATLAS collaboration, New Small Wheel, Technical Design Report, CERN-LHCC-2013-006 (2013).
3. T. Alexopoulos et al., Development of large size Micromegas detector for the upgrade of the ATLAS muon system, Nucl. Instrum. Meth. A 617 (2010) 161.
4. T. Alexopoulos et al., A spark-resistant bulk-Micromegas chamber for high-rate applications, Nucl. Instrum. Meth. A 640 (2011) 110.

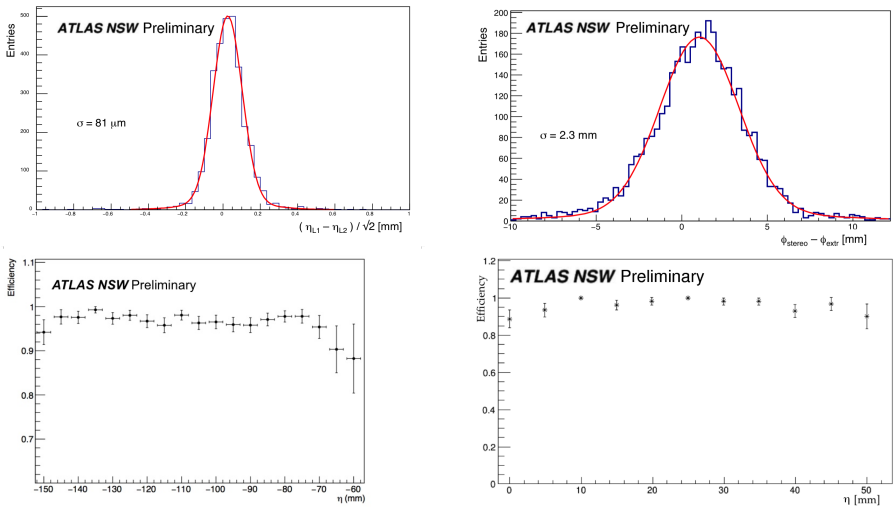

Figure 4: *Resolution on the precision coordinate (top left) and second coordinate (top right) of the Mod0 tested at the CERN H8 beamline. Efficiency of the Mod0 (bottom left) and Mod0.5 (bottom right) tested at the LNF CRS.*

Frascati Physics Series Vol. 67 (2018)
6th Young Researcher Workshop 'Physics Challenges in the LHC Era'
May 7 and 10, 2018

PRELIMINARY STUDY FOR $t\bar{t}$ RESONANCE SEARCH IN DILEPTON CHANNEL AND PERFORMANCE OF MUON RECONSTRUCTION CLOSE TO JETS IN ATLAS

Maurizio De Santis on behalf the NPTEV-TQP2020 group
INFN and University of Roma Tor Vergata

Abstract

A preliminary study on a search for resonances decaying to $t\bar{t}$ in the dilepton channel is presented. From these decays, the spin-correlation information is exploited in order to search for physics phenomena. A preliminary check using simulated samples has been done. Moreover, a study on the reconstruction efficiencies for muons close to jets, useful for high-$m_{t\bar{t}}$ invariant mass is presented. The first reconstruction efficiencies for muons close to jets in the ATLAS detector are also presented in this article.

1 The $t\bar{t}$ resonance

1.1 Introduction

The top quark is the heaviest fundamental particle in the Standard Model. The lifetime of the top quark is shorter than the timescale for hadronisation ($\sim 10^{-23}$ s) and much shorter than the spin-decorrelation time [1] ($\sim 10^{-21}$ s). As a result, the spin information of the top quark is transferred directly to its decay products. The top quark can be used as a probe to search for Beyond Standard Model (BSM) phenomena: in particular, it is possible to observe and characterise the BSM phenomena through the search for $t\bar{t}$ resonances and spin correlations near the resonance.
In this article the $t\bar{t}$ pair is studied in the dilepton final state. The dilepton final state is defined when both W bosons originated from top decay $t \to Wb$ in turn decay leptonically in a charged lepton and a neutrino, $W^{\pm} \to \ell^{\pm}\nu$ (with $\ell = e, \mu$ or τ), as shown in Fig. 1 (left). The dilepton channel represents only about 10% of the total Branching Ratio (BR) of top-pair decays, as shown in Fig. 1 (right) and only ee, $e\mu$ and $\mu\mu$ final states are taken into consideration here (including muons from the τ-lepton decay).
In this analysis the dilepton final state is studied inasmuch it is easier to measure the spin correlation of tops, using the direction of the outgoing leptons from W decay. Furthermore, it is interesting to combine

a variable that is sensitive to spin correlation (e.g. $|\Delta\phi|$) with the invariant mass $m_{t\bar{t}}$ or a transverse-mass proxy for the $t\bar{t}$ system. In these proceedings the $|\Delta\phi|$ and the invariant mass $M_{\ell\ell}$ ($\ell = e, \mu$ originated from W decay) are presented.

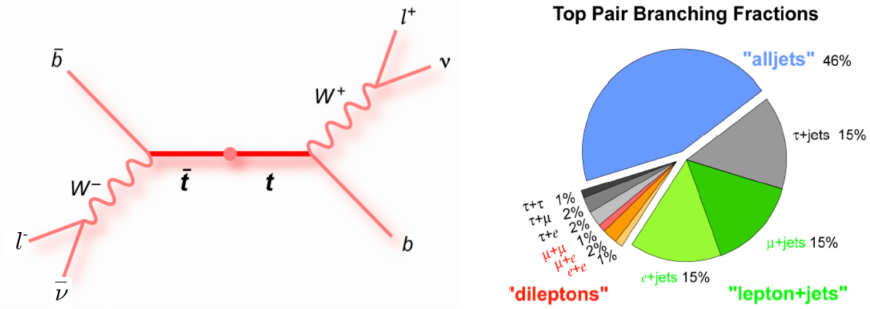

Figure 1: *Left: Schematisation of the $t\bar{t}$ decay process in the dilepton channel. Right: Pie chart of the total BR of the $t\bar{t}$ decay.*

1.2 Event Selection

This analysis utilizes reconstructed electrons, muons, jets and missing transverse energy (MET)[1]. Jets are reconstructed with the anti-k_t algorithm [2)], using a radius parameter $R = 0.4$ for topological clusters of energy deposits in the calorimeters; jets are accepted if they satisfy $p_T > 25$ GeV and $|\eta| < 2.5$[2]. Moreover, jets likely to originate from pile-up are suppressed using a multivariate jet-vertex-tagger (JVT) [3)] for candidates with $p_T < 60$ GeV and $|\eta| < 2.4$ and pile-up effects on all jets are corrected using a jet-area method.

Electrons are accepted if they satisfy $p_T > 25$ GeV and $|\eta| < 2.5$, excluding the range $1.37 < |\eta| < 1.52$ (i.e. electron candidates are excluded if the calorimeter cluster is within the transition region between the barrel and the endcap of the electromagnetic calorimeter). Moreover, tracks associated with electron candidates must satisfy the requirements $|d_0^{sig}| < 5$, where d_0 is the transverse impact parameter with respect to the beamline and the significance is the ratio between d_0 and its error, and $|z_0 \sin\theta| < 0.5$ mm, where z_0 is the longitudinal impact parameter of the track with respect to the primary vertex and θ is the polar angle.

Muons are accepted if they satisfy $p_T > 25$ GeV and $|\eta| < 2.5$. Tracks associated with muon candidates must satisfy the requirements of transverse impact-parameter significance $|d_0^{sig}| < 3$ and longitudinal impact parameter $|z_0 \sin\theta| < 0.5$ mm. For all subchannels (ee, $\mu\mu$ and eμ), the missing transverse energy is required to satisfy MET > 60 GeV.

1.3 Data and Monte Carlo simulations

In this analysis the data of the years 2015+2016 (~ 36.5 fb^{-1}) and 2017 (~ 80 fb^{-1}) will be used, recorded in pp collision at the ATLAS experiment, at a center-of-mass energy of $\sqrt{s} = 13$ TeV. Samples have been

[1]The missing transverse energy is defined as the transverse-plane projection of the vectorial sum of all momenta associated with all particles under study, changed in sign, which corresponds to the transverse energy carried by invisible particles (neutrinos).

[2]The pseudorapidity η is defined as $\eta = -\ln(\tan(\theta/2))$ where θ is the angle with respect to the beam axis.

simulated for the following processes: $t\bar{t}$ production is simulated with POWHEG+PYTHIA 8 [4, 5]. The diboson (ZZ, WZ, WW) and Z+jets backgrounds are simulated with the SHERPA NLO code [6] and single-top production with POWHEG+PYTHIA 6.

1.4 Studies on kinematics

A preliminary studies on kinematics has been performed, as shown in the following figures. Fig. 2 shows the number of jets in the three dilepton channels (ee, $\mu\mu$ and eμ respectively); it is possible to see that, for the electron-electron and muon-muon cases, there is a significant background from diboson and Z+jets. For the electron-muon case, the main backgrounds are dibosons and single top. Fig.s 3 and 4 shows the angular difference $\Delta\phi$ for $M_{\ell\ell} < 300$ GeV and $M_{\ell\ell} > 300$ GeV, respectively. It is possible to see that the distribution increases with large $\Delta\phi$, with a maximum when $\Delta\phi = \pi$.

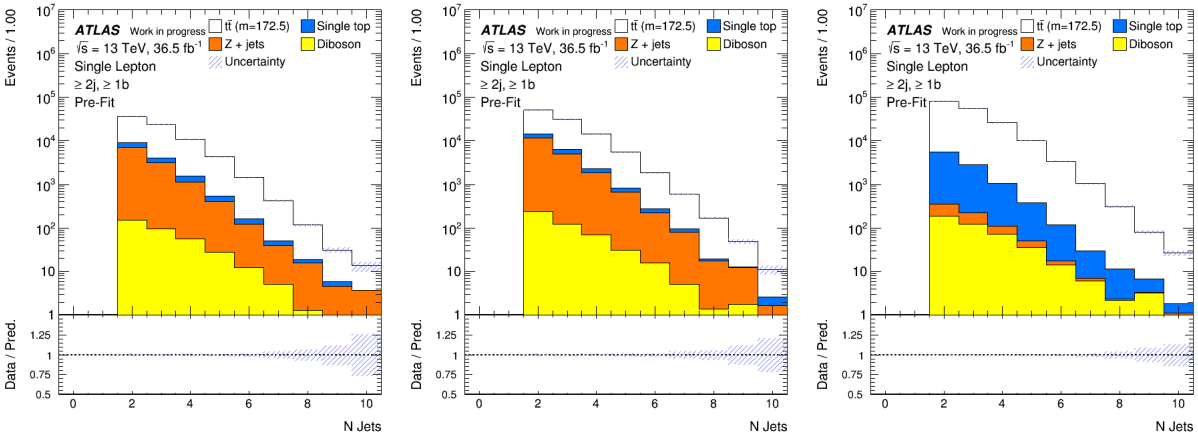

Figure 2: *Left: Number of jets in the electron-electron final state. Center: Number of jets in the muon-muon final state. Right: Number of jets in the electron-muon final state.*

1.5 Next steps

The next steps planned for the analysis are: (i) building a proxy for the $t\bar{t}$ invariant mass which contains the neutrino and b-jets (jets originated from a bottom quark) information; (ii) evaluating the sensitivity to BSM signals with MC simulations and a simplified analysis; (iii) based on this simplified analysis, choosing the best variable or combination of variables to be used as observables; (iv) comparing simulation with data to test differences in the spin correlation as a function of the $t\bar{t}$ invariant mass and, if no significant deviation is observed, extracting exclusion limits on various new physics models.

2 Performance of muon reconstruction close to jets

2.1 The importance of muons close to jets

In the $t\bar{t}$-resonance analyses, in particular the case with a high invariant mass m_{tt} where the muons are very close to the b-jets, the information about the performance of muon reconstruction near those jets is

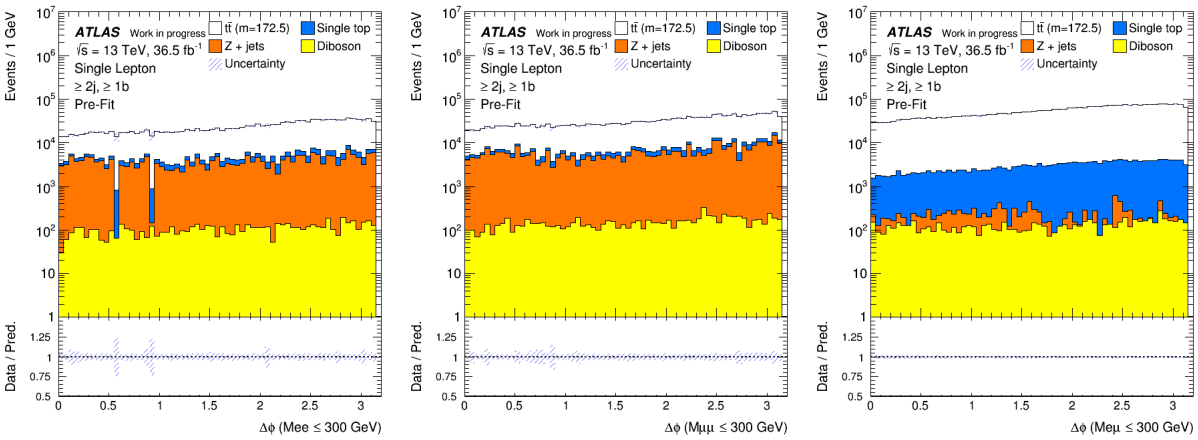

Figure 3: *Angular difference $\Delta\phi$ between the two charged leptons originated from W-boson decay. The events are restricted to the invariant mass of the two charged leptons $M_{\ell\ell} < 300$ GeV. Left: electron-electron final state. Center: muon-muon final state. Right: electron-muon final state.*

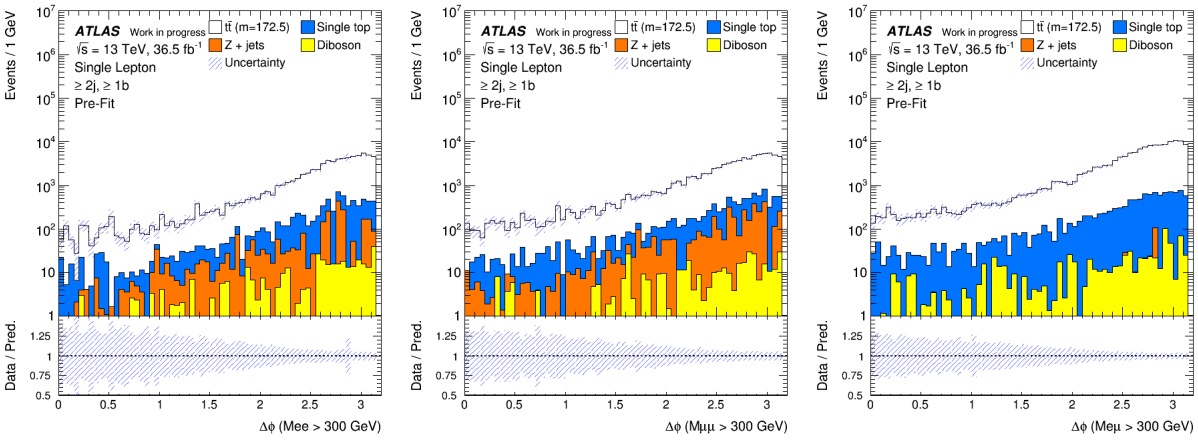

Figure 4: *Angular difference $\Delta\phi$ between the two charged leptons originated from W-boson decay. The events are restricted to the invariant mass of the two charged leptons $M_{\ell\ell} > 300$ GeV. Left: electron-electron final state. Center: muon-muon final state. Right: electron-muon final state.*

extremely useful.

The reconstruction efficiencies are determined using J/Ψ sample. The method employed for the reconstruction efficiencies is called "Tag&Probe" and is based on the selection of an almost pure muon sample from $J/\Psi \to \mu\mu$ events, followed by requiring one leg of the decay (tag) to be identified as a muon that fires the trigger and the second leg (probe) to be reconstructed by a system which is independent of the tag-muon criteria.

This study is performed within the muon working group of the ATLAS collaboration [7].

2.2 Event selection

The reconstructed muons constituting tags and probes satisfy the selections outlined in the following. The tagged muons are accepted if they satisfy $p_T > 4$ GeV and $|\eta| < 2.5$; moreover, these muons must be matched with the triggers. The probe muons are accepted if they satisfy $p_T > 4$ GeV and $|\eta| < 2.5$ and the invariant mass of the tag and probe muons must be within 2.7 GeV $< m(\text{tag}, \text{probe}) <$ 3.5 GeV and with $\Delta R < 0.4$, with ΔR defined as the angular distance between the probe and its nearest jet, i.e. $\Delta R = \sqrt{\Delta\eta^2 + \Delta\phi^2}$.

2.3 Regions under study

Four regions for muons close to jets have been studied: a first region defined by the ratio $p_T^{varcone30}/p_T > 0.06$, where $p_T^{varcone30}$ is defined as the scalar sum of the transverse momenta of the tracks with $p_T > 1$ GeV near the muon in a cone of $\Delta R = 0.3$, and the p_T in the denominator is the transverse momentum of the probe. A second region defined by the ratio $E_T^{topocone20}/p_T > 0.06$, with $E_T^{topocone20}$ is the transverse energy of the tracks near the muon in a cone of $\Delta R = 0.2$; two regions for ΔR, the first for 0 $< \Delta R(\text{jet}, \text{probe}) < 0.2$ and the second for $0.2 < \Delta R(\text{jet}, \text{probe}) < 0.4$.
The data collected in the year 2016, through the pp collision at the ATLAS experiment at a center-of-mass energy of $\sqrt{s} = 13$ TeV, have been used. The total reconstruction efficiency for muons with Medium quality is measured according to Eq. (1):

$$\epsilon(\text{Medium}) = \epsilon(\text{Medium}|\text{CP}) \times \epsilon(\text{ID}|\text{MS}), \tag{1}$$

where the medium muons are those satisfying the medium quality criteria defined in [7] that minimizes the systematic uncertainties associated with muon reconstruction and calibration; CP (Calo Probes) are the Inner Detector (ID) tracks tagged as muons by the calorimeter deposit; MS are the probe muons in the Muon Spectrometers. In the following plots the total reconstruction efficiency is labeled as "CaloTag probe". The resulting values are plotted as distinct measurements in each η bin with p_T increasing from 5 to 15 GeV going from left to right.
The plot in Fig. 5 shows the reconstruction efficiency of the $p_T^{varcone30}/p_T > 0.06$ selection. There is good agreement between data efficiency and the simulation efficiency, except in the central bin (-0.1 $< \eta <$ 0.1) of the crack region. In the ratio data/MC, the blue is the statistical error and yellow is the quadratic sum of statistical and systematic errors.
Figure 6 shows the reconstruction efficiency of the $E_T^{topocone20}/p_T > 0.06$ selection. There is good agreement between data efficiency and the simulation efficiency, except in the central bin ($-0.1 < \eta < 0.1$) of the crack region. In the data/MC ratio, the statistical error is displayed in blue and the quadratic sum of statistical and systematic errors in yellow.
Figure 7 shows the reconstruction efficiency in the two region of ΔR: on the left the region 0 $< \Delta R(\text{jet}, \text{probe}) < 0.2$ is presented, on the right the region $0.2 < \Delta R(\text{jet}, \text{probe}) < 0.4$. The large error bars are due to the fact that the data and MC samples do not have enough probes close to jets. In the data/MC ratio, the statistical error is blue and the quadratic sum of statistical and systematic errors is yellow.

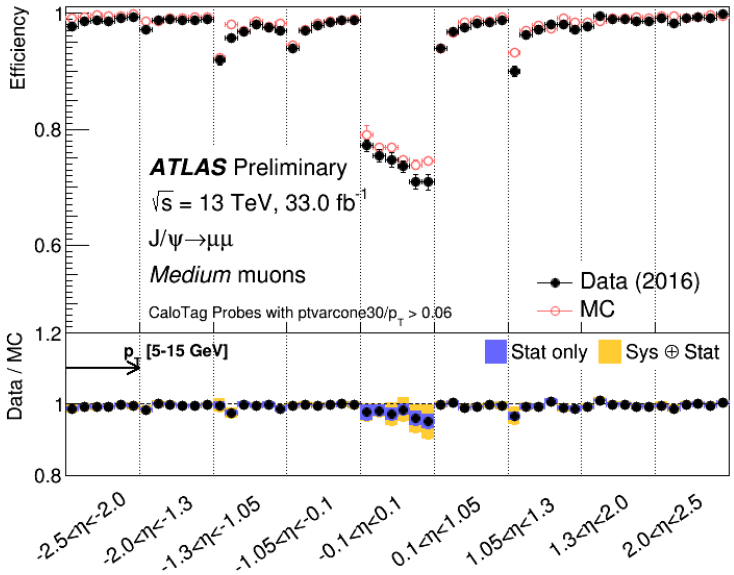

Figure 5: *Upper panel: total reconstruction efficiency of muons close to jets in the region* $p_T^{varcone30}/p_T > 0.06$*, black full dots are data 2016 and red empty dots are Monte Carlo. Lower panel: data/MC ratio; blue is the statistic error and yellow is the quadratic sum of statistic and systematic errors.*

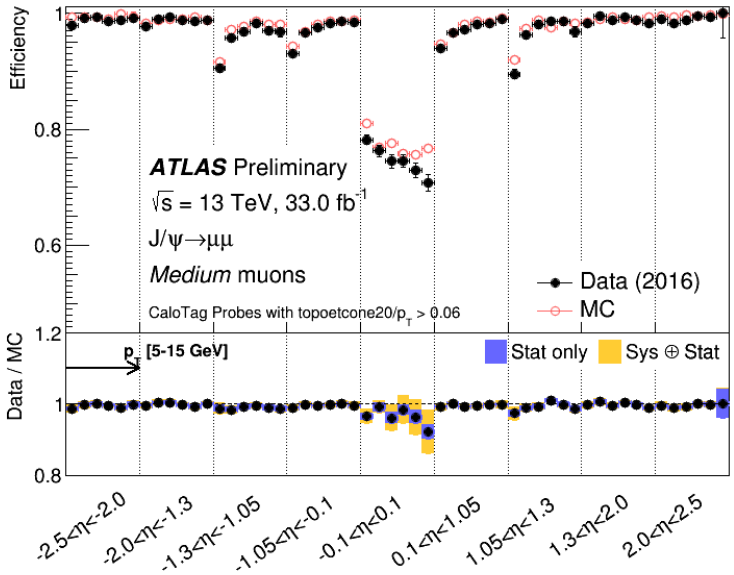

Figure 6: *Upper panel: total reconstruction efficiency of muons close to jets in the region* $E_T^{topocone20}/p_T > 0.06$*, black full dots are 2016 data and red empty dots are Monte Carlo simulations. Lower panel: data/MC ratio; blue is the statistic error and yellow is the quadratic sum of statistic and systematic errors.*

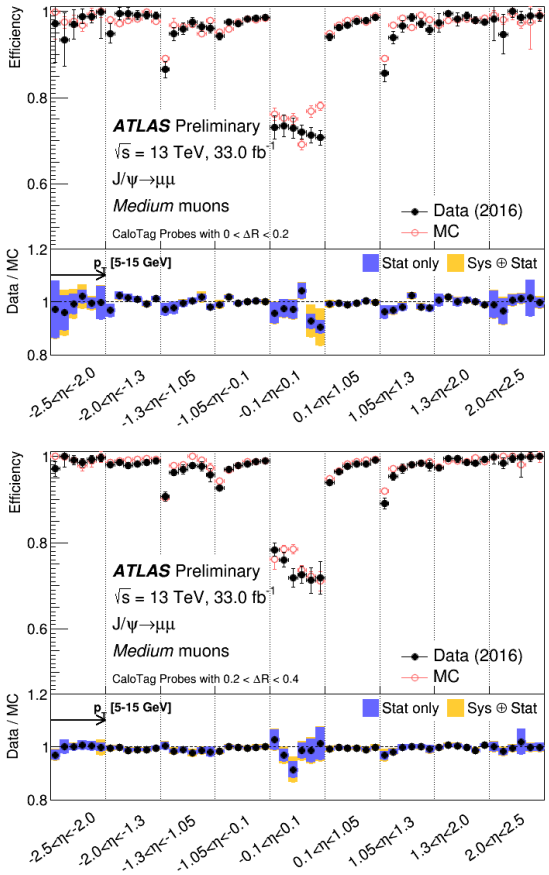

Figure 7: *Upper panel in the top figure: total reconstruction efficiency of muons close to jets in the region* $0 < \Delta R(jet,probe) < 0.2$. *Upper panel in the bottom figure: total reconstruction efficiency of muons close to jets in the region* $0.2 < \Delta R(jet,probe) < 0.4$. *Black full dots are 2016 data and red empty dots are Monte Carlo simulations. Lower panels: data/MC ratio; blue is the statistic error and yellow is the quadratic sum of statistic and systematic errors.*

3 Summary

We are preparing the analysis of $t\bar{t}$ resonance in dilepton channel to search for new phenomena Beyond Standard Model; moreover, the first reconstruction efficiency for muons close to jets in the ATLAS detector has been studied.

4 Acknowledgements

I would like to thank Prof. Lucio Cerrito for the opportunity to work in the NPTEV-TQP2020 group. A heartfelt thanks to Dr. Marco Vanadia and Dr. Michele Pinamonti for helping me in the analysis. Finally, I would like to thank all ATLAS group.

References

1. C. Patrignani et al., *Review of Particle Physics*, Chin. Phys. C40 (2016) 100001.

2. M. Cacciari, G. P. Salam and G. Soyez, *The anti-k_t jet clustering algorithm*, JHEP 04 (2008) 063, arXiv:0802.1189 [hep-ph].

3. ATLAS Collaboration, *Tagging and suppression of pileup jets with the ATLAS detector*, ATLAS-CONF-2014-018, 2014, url:https://cds.cern.ch/record/1700870 .

4. S. Frixione, P. Nason and C. Oleari, *Matching NLO QCD computations with Parton Shower simulations: the POWHEG method*, JHEP 0711 (2007) 070, arXiv: 0709.2092 [hep-ph].

5. T. Sjostrand, S. Mrenna and P.Z. Skands, *A brief introduction to PYTHIA 8.1*, Comput. Phys. Commun. 178 (2008) 852, arXiv: 0710.3820 [hep-ph].

6. S. Höche, F. Krauss, M. Schönherr and F. Siegert, *QCD matrix elements + parton showers: the NLO case*, JHEP 04 (2013) 027, arXiv: 1207.5030 [hep-ph].

7. ATLAS Collaboration, *Muon reconstruction performance of the ATLAS detector in proton-proton collision data at $\sqrt{s} = 13$ TeV*, Eur. Phys. J. C76 (2016) 292, arXiv:1603.05598 [hep-ex].

Frascati Physics Series Vol. 67 (2018)
6th Young Researcher Workshop 'Physics Challenges in the LHC Era'
May 7 and 10, 2018

THE MU2E EXPERIMENT AT FERMILAB: R&D, DESIGN AND STATUS

Eleonora Diociaiuti
LNF-INFN & Tor Vergata University
On behalf of the Mu2e collaboration

Abstract

The Mu2e Experiment at Fermilab [1] will search for coherent, neutrinoless conversion of negative muons into electrons in the field of an aluminum nucleus, $\mu^- + N(A,Z) \rightarrow e^- + N(A,Z)$. This is an example of Charged Lepton Flavour Violation (CLFV) never observed experimentally.
The dynamics of such a process is well modelled by a two-body decay, resulting in a mono-energetic electron with an energy slightly below the muon rest mass (∼104.967 MeV).
If no events are observed in three years of running, Mu2e will set an upper limit on the ratio between conversion and capture rate $R_{\mu e} \leq 6 \times 10^{-17}$ (@ 90% C.L.). This will improve the current limit of a factor of 10^4 over previous experiments.
The experiment complements and extends the current/planned searches ($\mu \rightarrow e\gamma$ decay at MEG , mu3e) as well as the direct searches for new physics at the LHC. Indeed, such CLFV searches in the muon sector probe new physics at a mass scale inaccessible with direct searches at either present or planned high-energy colliders.
To detect the muon conversion process, a very intense pulsed beam of negative muons is produced by means of a S-shape Superconducting Solenoid Magnet System that is organized into three sub-systems: the Production Solenoid, the Transport Solenoid and the Detector Solenoid. The beam is stopped at 10 GHz on an Aluminum target inside the Detector Solenoid.
The Mu2e detectors, also installed inside the Detector Solenoid, are a high-precision tracker made on ∼ 20000 straw tubes, and a calorimeter composed of ∼ 1500 pure CsI crystals organized in two disks and readout by two large area UV-extended Silicon Photomultipliers (SiPMs). The Detector Solenoid region is surrounded by a Cosmic Ray Veto based on scintillators readout by SiPMs.

1 Charged Lepton Flavor Violation and muon to electron conversion

Within the Standard Model (SM), transitions in the lepton sector between charged and neutral particles preserve flavor, since the neutrinos are considered massless. Even considering the discovery of neutrino oscillations, in the minimal extension of SM, the predicted branching ratios of Charged Lepton Flavor Violation (CLFV) processes in the muon sector are smaller than 10^{-50}, unreachable by the current particle accelerators.

Any experimental observation of CLFV processes would be a clear signature of New Physics (NP). The coherent muon conversion in the electric field of a nucleus, $\mu N \rightarrow eN$, is an example process that can probe CLFV. This process has a very clear experimental signature: a monoenergetic electron with energy slightly below the muon rest mass ($\sim$ 104.96 MeV).

The Mu2e experiment [2)] is designed to improve by 4 orders of magnitude the current limit on the conversion rate, $R_{\mu e}$, set by the SINDRUM II experiment [3)]. The $R_{\mu e}$ rate is defined as the ratio between the number of electrons from the conversion process and the number of captured muons:

$$R_{\mu e} = \frac{\mu^- N(Z,A) \rightarrow e^- N(Z,A)}{\mu^- N(Z,A) \rightarrow \nu_\mu N(Z-1,A)} < 6 \times 10^{-17} \text{ (at 90\% C.L.)}, \quad (1)$$

where, in the Mu2e case, N(Z,A) is an aluminum nucleus.

Many NP scenarios, like SUSY, Leptoquarks, Heavy Neutrinos, GUT, Extra Dimensions or Little Higgs, predict significantly enhanced values for $R_{\mu e}$, at a level accessible by the Mu2e sensitivity [4)].

A model-independent description of the CLFV transitions, for NP models, is provided by an effective Lagrangian [5)] where the different processes are divided in dipole amplitudes and contact-term operators. While the $\mu \rightarrow e\gamma$ decay is mainly sensitive to the dipole amplitude, $\mu \rightarrow e$ conversion and $\mu \rightarrow 3e$ receive contributions also from the contact interactions. It is possible to parametrise the interpolation between the two amplitudes by means of two parameters [5)]: Λ, which sets the mass scale, and κ, which governs the ratio of the four-fermion to the dipole amplitude. For $\kappa \ll 1 (\gg 1)$ the dipole-type (contact) operator dominates. Figure 1 summarises the power of different searches to explore this parameter space [6)].

Present experimental limits already excluded the energy scale up to $\Lambda < 700$ TeV, setting serious constraints on SM extensions. The interpretation of a eventual direct observation of NP at LHC will have to take into account precise measurements (or constraints) from MEG [7)] and Mu2e: the comparison between these determinations will help pin down the underlying theory.

2 The Mu2e experimental apparatus

The Mu2e apparatus consists of three superconductive solenoid magnets, as shown in Figure 2.

In the Production Solenoid (PS) a 8 GeV proton beam provided by the Fermilab accelerator enters the PS and hits a tungsten target producing mostly pions. The gradient field in the PS increases from 2.5 to 4.6 T in the same direction of the incoming beam and opposite to the outgoing muon beam direction. This gradient field works as a magnetic lens to focus charged particles into the transport channel. The focused beam is constituted by muons, pions and a small number of protons and antiprotons. When the beam passes through the S-shaped Transport Solenoid (TS), low momentum negative charged particles are selected and delivered to the aluminum stopping target foils in the Detector Solenoid (DS). Electrons from the μ-conversion (CE) in the stopping target are captured by the magnetic field in the DS and transported through the Straw Tube Tracker, which reconstructs the CE trajectory and its momentum. The CE then impinges the Electromagnetic Calorimeter, which provides independent measurements of energy, impact time and position. Both detectors operate in a 10^{-4} Torr vacuum and in an uniform 1 T

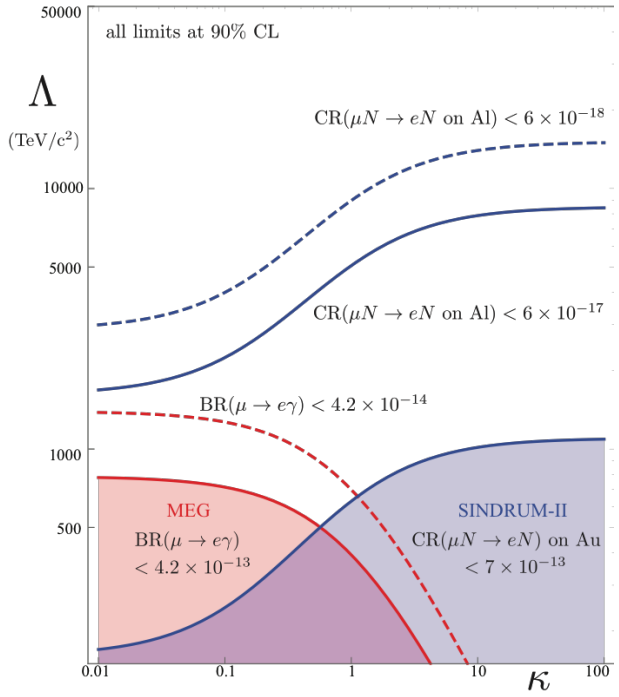

Figure 1: *Sensitivity of $\mu \to e\gamma$, $\mu \to e$ transition and $\mu \to 3e$ to the scale of new physics Λ as a function of the parameter κ . The shaded areas are excluded by the present limits.*

axial field.
A Cosmic Ray Veto (CRV) system covers the entire DS and half of the TS.
The measurement of the total number of captured muons is provided by a high purity germanium detector, via the observation of the x-rays resulting from the nuclear capture.
To reach the sensitivity goal $R_{\mu e} < 8.4 \times 10^{-17}$ at 90% C.L., about 10^{20} protons on target are needed; this corresponds to about 10^{18} stopped muons are needed. Moreover a pulsed beam structure is needed to suppress the prompt background coming from the proton interactions; Fermilab accelerator complex provides a sequence of 200 ns wide micro-bunches separated by 1.7 μs. The beam period is roughly twice the muon mean lifetime in Al nucleus, $\tau_{Al} = 864$ ns. This particular beam structure, as shown in Figure 3, allows Mu2e to use a delayed selection windows.

3 Mu2e Detectors

3.1 Tracker

The Mu2e tracker will measure the electron trajectory in order to calculate their momentum. The main aims of Mu2e tracker are: i) minimize multiple Coulomb scattering and energy loss to obtain a good momentum resolution, ii) provide sufficient numbers of hits to find and fit tracks with high efficiency, iii) have segmentation and/or multi-hit capability to operate at the expected rates, iv) provide redundancy to protect against mis-reconstructions and non-Gaussian tails.
The tracker total length is ∼3 m and its diameter is 1.6 m; its active area's radius extends from 40 to 70 cm, so that, as shown in Figure 4, particles with a very low momentum do not reach at all the active

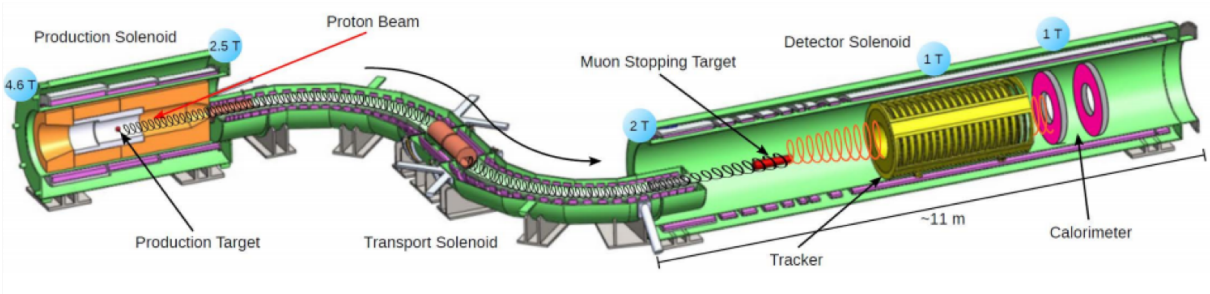

Figure 2: *Layout of the Mu2e experiment.*

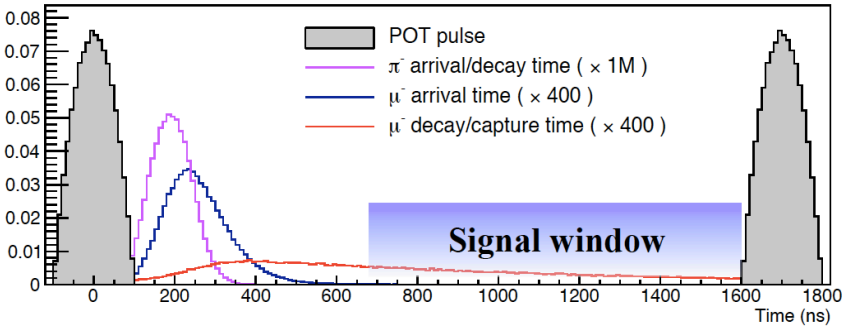

Figure 3: *The Mu2e spill cycle for the proton on target pulse (POT) and the delayed selection window that allows an effective elimination of the background from RPC*

area or just leave leave too few hits for a track to be reconstructed. The detector is made of 20736 drift

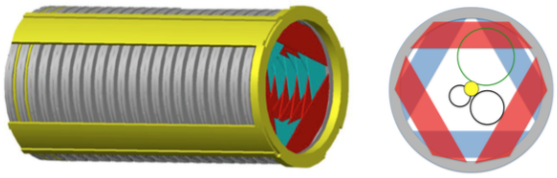

Figure 4: *Left: longitudinal view of the Mu2e tracker. Right: Cross view of Mu2e tracker with trajectories of a 105 MeV/c momentum conversion electron (green circle), 53 MeV/c Michel electron (bottom right circle) and electron with energy small than 53 MeV (bottom left circle).*

straw tubes placed transverse to the axis of the DS. Current choice for drift gas is 80:20 Argon: CO_2 . Groups of 96 straws are assembled into panels, 6 panels (three per side rotated by 120°) are assembled into planes. A pair of planes made a station, each station is separated by 46 mm. This two planes are identical but the second plane is rotated of 180° around the vertical axis with respect to the first plane. The Mu2e experiment is composed of 18 stations.

3.2 Calorimeter

The Mu2e calorimeter [8] must operate in a high-rate, high-radiation environment. This motivates a fast response, an excellent time resolution and good radiation hardness requirements. The Mu2e calorimeter has to: i)provide the means to implement an independent trigger based on the sum and pattern of energy deposition; ii) provide a "seed" to improve tracker pattern recognition and reconstruction efficiency; iii) provide shower shape, energy, and timing information that, in combination with information from the tracker, can distinguish electrons from muons and pions; iv)have large acceptance for signal electrons within the acceptance of the tracker. After a long R&D phase, the best compromise between costs and properties has been selected: the calorimeter design consists in 1346 undoped CsI crystals located downstream of the tracker, arranged in two disks and positioned at a distance of half wavelenght of a typical conversion electron (Figure 5).

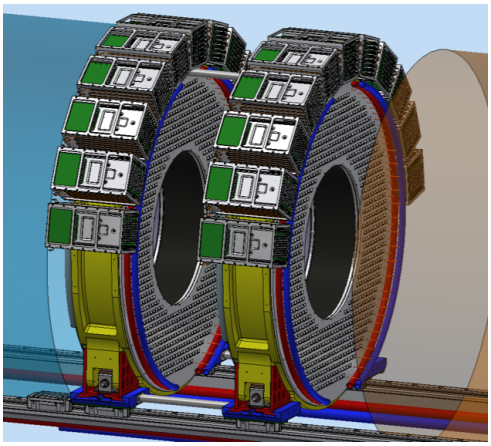

Figure 5: *CAD model of the Mu2e electromagnetic calorimeter.*

The crystals have squared faces with dimensions of (34×34) mm^2 and are 200 mm long. Each crystal is read by two 2×3 array of individual 6×6 mm ^{2} UV-extended Silicon Photomultipliers (SiPMs). The solid-state photodetectors are necessary due to the presence of the high magnetic field. FEE, HV, slow controls and digitizer electronics are mounted behind each disk and must then work adequately in a high vacuum (to reduce multiple scattering), high magnetic field and high radiation environment.
Equalization of the crystal response will be provided through a circulating radioactive source (FluorinertTM, C8F18), already experimented by the BaBar EMC [9] while a laser flasher system will be used for relative calibration and gain monitoring. Usage of cosmic ray events for the calibration along running is also planned.

3.3 Cosmic Ray Veto (CRV)

Cosmic muons are one of the major sources of background for the Mu2e experiment: they can produce 105 MeV electrons through interaction with the apparatus or with a decay-in-flight.

The CRV system provides both a passive shielding (thick layer of concrete surrounding the DS) and an active veto, with a system of four layers of long scintillator strips, with an aluminum layer between them, covering all the DS and the last part of the TS (Figure 6). The strips are 2 cm thick, providing ample light yield to allow a low enough light threshold to be set to suppress most of the backgrounds.

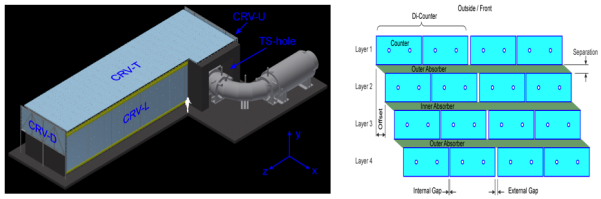

Figure 6: *Left: 3D view of the of the cosmic ray veto. Right: detail of a single CRV module with 4 scintillator strips.*

Category	Background process	Estimated Yield (events)
Intrinsic	Decay in orbir (DIO)	0.199 ± 0.092
	Muon Capture (RMC)	0.000 ± 0.004
Late Arriving	Pion Capture (RPC)	0.023 ± 0.006
	Muon decay in flight	< 0.003
	Pion decay in flight	0.001 ± 0.001
	Beam electrons	0.003 ± 0.001
Miscellaneous	Antiproton induced	0.047 ± 0.024
	Cosmic rays	0.092 ± 0.020
	Total	0.37 ± 0.10

Table 1: *Expected background list as evaluated by full simulation.*

Aluminum absorbers between the layers are designed to suppress punch through from electrons. The scintillation light is then captured by optical fibers and then read out by means of SiPMs.

4 Expected background

When negative muons stop in the aluminum target, they are captured in an atomic excited state. The resultant muonic atoms persist with a lifetime of 864 ns, decaying in orbit (DIO) 39% of the time while capturing on the nucleus the other 61% of the time. Low-energy photons, neutrons and protons are emitted in the nuclear capture process and constitute an environmental background that produces an ionization dose and a neutron fluency on the detection systems as well as an accidental occupancy for the reconstruction program. The kinematic limit for the muon decay in vacuum is at about 54 MeV, but the nucleus recoil generates a long tail that has the endpoint exactly at the conversion electron energy. For this reason, DIO electrons are an irreducible background that have to be distinguished by the mono-energetic CE. The finite tracking resolution and the positive reconstruction tail has a large effect on the falling spectrum of the DIO background that translates in a residual contamination in the signal region. Estimates of other backgrounds are presented in Table 1 for a total background contribution of 0.37 events.

5 Conversion Electron reconstruction

At the CE energy the momentum resolution is dominated by fluctuations in the energy loss in the target, multiple scattering and bremsstrahlung in the tracker. By performing a full simulation of the tracker, a pattern recognition and a Kalman fitter for the tracking we obtain: a CE reconstruction efficiency of 9 % for good quality tracks and at least 25 hits/track. The resolution is well parametrised by a Crystal Ball

function with a negative bremsstahlung tail, a Gaussian core of 116 keV and a long exponential positive resolution tail.

Figure 7 shows the signal and background distributions as seen by a full simulation of the experiment (pileup included) in the following conditions: (i) 3.6×10^{20} proton on target, (ii) 6×10^{17} stopped muons and (iii) a $R_{\mu e}$ of 10^{-16}. After maximising signal over background, the best selection corresponds to counting events in a momentum window between 103.75 and 105 MeV/c. A DIO contribution of 0.199 events is estimated and 3.5 candidates are observed. This counting corresponds to setting a limit on $R_{\mu e}$ below $6\times\ 10^{-17}$ at 90 % C.L., in good agreement with the experimental goal.

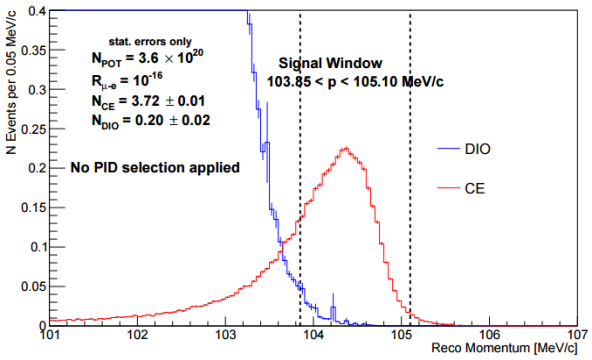

Figure 7: *Full simulation of DIO and CE events for an assumed $R_{\mu e}$ of 10^{-16}.*

References

1. Mu2e Collaboration, http://mu2e.fnal.gov/collaboration.shtml
2. L. Bartoszek, et al., Mu2e Technical Design Report [arXiv:1501.05241]
3. W. Bertl et al; A search for $\mu - e$ conversion in muonic gold, The European Physical Journal C - Particles and Fields 47(2)2006 337-346
4. Marciano, Mori, and Roney, Flavour physics of leptons and dipole moments, Ann. Rev. Nucl. Sci. 58 ;doi:58.110707.171126 2008 [arXiv:0801.1826]
5. A. De Gouvea et al. Lepton Flavor and Number Conservation, and Physics Beyond the Standard Model; Prog. Part. Nucl. Phys 71,75-92 doi:10.1016/j.ppnp.2013.03.006, 2013 [arXiv:1303.4097]
6. R. Bernstein and P. Cooper, Charged Lepton Flavor Violation: An Experimenter's Guide, FERMILAB-PUB-13-259-PPD,doi:10.1016/j.physrep.2013.07.002 2013[arXiv:1307.5787]
7. A.M. Baldini et al; Search for the lepton flavour violating decay $\mu^+ \rightarrow e^+\gamma$ with the full dataset of the MEG experiment. The European Physical Journal C, 2016, Volume 76, Number 8, Page 1
8. N. Atanov et al; The Mu2e undoped CsI crystal calorimeter; JINST 13 (2018) C02037 [arXiv:1801.02237]
9. J.M. Bauer; The BaBar Electromagnetic Calorimeter: Status and Performance Improvements; IEEENucl.Sci.Symp.Conf.Rec.2:1038-1042, 2006 [arXiv:physics/0601138]

Frascati Physics Series Vol. 67 (2018)
6th Young Researcher Workshop 'Physics Challenges in the LHC Era'
May 7 and 10, 2018

DESIGN AND STATUS OF THE Mu2e CRYSTAL CALORIMETER

Raffaella Donghia
Roma Tre University and INFN - National Laboratory of Frascati
On behalf of the Mu2e calorimeter group

Abstract

The Mu2e experiment at Fermilab will search for the charged-lepton flavour violating neutrino-less conversion of a negative muon into an electron in the field of an aluminum nucleus. The calorimeter plays an important role in providing a fast trigger filter, excellent particle identification and a seeding for track reconstruction. Its requirements are to provide an energy (timing) resolution better than 10% (0.5 ns) and a position resolution below 1 cm, for 100 MeV electrons. The calorimeter consists of two disks, each one made of 674 un-doped CsI crystals readout by two large area arrays of 2×3 UV-extended SiPMs of 6×6 mm^2 dimensions. A large scale prototype (Module-0) has been constructed and tested with an electron beam in the energy range between 60 and 120 MeV at the BTF of Frascati National Laboratories. Results demonstrated that this calorimeter satisfies the Mu2e requirements.

1 Introduction

The Mu2e experiment [1) 2)] at Fermilab will search for the muon conversion to an electron in the field of an Aluminum nucleus, improving by 4 orders of magnitude the world best sensitivity on this Charged Lepton Flavor Violating process. The experiment consists of three superconducting solenoids magnets containing the production and the stopping target, the tracker and the electromagnetic calorimeter and an external system used to veto cosmic rays (Fig. 1, left).

The Mu2e calorimeter is designed to achieve an energy resolution better than 10% and a time resolution below 0.5 ns, for the 104.97 MeV electrons coming from the muon-to-electron conversion process (CEs), in order to help the tracker in the identification of CEs, in building an efficient trigger and in improving the track reconstruction efficiency.

The baseline calorimeter design consists of two disks of 674 un-doped CsI crystals readout by two large area UV-extended Silicon Photomultipliers (SiPMs) (Fig. 1, right) [3)]. The Front End Electronics

(FEE) amplification and HV regulator chips are connected to the SiPM pins while the digitization of the signals are carried out by custom boards located in nearby crates. A radioactive source system [4] and a laser system allow to set the energy scale and monitor the fast changes of response and resolution. Several tests have been performed on single components and on a large scale calorimeter prototype (Module-0) to confirm that the chosen design satisfies the Mu2e requirements. In the following, the qualification tests carried out during the pre-production phase to select the vendors of crystals and sensors are summarised and the realisation and test of Module-0 calorimeter prototype is also discussed. At the moment of writing, the production of components has also started. A summary of the methods and results obtained so far for the production is also reported.

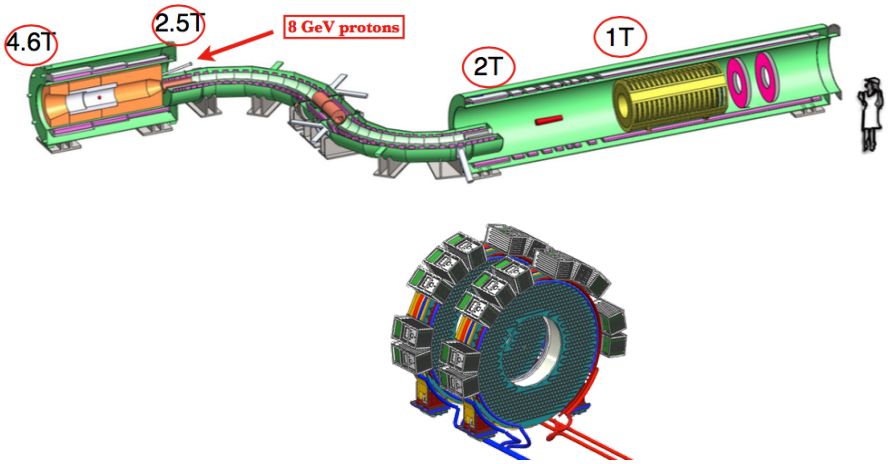

Figure 1: *Top: Layout of the Mu2e experiment at Fermilab. Bottom: Engineering drawing of Mu2e crystal calorimeter disks.*

2 Pre-production of CsI crystals and Mu2e SiPMs

During 2016, we received 72 square crystals of $34 \times 34 \times 200$ mm^3 dimensions from three different vendors: Saint Gobain, Siccas, Amcrys. A dedicated Quality Assurance process was carried out to evaluate the crystals characteristics. The scintillation properties were evaluated with a ^{22}Na source, which emits back-to-back 511 keV photons, by coupling the crystals in air to a UV-extended PMT [7]. The light yield (LY) exceeded the specifications of LY>100 photoelectrons/MeV. The Longitudinal Response Uniformity (LRU), defined as the RMS of the LY measured in 8 different positions along the crystal axis, was required to be smaller than 5%. All the crystals satisfied this requirement, except four Siccas and one St. Gobain crystals. The energy resolution at 511 keV was on average 14.5%, well within the 19% requirement. Finally, the ratio (F/T) between the response to the fast (F) light emission component (at $\sim$ 315 nm wavelength) over the total (T) light had to be better than 75%. Most of the crystals satisfied this specification apart some of the Amcrys crystals. All crystals demonstrated a good radiation hardness up to a dose of 100 krad. St.Gobain and Siccas were chosen as vendors for the crystals production.

A Mu2e-SiPM is defined as the parallel of two series of three UV-extended SiPMs of 6×6 mm^2 dimensions for a total active area of 12×18 mm^2. The readout series configuration has been chosen to reduce the overall capacitance and narrow the shape of signals. In 2016, we procured 150 custom Mu2e-

SiPMs from Hamamatsu, SensL and AdvanSiD companies. All these pre-production sensors have been characterized at an automatized station built to measure the operational voltage, the photon detection efficiency and the gain of all cells, as well as the RMS spreads of each array [8]. The measured parameters were well within the required technical specifications (G $>10^6$, PDE $> 20\%$, $\mathrm{RMS}_{Vop} < 0.5\%$). Moreover, mean time to failure (MTTF) and radiation hardness tests were performed. The Mu2e SiPMs reached an MTTF larger than 6×10^5 hours for all vendors. SiPM prototypes were not damaged when exposed to a ionization dose up to 18 krad.

As neutron hardness test, a SiPM for each vendor was exposed to a total flux of up to 8.5×10^{12} n/cm^2 at 1 MeV equivalent energy. The Hamamatsu SiPM maintained a dark current lower than 20 mA and better than a factor of two with respect to the other sensors. For this reason, Hamamatsu was selected as the vendor for the production phase [9].

3 Realization and test of the Module-0 prototype

A large scale prototype, called Module-0 (Fig. 2), has been built using 51 crystals and 102 Mu2e SiPMs produced and qualified during the pre-production phase. Module-0 was built trying to resemble as much as possible the final disk. The back disk was done by Zedex insulator instead of PEEK but the cooling lines connecting the SiPM and FEE holders were realized with the final technique, thickness and shape. For the electron beam test, carried out in May 2017 at the LNF Beam Test Facility, the detector was thermally stabilized at room temperature. In a later test, it was operated under vacuum to measure the outgassing rates and then cooled to low temperature inside a large vacuum chamber.

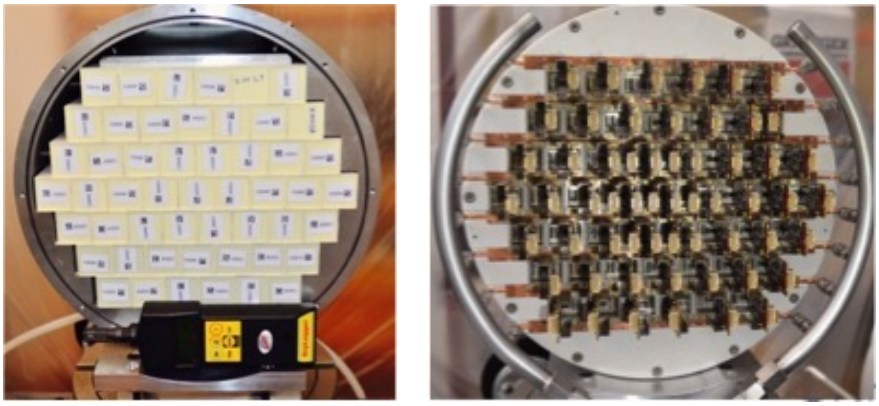

Figure 2: *Pictures of the Module-0 during assembly: frontal view with crystals (left) and back view with SiPM and FEE chips (right).*

The SiPM signals were amplified with a first prototype of the FEE chips. On the same chip, a local HV regulator allowed to set and read back the bias voltages. A NIM prototype of the Mezzanine board allowed to perform the slow control in groups of 16 channels. Since the Mu2e custom digitizer (DIRAC) was not ready yet for the electron beam test, data were sampled and acquired by means of two 32-channels V1742 CAEN boards at 1 GHz sampling rate. Due to the limited number of available channels in the DAQ system, only the central crystal and the first surrounding ring were equipped and readout with two sensors and two FEE chips per crystal. For the outer crystals, one of the sensors was left without FEE and unbiased. In total 58 SiPMs were readout. The remaining 6 digitizer channels were

used to collect trigger and scintillating counters' signals.

Similarly to the calorimeter disks, Module-0 is a structure of staggered crystals with a size large enough to contain most of the electromagnetic shower for an 105 MeV electron beam. Energy and time measurements were obtained using an electron beam in the energy range between 60 and 120 MeV, impinging at 0 and at 50 degrees on the calorimeter surface. Two finger plastic scintillating counters ($5 \times 1 \times 2$ cm^3), crossed at 90 degrees, were positioned on the beam axis, at few centimetres from the front face of Module-0. These beam counters provided a trigger for electrons and allowed to select single particle events. To select cosmic rays, a large plastic scintillator ($50 \times 50 \times 200$ mm^3), was placed above the calorimeter. All scintillators were read out by photomultipliers. A calibration laser system was installed to monitor the response of the central crystal during the running time. The temperature was kept stable at 20 °C by using an external chiller connected to the Module-0 cooling pipes and monitored by the temperature sensors present on each FEE chip.

We have acquired data for one week by triggering with the OR logic of different trigger signals. The beam trigger (BT) was produced by the coincidence of the discriminated signals of the two beam counters. A trigger (BTF) provided by the BTF system allowed to take beam events, without relying on our beam counters. A cosmic ray trigger (CRT) generated by the discriminated signals of the scintillation counter was used to collect cosmic-ray events for calibration purposes. A sinchronization signal from the Laser system (LT) allowed to acquire the laser pulses for monitoring purposes.

3.1 Energy resolution

The charge was estimated by numerical integration of the collected waveforms in a 200 ns wide time window. A single-particle selection cut has been applied during the analysis. To equalize the response of each channel of the Module-0 two calibration strategies were followed:

- Equalization based on the beam energy deposit of a 100 MeV beam centered at the center of the crystal under calibration. This was carried out only for the two innermost rings for a total of 26 channels. Statistical error of each calibration was around 0.48 %.
- Equalization based on the energy deposition from Minimum Ionizing Particles (MIP) selected from the CRT trigger. This was done for all calorimeter channels. Statistical error of each calibration was around 0.45 %.

The two calibration techniques were compared for the 26 common channels. The ratio of these calibration constants with respect to the central channel are well centered at 1 with an RMS of 3% providing an upper limit for the systematic error of such procedure. The peak values were obtained through a Log-Normal fit to the charge reconstructed in a single crystal.

For the final equalization, we have applied the calibration factors obtained with the CRT sample. The energy scale has been set, after the equalization, by comparing the reconstructed charge in the whole matrix (Qrec) with the expected energy deposited in the Module-0, as evaluated by a Geant4 based Montecarlo simulation. A good linearity in response is obtained. The energy scale factor resulted to be $E_{sc} = (12.07 \pm 0.11)$ pC/MeV and was then applied to all reconstructed charges to obtain the calibrate energy $\mathrm{E} = \mathrm{Q_{rec}} \times \mathrm{E_{sc}}$. In Figure 3 (top), the distribution of E for 100 MeV electron beam entering at 0° in the Module-0 is shown. Monte Carlo simulation (red line) is in well agreement with data. A similar distribution for the 100 MeV electrons impinging at 50° is shown in the bottom plot.

The energy resolution (σ_E/E) is evaluated as the ratio between the sigma of a Log-Normal fit applied to the energy distribution (σ_E) and the energy peak value (E). An energy resolution of $\sim 5.4\%$ (7.5%)

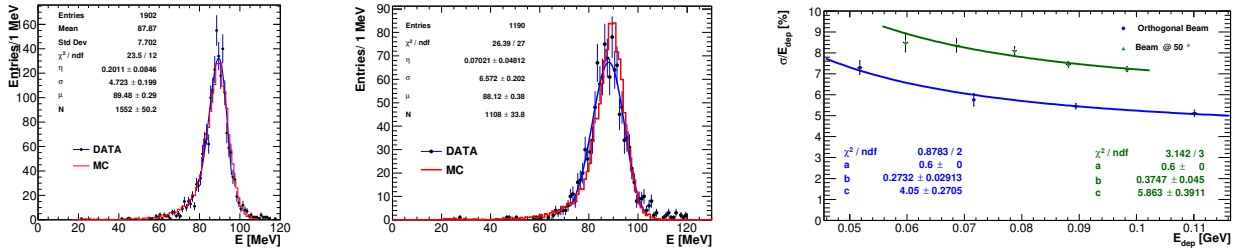

Figure 3: *Data - MC comparison of the energy deposited in the entire matrix when a 100 MeV electron beam strikes at an incidence angle of 0° (left), 50° (middle) on the Module-0 surface. Energy resolution as a function of the deposited energy in Module-0 (right). Black dots: 0 degrees; red dots: 50 degrees.*

is obtained at 100 MeV for 0 (50) degrees, in good agreement with the Mu2e requirements. The energy resolution at different beam energies is reported in Figure 3. The dependence of the energy resolution as a function of the deposited energy E_{dep} for single particle events has been parametrized by the function:

$$\frac{\sigma_E}{E_{dep}} = \frac{a}{\sqrt{E_{dep}[GeV]}} \oplus \frac{b}{E[GeV]} \oplus c \tag{1}$$

where a represents the stochastic term, b the noise term and c the constant term. The operator $\oplus$ means quadratic sum. The fit is rather insensitive to the stochastic term that is almost negligible and it has been fixed to 0.6% has estimated by the light yield contribution of 40 pe/MeV. The deterioration of resolution at increasing incidence angles is dominated by the increasing fluctuation of the leakage term.

3.2 Timing Resolution

After applying the same selection criteria explained above, the signal time is determined by fitting the leading edge of the waveform with an analytic function. The best accuracy was achieved by setting the signal time at a constant fraction (CF) of the pulse height. For the time evaluation, three free components have to be fixed: i) the waveforms fit function; ii) the fit range and iii) the best CF value. After a study of several different functions, the best result was obtained using an asymmetric log-normal function [10]. The optimisation of the resolution was then performed by varying the fit range and the constant fraction threshold over a grid and by choosing the best configuration. Figure 4 (left) shows an example of a Hamamatsu SiPM waveform fit by a log-normal function in the optimized region.

The time difference (ΔT) of the two Hamamatsu SiPMs, reading out the central crystal of Module-0, is shown in Figure 4 (right) for 100 MeV electron beam at 0°. The red line represents the gaussian fit and the time resolution for a single sensor is evaluated as $\sigma(\Delta T)/\sqrt{2}$. A single sensor resolution of $\sim$ 132 ps is obtained. Since in the Mu2e experiment the sampling frequency of the digitizer boards will be 200 MHz, the waveforms were offline re-sampled in 5 ns bins. A time resolution deterioration smaller than 30 % is obtained, which is negligible with respect to the Mu2e calorimeter requirements. Figure 4 (right) shows the time resolution as a function of the highest crystal energy at different beam energies and for cosmic rays. Both Hamamatsu and SensL SiPMs results are reported. The dependance of the single sensor time resolution σ_T from the deposited energy E_{dep} for single particle events was parametrized by the function [11]:

$$\sigma_T = \frac{a}{E[GeV]} \oplus b \tag{2}$$

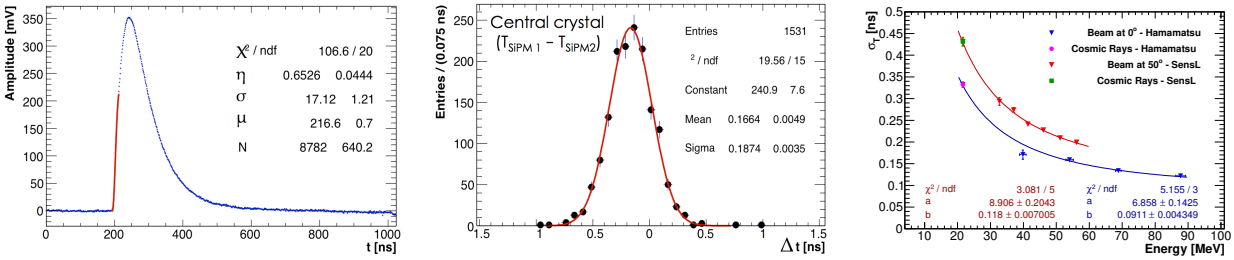

Figure 4: *Left: Example of a Hamamatsu SiPM waveform for a beam energy of 100 MeV and sampled at 1 GHz. The red line represents the log-normal fit used to extrapolate the signal time. Middle: Time difference between the two Hamamatsu SiPMs reading out the central crystal, when a 100 MeV beam enters perpendicularly. Right: Time resolution as a function of the deposited energy in the most energetic crystal.*

where a is proportional to the emission time constant of the undoped CsI and b represents the additional contribute due to the readout electronics.

4 Production phase

The calorimeter crystals and SiPMs production phase in now ongoing and the readout electronic design is almost concluded.

Crystals, produced by Saint Gobain and SICCAS, are delivered to Fermilab where their dimensions, light yield and light response uniformity and radiation induced noise are measured, checking the same above mentioned requirements and using automitised test station developed at LNF-INFN. Of the ∼150 crystals tested so far, some have been rejected because of the mechanical tolerance, while all the other checks have been successful passed. An on going revision of vendor procedures is expected to improve the production yield. Radiation hardness is checked at Caltech on a random subsample of each production batch.

Also SiPM characteristics are tested at Fermilab. Automatised test station developed at LNF-INFN and Pisa-INFN are used to check the array uniformity and the gain × PDE of each cell: 25 arrays can be tested at the same time; 5 of them have never changed and are used as reference; dark current versus bias voltage and gain at the operating voltage are measured at 3 different temperatures: −10 °C, 0 °C, 200 °C. An accelerated aging test at 65 °C is performed on 15 arrays per batch to ensure the required Mean Time to Failure. Radiation hardness to neutrons is checked on 5 arrays per batch at the Helmholtz Zentrum Dresden Rossendorf (Germany). Of the ∼ 1500 Hamamatsu production SiPM tested so far only 4% have been rejected because of dark current non-uniformity between the 6 cells.

5 Conclusion

The Mu2e calorimeter is a state of the art crystal calorimeter with excellent energy ($<$ 10%) and timing ($<$ 500 ps) resolutions, for 100 MeV electrons, and a good pileup discrimination capability. Our tests demonstrated that pure CsI + SiPMs design assisted by a fast analog electronics and a digitisation at 200 Msps can largely satisfy Mu2e requirement.

There are many other demanding requests to be satisfied by this detector, such as to keep the required performance in presence of 1 T axial magnetic field, in an evacuated region and in a radiation

harsh environment. The CsI crystals will withstand the expected dose and fluence with a small light yield loss [12]. The Mu2e SiPMs will work under neutron irradiation when cooled at 0 °C [13], thus asking for a good engineering design of the calorimeter mechanics and of its cooling system. Test on single crystals and SiPMs demonstrates the required technical specifications can be reached.

The schedule is to start assembly the first calorimeter disk in winter 2018 and complete the construction in 2020.

Acknowledgment

This work was supported by the EU Horizon 2020 Research and Innovation Program under the Marie Sklodowska-Curie Grant Agreement No.690385.

References

1. L. Bartoszek et al., (Mu2e experiment), *Mu2e Technical Design Report* arXiv:1501.05241.
2. R. Donghia on behalf of the Mu2e Collaboration, *The Mu2e experiment at Fermilab: Design and status*, Nuovo Cimento 40 C 176 (2017).
3. N. Atanov et al., *Design, status and test of the Mu2e crystal calorimeter*, JoP: Conference Series, Vol. 928, conference 1 (2016).
4. BABAR Collaboration, *The BABAR detector*, NIM A A479, pp. 1-116 (2002).
5. N. Atanov et al., *The Mu2e calorimeter: QA of production crystals and SiPMs and results from Module-0 test beam*, submitted to NIM A.
6. N. Atanov et al., *ELECTRONICS*, submitted to NIM A.
7. N. Atanov et al., *Quality Assurance on Un-Doped CsI Crystals for the Mu2e Experiment*, IEEE Trans. Nucl. Sci. 65, 752-757 (2017).
8. N. Atanov et al., *Quality Assurance on a custom SiPMs array for the Mu2e experiment* NSS-MIC (2017).
9. M. Cordelli er al., *Pre-production and quality assurance of the Mu2e calorimeter Silicon Photomultipliers*, NIM A submitted to Elsevier (2017).
10. O. Atanova et al.,*Measurement of the energy and time resolution of a undoped CsI + MPPC array for the Mu2e experiment*, JINST 12 P05007 (2017).
11. A.M. Baldini et al., *A cryogenic facility for testing the PMTs of the MEG liquid xenon calorimeter*, NIM A 566 294-301 (2016).
12. S. Baccaro et al.,*Irradiation study of UV Silicon Photomultipliers for the Mu2e Calorimeter*, JINST 12 C02022 (2017).
13. M. Cordelli et al., *Neutron irradiation test of Hamamatsu, SensL and AdvanSiD UV-extended SiPMs*, JINST 13 T03005 (2018).

Frascati Physics Series Vol. 67 (2018)
6th Young Researcher Workshop 'Physics Challenges in the LHC Era'
May 7 and 10, 2018

ρ-MESON LEPTOPRODUCTION AS TESTFIELD FOR THE UNINTEGRATED GLUON DISTRIBUTION IN THE PROTON

Andrèe Dafne Bolognino
Dipartimento di Fisica dell'Università della Calabria I-87036 Arcavacata di Rende, Cosenza, Italy
INFN - Gruppo collegato di Cosenza, I-87036 Arcavacata di Rende, Cosenza, Italy
Francesco Giovanni Celiberto
Instituto de Fiśica Teórica UAM/CSIC, Nicolás Cabrera 15, 28049 Madrid, Spain
Universidad Autónoma de Madrid, 28049 Madrid, Spain
Dmitry Yu. Ivanov
Sobolev Institute of Mathematics, 630090 Novosibirsk, Russia
Novosibirsk State University, 630090 Novosibirsk, Russia
Alessandro Papa
Dipartimento di Fisica dell'Università della Calabria I-87036 Arcavacata di Rende, Cosenza, Italy
INFN - Gruppo collegato di Cosenza, I-87036 Arcavacata di Rende, Cosenza, Italy

Abstract

The gluon content of the proton is embodied by the unintegrated gluon distribution (UGD), which has universal validity. In literature many models of UGD have been proposed so far. The polarized ρ-meson leptoproduction at HERA offers a nowadays unexplored textfield to discriminate among existing models of UGD, via the comparison with theoretical predictions formulated in the κ-factorization approach.

1 Introduction

Our ability to find New Physics at the LHC strongly relies on getting a more and more precise understanding of the structure of the proton. In approaches based on the theoretical study of collision processes, the information about the proton structure is encoded in the partonic distribution functions entering the *factorized* expression for the cross section. At small x the proper factorization scheme is given by κ-*factorization*, whereby the Deep Inelastic Scattering (DIS) cross section is represented as the convolution of the unintegrated gluon distribution (UGD) in the proton with the (perturbative) impact factor (IF) for the $\gamma^* \to \gamma^*$ transition. The UGD is a nonperturbative quantity, function of x and κ, where the latter represents the gluon momentum transverse to the direction of the proton. The UGD, in its original definition, obeys the BFKL [1] evolution equation in the x variable. The UGD is not well known and several models for it, which lead to very different shapes in the (x, κ)-plane, have been proposed so far (see, for instance, Ref. [2]).

The aim of this work is to present some arguments that HERA data on polarization observables in vector-meson (VM) electroproduction can be used to constrain the κ-dependence of the UGD in the HERA energy range. In particular, we will focus our attention on the *ratio* of the two dominant amplitudes for the polarized electroproduction of ρ mesons, *i.e.* the longitudinal VM production from

longitudinally-polarized virtual photons and the transverse VM production from transversely-polarized virtual photons.

The paper is organized as follows: in Section 2 we will present the expressions for the amplitudes of interest here and sketch the main properties of a few models for the UGD; in Section 3 we compare theoretical predictions from the different models of UGD with HERA data; in Section 4 we draw our conclusions.

2 Theoretical setup

The H1 and ZEUS collaborations have provided useful and complete analyses of the hard exclusive production of the ρ meson in ep collisions through the subprocess

$$\gamma^*(\lambda_\gamma)p \to \rho(\lambda_\rho)p\,. \tag{1}$$

Here λ_ρ and λ_γ represent the meson and photon helicities, respectively, and can take the values 0 (longitudinal polarization) and ± 1 (transverse polarizations). The helicity amplitudes $T_{\lambda_\rho\lambda_\gamma}$ extracted at HERA [3] exhibit the following hierarchy [4]:

$$T_{00} \gg T_{11} \gg T_{10} \gg T_{01} \gg T_{-11}. \tag{2}$$

The H1 and ZEUS collaborations have analyzed data in different ranges of Q^2 and W. In what follows we will refer only to the H1 ranges,

$$\begin{aligned} 2.5\,\mathrm{GeV}^2 < Q^2 < 60\,\mathrm{GeV}^2, \\ 35\,\mathrm{GeV} < W < 180\,\mathrm{GeV}, \end{aligned} \tag{3}$$

and will concentrate only on the dominant helicity-amplitude ratio, T_{11}/T_{00}.

2.1 Electroproduction of polarized ρ mesons in κ-factorization

In the high-energy regime, $s \equiv W^2 \gg Q^2 \gg \Lambda^2_{\mathrm{QCD}}$, which implies small $x = Q^2/W^2$, the forward helicity amplitude for the ρ-meson electroproduction can be written, in κ-factorization, as the convolution of the $\gamma^* \to \rho$ IF, $\Phi^{\gamma^*(\lambda_\gamma)\to\rho(\lambda_\rho)}(\kappa^2, Q^2)$, with the UGD, $\mathcal{F}(x,\kappa^2)$. Its expression reads

$$T_{\lambda_\rho\lambda_\gamma}(s,Q^2) = \frac{is}{(2\pi)^2}\int \frac{d^2\kappa}{(\kappa^2)^2}\Phi^{\gamma^*(\lambda_\gamma)\to\rho(\lambda_\rho)}(\kappa^2,Q^2)\mathcal{F}(x,\kappa^2), \quad x = \frac{Q^2}{s}\,. \tag{4}$$

The expressions for the IFs, for the longitudinal and the transverse cases, take the form given by Eq. (33) and Eq. (38) in Ref. [6]. In particular, the longitudinal IF encompasses the twist-2 distribution amplitude (DA) [5]; while the transverse IF is defined using DAs which encompass both genuine twist-3 and Wandzura—Wilczek (WW) contributions [5, 7]. In this work we focus on the WW contributions and then we relax this approximation including the genuine parts. Moreover, for the sake of semplicity, we have adopted the *asymptotic* choice for the twist-2 DA (for further details see Section 2.2 of Ref. [8]).

2.2 Models of Unintegrated Gluon Distribution

A selection of six UGD models has been considered, without pretension to exhaustive coverage, but with the aim of comparing different approaches. We refer the reader to the original papers for details on the derivation of each model and limit ourselves to presenting here just the functional form $\mathcal{F}(x,\kappa^2)$ of the UGD, as we implemented it in the numerical analysis.

2.2.1 An x-independent model (ABIPSW)

The simplest UGD model is x-independent and merely coincides with the proton impact factor [7]:

$$\mathcal{F}(x,\kappa^2) = \frac{A}{(2\pi)^2\, M^2}\left[\frac{\kappa^2}{M^2+\kappa^2}\right], \tag{5}$$

where M corresponds to the non-perturbative hadronic scale. The constant A is unessential since we are going to consider the ratio T_{11}/T_{00}.

2.2.2 Gluon momentum derivative

This UGD is given by

$$\mathcal{F}(x,\kappa^2) = \frac{d[xg(x,\kappa^2)]}{d\ln\kappa^2} \tag{6}$$

and encompasses the collinear gluon density $g(x,\mu_F^2)$, taken at $\mu_F^2=\kappa^2$. It is based on the obvious requirement that, when integrated over κ^2 up to some factorization scale, the UGD must give the standard gluon density.

2.2.3 Ivanov–Nikolaev' (IN) UGD: a soft-hard model

The UGD proposed in Ref. [9] is developed with the purpose of probing different regions of transverse momentum. In the large-κ region, DGLAP parametrizations for $g(x,\kappa^2)$ are employed. Moreover, for the extrapolation of the hard-gluon densities to small κ^2, an Ansatz is made [10], which describes the color gauge-invariance constraints on the radiation of soft gluons by color-singlet targets. The gluon density at small κ^2 is supplemented by a non-perturbative soft component, according to the color-dipole phenomenology.

This model of UGD has the following form:

$$\mathcal{F}(x,\kappa^2) = \mathcal{F}_{\rm soft}^{(B)}(x,\kappa^2)\frac{\kappa_s^2}{\kappa^2+\kappa_s^2} + \mathcal{F}_{\rm hard}(x,\kappa^2)\frac{\kappa^2}{\kappa^2+\kappa_h^2}\,, \tag{7}$$

We refer the reader to Ref. [9] for an exaustively discussion on the features, the parameters and on the expressions of the soft and the hard terms. We stress that this model was successfully tested on the *unpolarized* electroproduction of VMs at HERA.

2.2.4 Hentschinski-Salas–Sabio Vera (HSS) model

This model, originally used in the study of DIS structure functions [11], takes the form of a convolution between the BFKL gluon Green's function and a LO proton impact factor. It has been employed in the description of single bottom-quark production at LHC in [12] and to investigate the photoproduction of J/Ψ and Υ in [13]. We implemented the formula given in [12] (up to a κ^2 overall factor needed to match our definition), which reads

$$\mathcal{F}(x,\kappa^2,M_h) = \int_{-\infty}^{\infty}\frac{d\nu}{2\pi^2}\,\mathcal{C}\,\frac{\Gamma(\delta-i\nu-\frac{1}{2})}{\Gamma(\delta)}\,\left(\frac{1}{x}\right)^{\chi\left(\frac{1}{2}+i\nu\right)}\left(\frac{\kappa^2}{Q_0^2}\right)^{\frac{1}{2}+i\nu} \tag{8}$$

$$\times\left\{1+\frac{\bar{\alpha}_s^2\beta_0\chi_0\left(\frac{1}{2}+i\nu\right)}{8N_c}\log\left(\frac{1}{x}\right)\left[-\psi\left(\delta-\frac{1}{2}-i\nu\right)-\log\frac{\kappa^2}{M_h^2}\right]\right\},$$

where $\beta_0 = (11N_c - 2N_f)/3$, with N_f the number of active quarks, $\bar{\alpha}_s = \alpha_s\left(\mu^2\right) N_c/\pi$, with $\mu^2 = Q_0 M_h$, and $\chi_0(\frac{1}{2} + i\nu)$ is the LO eigenvalue of the BFKL kernel. Here, M_h plays the role of the hard scale which can be identified with the photon virtuality, $\sqrt{Q^2}$. In Eq. (8), $\chi(\gamma)$ is the NLO eigenvalue of the BFKL kernel, collinearly improved and employing BLM method for the scale fixing given as in Section 2 of Ref. [12].

This UGD model is described through three parameters Q_0, δ and $\mathcal{C}$ which characterize a peculiar parametrization for the proton impact factor (see Ref. [12] for further details). We adopted here the so called *kinematically improved* values (see Section III A of Ref. [8] for further details).

2.2.5 Golec-Biernat–Wüsthoff' (GBW) UGD

This UGD parametrization derives from the effective dipole cross section $\sigma(x, r)$ for the scattering of a $q\bar{q}$ pair off a nucleon [14], through a Fourier transform and reads

$$\mathcal{F}(x, \kappa^2) = \kappa^4 \sigma_0 \frac{R_0^2(x)}{8\pi} e^{\frac{-k^2 R_0^2(x)}{4}} . \tag{9}$$

We refer to Ref. [14] for the details and discussion of the parameters of this model.

2.2.6 Watt–Martin–Ryskin' (WMR) model

The UGD introduced in [15] reads

$$\mathcal{F}(x, \kappa^2, \mu^2) = T_g(\kappa^2, \mu^2) \frac{\alpha_s(\kappa^2)}{2\pi} \int_x^1 dz \left[\sum_q P_{gq}(z) \frac{x}{z} q\left(\frac{x}{z}, \kappa^2\right) + P_{gg}(z) \frac{x}{z} g\left(\frac{x}{z}, \kappa^2\right) \Theta\left(\frac{\mu}{\mu + \kappa} - z\right) \right] , \tag{10}$$

where the term $T_g(\kappa^2, \mu^2)$, whose expression is given in Ref. [15], gives the probability of evolving from the scale κ to the scale μ without parton emission. This UGD model depends on an extra-scale μ, which we fixed at Q.

3 Numerical analysis

In this Section we present our results for the helicity-amplitude ratio T_{11}/T_{00}, as obtained with the six UGD models presented above, and compare them with HERA data.

In Fig. 1 we compare the Q^2-dependence of T_{11}/T_{00} for all six models at $W = 100$ GeV, together with the experimental result.

We used here the asymptotic twist-2 DA ($a_2(\mu^2) = 0$) and the WW approximation for twist-3 contributions. Theoretical results are spread over a large interval, thus supporting our claim that the observable T_{11}/T_{00} is potentially able to strongly constrain the κ-dependence of the UGD. None of the models is able to reproduce the data over the entire Q^2 range; the x-independent ABIPSW model and the GBW model seem to better catch the intermediate-Q^2 behavior of data.

To gauge the impact of the approximation made in the DAs, we calculated the T_{11}/T_{00} ratio with the GBW model, at $W = 35$ and 180 GeV, by varying $a_2(\mu_0 = 1 \text{ GeV})$ in the range from 0 to 0.6 and properly taking into account its evolution. Moreover, for the same UGD model, we relaxed the WW approximation in T_{11} and considered also the genuine twist-3 contribution. All that is summarized in

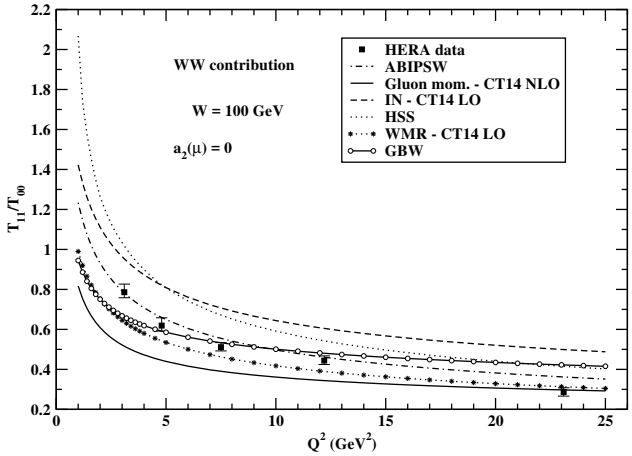

Figure 1: *Q^2-dependence of the helicity-amplitude ratio T_{11}/T_{00} for all the considered UGD models at $W = 100$ GeV. In the twist-2 DA we have put $a_2(\mu_0 = 1\ GeV) = 0$ and the T_{11} amplitude has been calculated in the WW approximation.*

Fig. 2, which indicates that our predictions for the helicity amplitude ratio are rather insensitive to the form of the meson DAs.

The stability of T_{11}/T_{00} under the lower cut-off for κ, in the range $0 < \kappa_{\min} < 1$ GeV, has been investigated. This is a fundamental test since, if passed, it underpins the main underlying assumption of this work, namely that *both* helicity amplitudes considered here are dominated by the large-κ region. In Fig. 3 we show the result of this test for the GBW model at $W = 100$ GeV; similar plots can be obtained with the other UGD models. There is a clear indication that the small-κ region gives only a marginal contribution.

We refer to Section 3.1 of Ref. [8] for details on the numerical implementation and on the systematic uncertainty estimation.

4 Conclusions

In this paper we have proposed the helicity amplitudes for the electroproduction of vector mesons at HERA (and in possible future electron-proton colliders) as a nontrivial testfield for models of the unintegrated gluon distribution in the proton.

We have given some theoretical arguments, supported by a detailed numerical analysis, that both transverse and longitudinal cases are dominated by the kinematic region where small-size color dipoles interact with the proton. Moreover, we have shown that some of the most popular models for the unintegrated gluon distribution in the literature give very sparse predictions for the ratio of the transverse-to-longitudinal production amplitude.

References

1. V.S. Fadin, E.A. Kuraev, L.N. Lipatov, Phys. Lett. **B60** (1975) 50; E.A. Kuraev, L.N. Lipatov and V.S. Fadin, Zh. Eksp. Teor. Fiz. **71** (1976) 840 [Sov. Phys. JETP **44** (1976) 443]; **72** (1977) 377 [**45** (1977) 199]; Ya.Ya. Balitskii and L.N. Lipatov, Sov. J. Nucl. Phys. **28** (1978) 822.

2. J.R. Andersen *et al.* [Small x Collaboration], Eur. Phys. J. C **48** (2006) 53 [hep-ph/0604189]; Eur.

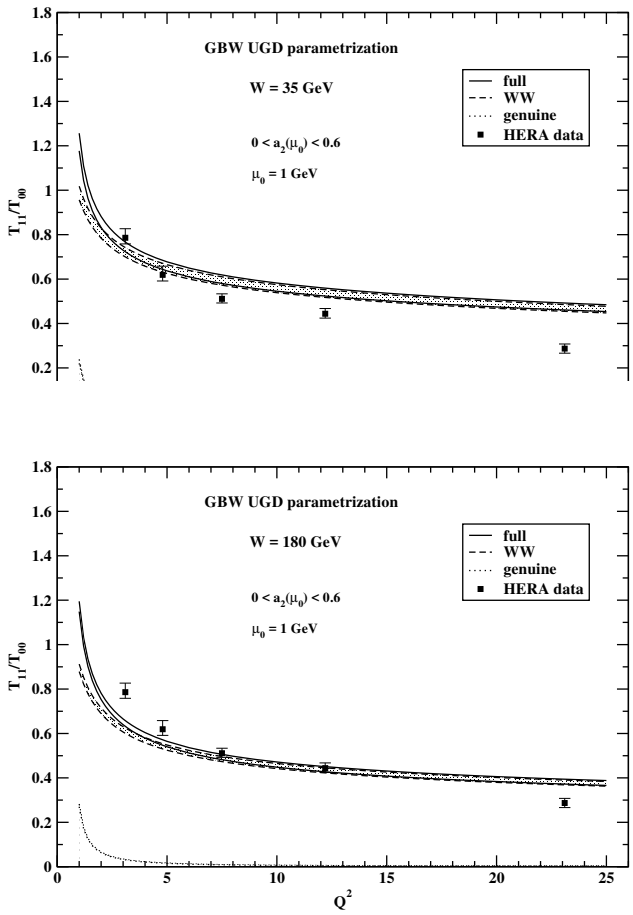

Figure 2: *Q^2-dependence of the helicity-amplitude ratio T_{11}/T_{00} for the GBW UGD model at $W = 35$ (left) and 180 GeV (right). The full, WW and genuine contributions are shown. The bands give the effect of varying $a_2(\mu_0 = 1\ GeV)$ between 0. and 0.6.*

Phys. J. C **35** (2004) 67 [hep-ph/0312333]; B. Andersson *et al.* [Small x Collaboration], Eur. Phys. J. C **25** (2002) 77 [hep-ph/0204115].

3. F.D. Aaron *et al.* [H1 Collaboration], JHEP **1005** (2010) 032 [arXiv:0910.5831 [hep-ex]].

4. D.Yu. Ivanov and R. Kirschner, Phys. Rev. D **58** (1998) 114026 [hep-ph/9807324].

5. P. Ball, V.M. Braun, Y. Koike and K. Tanaka, Nucl. Phys. B **529** (1998) 323 [hep-ph/9802299].

6. I.V. Anikin, D.Yu. Ivanov, B. Pire, L. Szymanowski and S. Wallon, Nucl. Phys. B **828** (2010) 1 [arXiv:0909.4090 [hep-ph]].

7. I.V. Anikin, A. Besse, D.Yu. Ivanov, B. Pire, L. Szymanowski and S. Wallon, Phys. Rev. D **84** (2011) 054004 [arXiv:1105.1761 [hep-ph]].

8. A.D. Bolognino, F.G. Celiberto, D.Yu. Ivanov, A. Papa, in progress.

9. I.P. Ivanov, N.N. Nikolaev, Phys. Rev. D **65** (2002) 054004 [hep-ph/0004206].

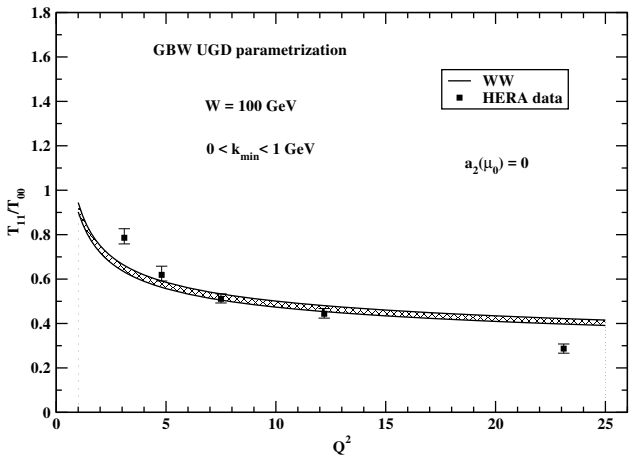

Figure 3: *Q^2-dependence of the helicity-amplitude ratio T_{11}/T_{00} for the GBW UGD model at $W = 100$ GeV. The band is the effect of a lower cutoff in the κ-integration, ranging from 0. to 1 GeV. In the twist-2 DA we have put $a_2(\mu_0 = 1\ GeV) = 0$ and the T_{11} amplitude has been calculated in the WW approximation.*

10. N.N. Nikolaev, B.G. Zakharov, Phys. Lett. B **332** (1994) 177 [hep-ph/9403281]; Z. Phys. C **53** (1992) 331.

11. M. Hentschinski, A. Sabio Vera, C. Salas, Phys. Rev. Lett. **110** (2013) no.4, 041601 [arXiv:1209.1353 [hep-ph]].

12. G. Chachamis, M. Deák, M. Hentschinski, G. Rodrigo, A. Sabio Vera, JHEP **1509** (2015) 123 [arXiv:1507.05778 [hep-ph]].

13. I. Bautista, A. Fernandez Tellez, M. Hentschinski, Phys. Rev. D **94** (2016) no.5, 054002 [arXiv:1607.05203 [hep-ph]].

14. K.J. Golec-Biernat, M. Wusthoff, Phys. Rev. D **59** (1998) 014017 [hep-ph/9807513].

15. G. Watt, A.D. Martin, M.G. Ryskin, Eur. Phys. J. C **31** (2003) 73 [hep-ph/0306169].

Frascati Physics Series Vol. 67 (2018)
6th Young Researcher Workshop 'Physics Challenges in the LHC Era'
May 7 and 10, 2018

VERIFYING THE PERFORMANCE OF THE ARGON-41 MONITORING SYSTEM FROM FLUORINE-18 PRODUCTION FOR MEDICAL APPLICATIONS

Nicole Virgili
Sapienza University of Rome, Department of Nuclear Engineering, Rome, Italy

Abstract

The aim of this work is to determine the detection efficiency of a Geiger–Muller detector placed in the terminal part of the chimney of the TR19PET cyclotron for environmental monitoring of ^{41}Ar emission (activity) through the chimney of the TR19PET cyclotron (19 MeV), installed at A. Gemelli University Hospital (Roma, IT) and routinely used in the production of positron-emitting radionuclides.

1 Introduction

In the medical field, cyclotrons are used both in diagnostics and therapy: in diagnostics they are used in the production of radioactive isotopes used, in particular, as tracers for Positron Emission Tomography (PET) [1]. The aim of this work is to characterize, from a radioprotection point of view, the emission of the radioactive gases following the production of the ^{18}F-FDG radiopharmaceutical by proton irradiation through the TR19PET cyclotron and to determine the detection efficiency of the Geiger–Muller detector through the use of Monte Carlo (MC) code MCNP. In a medical cyclotron facility, ^{41}Ar ($t_{1/2}$ = 109.34 m) is produced by the activation of air due to the neutron flux during irradiation, according to the $^{40}Ar(\mathrm{n},\gamma)^{41}Ar$ reaction. This is particularly relevant in widely diffused high-beam current cyclotrons for the production of PET radionuclides, ^{18}F radionuclide in this case.

2 Cyclotron TR19PET

The TR19PET system is composed of cyclotron, cabinet of power supply and control system, cooling units and local shielding (in order to reduce at the source level the radiant beams emitted). The TR19PET cyclotron, produced by ACSI [2], is an isochronus compact and accelerates negative ions H^- in a plan

vertically disposed up to a maximum energy of 19 MeV. ^{18}F-fluorine ion, the most used for PET in the form of ^{18}F-FDG radiopharmaceutical, is produced in water solution through the nuclear reaction ^{18}O(p,n)^{18}F. Once produced, the radionuclide (^{18}F) must be bound to a suitable molecule acting as a transporter, the FDG (Fluorodeoxyglucose) to create ^{18}F-FDG radiopharmaceutical, which accumulates in points of interest [3, 4, 1].

3 Problems following Fluorine-18 production

The main problems are due to: 1. The radionuclidic impurities of the irradiated (^{18}O) water, originated by the (^{18}F) FDG synthesis process [5]; 2. the ^{41}Ar ($t_{1/2}$ = 109.34 m) produced by the activation of air due to the neutron flux during irradiation, according to the ^{40}Ar(n,γ)^{41}Ar reaction [6]. The second problem is that the only exothermic reaction without threshold is the one wherein the neutron is captured by ^{40}Ar with the consequent production of ^{41}Ar. The natural concentration of argon-40 in air is 0.93% per volume. The argon-41 (half-life 109.2 minutes) emits β-radiation with a maximum energy of 1198 MeV and gamma rays of 1294 keV. The region of resonances is in the range between 10 keV and 15 MeV. In cyclotrons without their own shielding, most of the argon-41 inside the bunker air is produced by neutrons thermalized by the bunker concrete walls. The description with a 3D geometry of the FLUKA MC geometric model of the TR19 cyclotron, the cyclotron vault and the ducts through the vault walls (SimpleGeo and Flair) has been made by Infantino [7, 8]. Neutrons are generated with energy around 1 MeV and then slowed down to thermal energy with a peak around 4×10^{-7} MeV. Considering only the cross section value related to neutrons of energy 0.025 eV, the production of ^{41}Ar is understimated.

4 Geiger–Muller detector

The detector is placed within the internal wall of the terminal part of the cyclotron chimney with measure range from 0.1 μSv/h to 1 Sv/h[1] and energy range from 30 keV to >1 MeV. The cone geometry, as seen from the detector, has been used in order to estimate through the MCNP code the detector efficiency related to the activity of argon-41 in the cone. The following plume Gaussian model of dispersion in the environment has been used to describe the concentration in air C [MBq/m^3] at receptor level [5]:

$$C = \frac{Q}{2\pi\sigma_y\sigma_x\overline{u}} \exp\left\{-\frac{1}{2}\left[\frac{y}{2\sigma_y^2} + \frac{(z-h)^2}{2\sigma_z^2}\right]\right\}, \tag{1}$$

where x is the linear distance of the receptor, Q the emission rate [MBq/s], h the effective level of release, $\overline{u}$ the wind mean speed at release level, y the transverse distance of receptor from plume axis, z the receptor height at ground level, σ_y and σ_x the distribution standard deviations within the cloud along the trasverse and vertical directions, respectively. The measurements are evaluated assuming that the release effective height is equal to that of the chimney release (25 m), the receptor at ground level is located at variable distances of 100, 200, 300 m, the plant collocation is considered within an urban area. Finally, the wind evaluations are carried out at release level for a critical group of population, that is assumed to be located underwind, considering a costant wind direction in different climate conditions.

[1]The sievert (Sv) is a unit of ionizing radiation in the International System of Units, corresponding to 1 Sv= 1 J/kg.

5 Experimental measurements

The noble inert gas ^{41}Ar is only of local interest (sommersion) because of its rapid decay and it affects both skin (β particles) and internal organs (γ rays). The ^{41}Ar considered herein has a β electron-capture (EC) decay, a half-life $t_{1/2} = 1.8$ h and a decay constant $\lambda = 1.054\ 10^{-4} s^{-1}$. Moreover, the following data are considered: $A = 700$ Bq/μA (activity produced in air by ^{41}Ar), $I = 50\ \mu A$ (current intensity of the beam), $\lambda = 1.054\ \times 10^{-4} s^{-1}$ (decay constant). Two cases have been analysed herein: with and without air changes.

- Case 1: Without air changes
  Activity produced in air in Bq:

$$A_{produced} = 700\ \frac{\text{Bq}}{\mu\text{A}}\ 50\ \mu A = 35000\ \text{Bq}; \tag{2}$$

  Number of nuclei produced:

$$N = \frac{A}{\lambda} = \frac{35000}{1.054 \times 10^{-4}} = 3.32 \times 10^{8} \text{Bq s}; \tag{3}$$

  Maximum activity in 1 hour:

$$A_{max} = 35000 \times 3600 = 1.26 \times 10^{8}\ \text{Bq}. \tag{4}$$

  Calculating the number of nuclei produced according to the law of radioactive decay, which, in addition to the decay term of the previous batch, also includes a second production term of the current batch, one obtains:

$$N = N_0 e^{-\lambda \Delta t} + \frac{A}{\lambda}\left(1 - e^{-\lambda \Delta t}\right)\ \text{[atomi]}. \tag{5}$$

  Setting the time in intervals of 10 seconds each and considering

$$A = \lambda \times N\ \text{[Bq]}, \tag{6}$$

  one obtains the graph in Fig. 1.

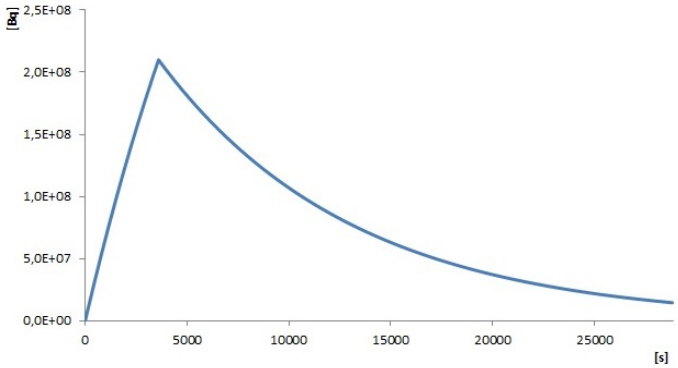

Figure 1: *Activity of* ^{41}Ar *vs. Time*

- Case 2: With air changes

  In this case the following data are considered: bunker volume $V_{cyclo} = 177.1$ m^3, branching ratio $b = 0.99157$, chimney diameter = 83 cm, area = 0.541 m^2, velocity during irradiation = 0.273 m/s, velocity during no irradiation = 0.100 m/s and irradiation time = 60 min. Moreover, a cone geometry has been considered, hypothesizing a height $h = 2$ m and a volume $V_{cone} = 1.08$ m^3, both seen by the detector:

$$Air\ changes\ rate\ (during\ irradiation) = \frac{2V_{cyclo}}{h} = 0.0148\ \frac{\mathrm{m}^3}{\mathrm{s}}, \tag{7}$$

$$Air\ changes\ rate\ (no\ irradiation) = \frac{a.c.r.\ (irr.)}{3} = 0.049\ \frac{\mathrm{m}^3}{\mathrm{s}}, \tag{8}$$

  where *a.c.r.(irr.)* is the air-change rate during the irradiation.

  The calculation of the detector efficiency through the use of MCNP, with cps standing for counts per second, proceeds along the following steps:

$$\epsilon = 4.72 \times 10^{-7}\ \frac{\mathrm{cps}}{\mathrm{Bq}}, \tag{9}$$

$$N_{expelled} = 2.77 \times 10^{7}\ \ [atomi]\,, \tag{10}$$

  where the number of expelled and recycled nuclei is calculated as:

$$N_{expelled} = \left[N_0 \exp^{-\lambda\Delta t} + \frac{A}{\lambda}\left(1 - \exp^{-\lambda\Delta t}\right)\right] \times \frac{V_{air\ changes}}{V_{cyclo}} \times \Delta t, \tag{11}$$

$$N_{recycled} = N_0 - N_{expelled} = 3.32 \times 10^9 - 2.77 \times 10^7 = 3.3 \times 10^9\,[\mathrm{atomi}]\,. \tag{12}$$

  Consequently, the expelled and recycled activities are calculated according to the following steps:

$$A_{expelled} = \lambda \times N_{expelled} = 3 \times 10^3\,[\mathrm{Bq}]\,, \tag{13}$$

$$A_{recycled} = \lambda \times N_{recycled} = 1.054 \times 10^{-4} \times 3.3 \times 10^9 = 3.47 \times 10^5\,[\mathrm{Bq}]\,, \tag{14}$$

$$\frac{A_{expelled}}{air\ changes\ rate} = \frac{3 \times 10^3}{0.148} = 20270.3. \tag{15}$$

  The activity potentially visible reads:

$$A_{potentially\ visible} = A_{expelled} \times \frac{v \times \Delta t}{H_{seen\ by\ detector}} = 27668.96\ \mathrm{Bq}. \tag{16}$$

  Figure 2 presents the activity of ^{41}Ar inside the cyclotron (left) and the activity of the expelled ^{41}Ar (right) with respect to time:

$$\frac{\mu Sv}{h} = \frac{1.3 \times 10^{-2}}{1939.129} \times 1000 = 6.68 \times 10^{-3}\frac{\mu Sv}{h}. \tag{17}$$

  At last, the counting rate is given by:

$$R = \epsilon b A_{potentially\ visible} = 1.3 \times 10^{-2}. \tag{18}$$

  Figure 3 presents the counts per second (left) and the counting rate per hour ($\mu Sv/h$, right), as seen by the detector, as a function of time.

  Finally, in Figure 4 one can see the optimized counts per second, after monitoring the emitted activity.

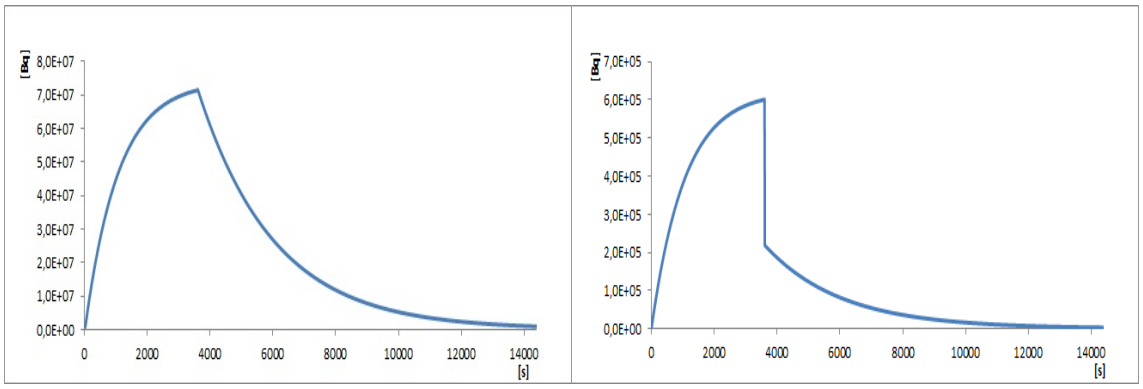

(a) Graph 1 (b) Graph 2

Figure 2: *Graph 1: Activity ^{41}Ar inside cyclotron vs. Time; Graph 2: Activity ^{41}Ar expelled vs. Time*

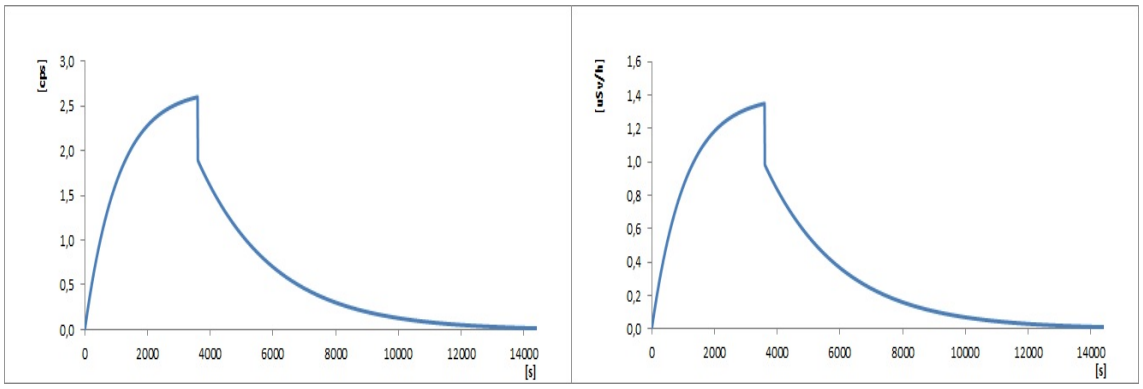

(a) Graph 1 (b) Graph 2

Figure 3: *Graph 1 cps seen by detector; Graph 2 $\mu Sv/h$ seen by detector*

6 Conclusions

In conclusion, the detection efficiency determined through the use of Monte Carlo codes is very low (4.7 $\times 10^{-7}$ cps/Bq), and the counting rate of 1.3 $\times 10^{-2}$ is low as well. Consequently, in normal operating conditions, the detector does not produce any signal and gives a totally inefficient contribution related to its functions. Other monitoring systems are currently being studied by our research team in order to achieve a greater efficiency, finalized to the radiological impact assessment.

7 Acknowledgements

I would like to thank my collaborators Professor R. Remetti ("Sapienza University of Rome Italy, Department of Energetics) and Dr. L. Indovina (Physics Department, University Hospital "A. Gemelli" Rome, Italy) for the work presented here and the organisers of the 6th Young Researchers Workshop: Physics Challenges in the LHC Era for the invitation.

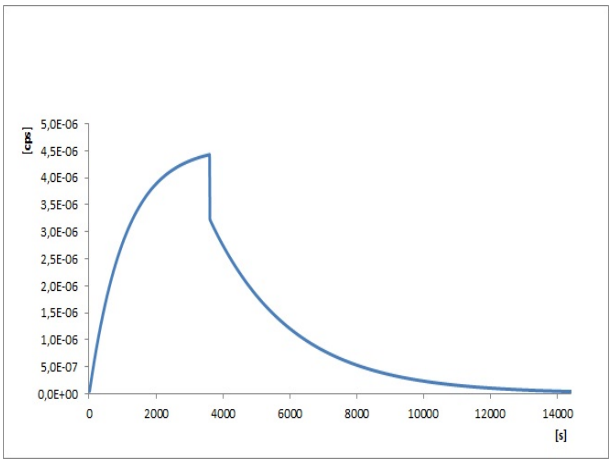

Figure 4: *Counting rate optimized monitoring activity emitted*

References

1. Bonardi M., 1987. The contribution to nuclear data for biomedical radioisotope production. Tokyo, Japan, Internation Atomic Energy Agency (IAEA), pp. 98-112.

2. ACSI, 2014, TR19 PET Cyclotron, Operating and Maintenance Manual Rev. 5.0. Richmond, BC, Canada: Advanced Cyclotron System Inc. (ACSI).

3. Rocha A. F. C. and Harbert J. C., Textbook of Nuclear Medicine Clinical Application,Lea and Febiger 1979 Philadelphia.

4. Schmor, P. W., 2010, Review of cyclotrons used in the production of radioisotopes for biomedical applications, Lanzhou, s.n., pp. 419-424.

5. Remetti R., Burgio N. T., Maciocco L., Arcese M. and Filannino M.A., *Monte Carlo simulation and radiometric characterization of proton irradiated [^{18}O]H_2O for the treatment of the waste streams originated from [^{18}F]FDG synthesis process*, Applied Radiation and Isotopes 69 (2011) 10461051.

6. Birattari, C., Bonardi, M., Ferrari, A. and Silari, M., 1985, Neutron activation of air by a biomedical cycltron and an assessment of dose to neighbourhood populations. Radiation Protection Dosimetry, 14(4), pp. 311-319.

7. Biju, K., Sunil, C. and Sakar, P. K., 2013. Estimation of 41Ar production in 01-1.0 GeV proton accelerator vaults using FLUKA Monte Carlo code. *Radiation Protection Dosimetry*, 157(3), pp. 437-441.

8. Infantino A., Valtieri L., Cicoria G., Pancaldi D., Mostacci D. and Marengo M., *Experimental measurement and Monte Carlo assessment of Argon-41 production in a PET cyclotron facility*, PhysicaMedica31 (2015) 991996.

Frascati Physics Series Vol. 67 (2018)
6th Young Researcher Workshop 'Physics Challenges in the LHC Era'
May 7 and 10, 2018

SEARCH FOR NEUTRAL LONG-LIVED PARTICLES DECAYING TO LEPTON-JETS WITH THE ATLAS DETECTOR IN p-p COLLISION DATA AT $\sqrt{s} = 13$ TeV

Cristiano Sebastiani
Università di Roma 'La Sapienza' and INFN, Sezione di Roma

Abstract

Several new physics models that extend the Standard Model require the existence of Long-Lived Particles (LLP) as a solution for problems like Dark Matter or Naturalness. In this scenario neutral LLPs decaying to collimated jets of leptons and light hadrons (lepton-jets) are of great interest. The present reports the latest results in the search of displaced lepton-jets with the ATLAS experiment [1)] at the proton-proton LHC collider at $\sqrt{s} = 13$ TeV.

1 Introduction

Many different proposed models and theories beyond the Standard Model predict the existence of long-lived particles (LLP). Most of these models include hidden sectors coupled to the visible one, resulting in an unconventional signature that can lead to an early discovery. Searches are detector-based depending on the LLP lifetime, which can range form few μm to several meters outside the ATLAS detector. The study here presented aims at searching for neutral LLP particles which decay far from the interaction point and therefore only the calorimetric detectors and the muon spectrometer will be considered. These signatures represent a great challenge for both trigger and reconstruction capabilities of the ATLAS detector, which is designed for prompt searches.

2 Benchmark models

In this study a dark-sector vector-portal model with a dark photon as a mediator is assumed. The benchmark model considered is the Falkowski–Ruderman–Volansky–Zupan (FRVZ) model [2)]. This model presents a final state with two light 400 MeV dark photons decaying to SM via kinetic mixing.

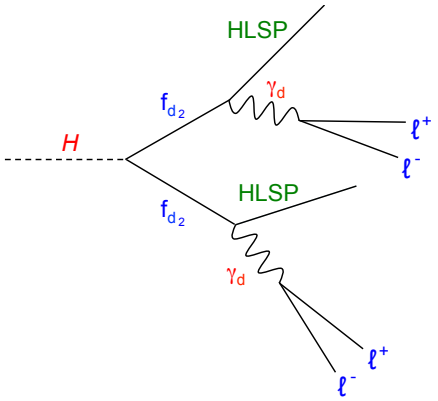

Figure 1: *The γ_d production together with a hidden light stable particle from a Higgs hidden decay chain for the FRVZ benchmark model. The γ_d are boosted objects decaying into displaced collimated structures*

The single dark photon is produced by a 125 GeV SM Higgs boson (or alternatively a BSM heavy Higgs boson) decay chain together with a light hidden stable particle (LHSP), Fig. 1. In this model the dark-photon (γ_d) branching ratio (BR) depends on its mass. For example, considering a mass of 400 MeV, γ_d decays 45% of the time into pairs of electrons or muons and 10% into pairs of pions. The mean lifetime is a free parameter of the model.

At the LHC these light dark photon are produced with a large boost, resulting in collimated structures containing pair of leptons or light hadrons called lepton-jets.

3 Lepton-jet selection

The reconstruction of a lepton-jet depends on the decay channel of the dark photon. A cluster of collimated muons in the Muon Spectrometer is a signature of one or more γ_d decaying to muons. A displaced jet in the calorimeters with no tracks in the inner detectors is a signature of a displaced γ_d decaying to pions or electrons. Therefore the reconstructed lepton-jets are classified in three different types according to the number of muons and jets found within a ΔR opening cone, as shown schematically in Fig. 2:

- Type 0 (Muonic-LJ) - At least two muons and no jets are found.
- Type 1 (Mixed-LJ) - At least two muons and a jet are found. This is a typical signature of a multiple dark photon model.
- Type 2 (Hadronic-LJ) - A jet and no muons are found.

To select muonic-LJ events a dedicated multi-muon trigger that requires muons reconstructed only in the muon spectrometer is adopted. For the selection of hadronic LJs a single jet trigger with a low electromagnetic fraction is used, in order to select displaced jets that decay mostly in the hadronic calorimeter.
This search selects events with two back-to-back reconstructed lepton-jets and straight cuts are applied on each LJ of the pair according to its type. These cuts are studied to reduce the background events coming from the cosmic-ray muons for the muonic LJ and the QCD multi-jet dominant background for

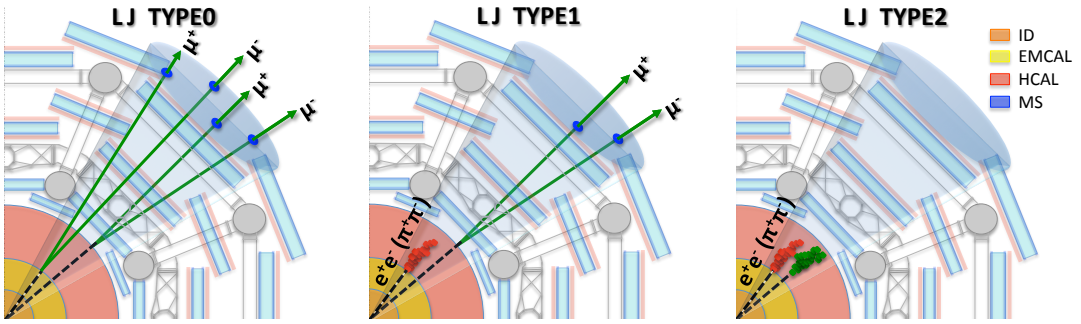

Figure 2: *Schematic picture of the lepton-jet classification according to the decay final state. Only muons (Type 0), mixed (Type 1) and only jets (Type 2).*

the hadronic LJ. For the cosmic background timing and impact-parameter detector variables are used. For the QCD multi-jet background cuts are applied on the electromagnetic fraction and width of the jet. The surviving events are used to fill the ABCD planes, as a function of two final discriminant variables: the isolation in the inner detector ($\sum P_T$) and the opening angle between the two LJs ($\Delta\Phi$).
The ABCD method is then used to estimate the QCD multi-jet dominant background in the signal region (high $|\Delta\Phi|$ and low $\sum p_T$).

4 Results

No excess was found and the expected yield was consistent with the observed one. An upper limit on $\sigma \times \mathrm{BR}(H \to \gamma_d\gamma_d + X)$ is then set at 95% CL as a function of the dark-photon mean lifetime.
The results are shown in Fig. 3 for both SM Higgs (left) and 800 GeV BSM Higgs. The expected (dashed) and the observed (solid) limits are shown for different values of the Higgs-boson branching fractions (horizontal lines) to dark photons.

Finally, these results are interpreted in the context of a vector-portal model. This is presented in Fig. 4 on a parameter-space exclusion contour plot for dark photons as a function of the γ_d mass and of the kinetic mixing parameter ϵ, expressing the coupling between QED and dark-photon fields, assuming different Higgs-decay branching fractions to invisible particles.

References

1. G. Aad et al., *The ATLAS Experiment at the CERN Large Hadron Collider*, JINST, 3:S08003, 2008.

2. A. Falkowski, J. T. Ruderman, T. Volansky and J. Zupan, JHEP 05 (2010) 77.

3. *Search for long-lived neutral particles decaying into displaced lepton jets in proton-proton collisions at* $\sqrt{s} = 13$ *TeV with the ATLAS detector*, Technical Report ATLAS-CONF-2016-042, CERN, Geneva, Aug 2016.

4. G. Aad et al., *Search for long-lived neutral particles decaying into lepton jets in proton-proton collisions at* $\sqrt{s} = 8$ *TeV with the ATLAS detector*, JHEP 11 (2014) 088.

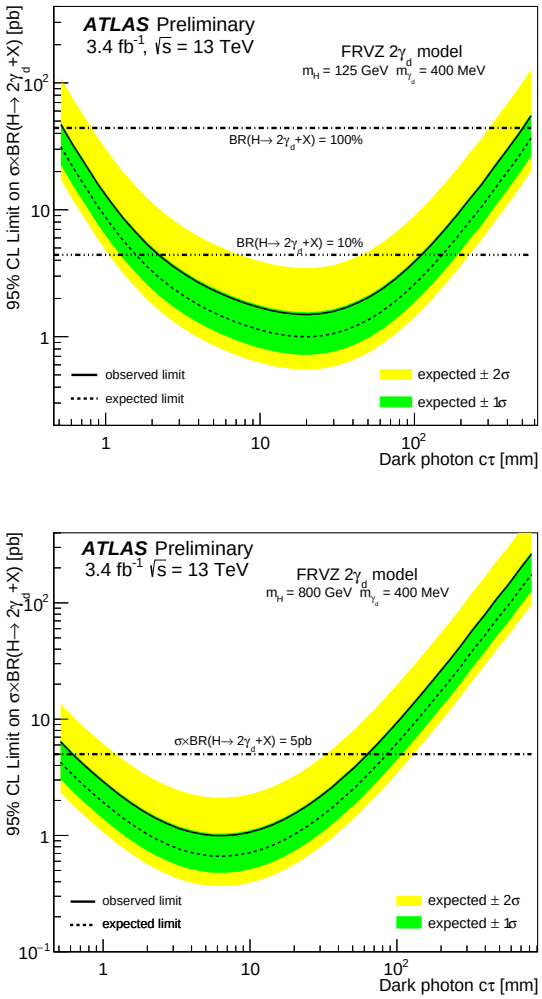

Figure 3: *95% upper limits on* $\sigma \times \mathrm{BR}$ *for the process* $H \to \gamma_d\gamma_d + X$*, considering a SM Higgs (top) or a* 800 *GeV BSM Higgs (bottom). The limit is presented as a function of the* γ_d *mean lifetime* $c\tau$ *for the FRVZ benchmark samples. The horizontal lines correspond to* $\sigma \times BR$ *for two values of the BR of the Higgs-boson decay to dark photons* [3].

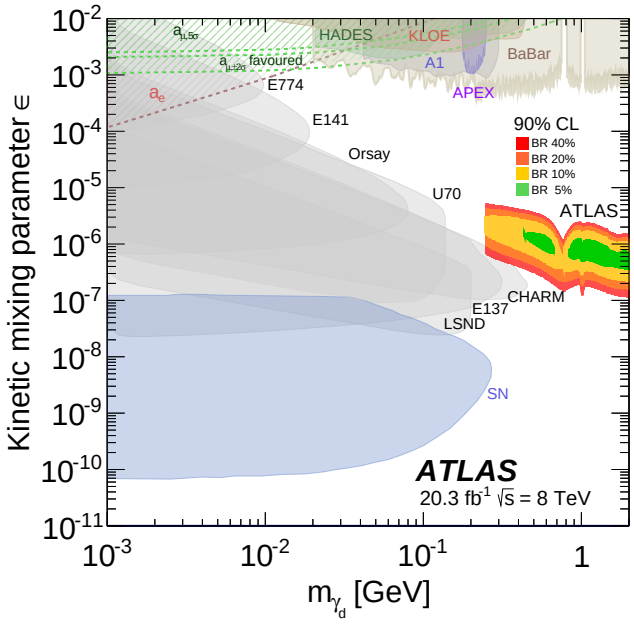

Figure 4: *Parameter-space exclusion plot for dark photons as a function of the γ_d mass and of the kinetic mixing parameter ϵ. Also shown are the 90% CL exclusion limits from the present ATLAS search, assuming the FRVZ model and $H \to \gamma_d\gamma_d + X$ decays with branching fractions of 5/10/20/40%* [4].

Frascati Physics Series Vol. 67 (2018)
6th Young Researcher Workshop 'Physics Challenges in the LHC Era'
May 7 and 10, 2018

MUON RECONSTRUCTION AND IDENTIFICATION IN THE ATLAS EXPERIMENT AT LHC

D. Vannicola [a,b]
[a] *Sapienza University, Rome*
[b] *INFN, Sezione di Roma*

Abstract

This article documents the performances of the ATLAS muon identification and reconstruction, using the LHC dataset recorded at $\sqrt{s} = 13$ TeV in 2015. Results on the reconstruction efficiency measured using a large sample of $J/\Psi \to \mu\mu$ and $Z \to \mu\mu$ decays from 3.2 fb^{-1} of proton-proton (pp) collision data, are presented and compared to Monte Carlo simulations.

1 Introduction

Muons play a fondamental role in the most important physics results published by the ATLAS experiment [1)] at the LHC. The discovery of the Higgs boson [2)], the precise measurements of Standard Model processes [3)] and the searches for physics beyond the Standard Model [5)] prove how muons are really important in physics. In this article, after describing the ATLAS muon-reconstruction and identification algorithms, also measurements of the reconstruction efficiency, obtained using samples of $J/\Psi \to \mu\mu$ and $Z \to \mu\mu$ decays from 3.2 fb^{-1} of pp collision data recorded in 2015, are presented as well. The comparison between data and MC simulation is also discussed.

2 ATLAS detector

The ATLAS detector presents an onion structure and consists of three different subdetectors:

- the inner detector (ID), close to the interaction point, is the innermost ATLAS subdetector, designed to detect muons in the pseudorapidity region up to $|\eta| < 2.5$;

- the lead/liquid-argon electromagnetic calorimeter covers $|\eta| < 3.2$, surrounded by hadronic calorimeters made of steel and scintillator tiles for $|\eta| < 1.7$, and copper or tungsten and liquid argon for $|\eta| > 1.7$;

- the muon spectrometer (MS) is the outermost ATLAS subdetecor and covers a pseudorapidity range up to $|\eta| < 2.7$.

The ID consists of three subdetectors: the silicon pixels (Pixel), the semiconductor tracker (SCT), with a pseudorapidity coverage up to $|\eta| = 2.5$, and the transition radiation tracker (TRT). The ID detectors are located inside an axial magnetic field of 2 T, and this allows an accurate measurement of the muon track parameters. The MS is designed to identify muons in the pseudorapidity range up to $|\eta| < 2.7$, with a momentum resolution better than 3% for muons with a transverse momentum (p_T) smaller than 200 GeV. It is made of 3 sections: one barrel ($|\eta| < 1.05$), and two endcaps ($1.05 < |\eta| < 2.7$). In the MS there are four different subdetecors: the resistive plate chambers (RPC), located in the barrel, the thin gap chamber (TGC), in the endcap, the monitored drift tube (MDT) and the cathode strip chamber (CSC). RPC and TGC are used to identify the bunch crossing and to provide the trigger, while a precise momentum measurement is provided by three layers of MDT (spatial resolution ~ 80 μm) in the region $|\eta| > 2$. Only in the first layer the MDT is replaced by the CSC. A system of three large superconducting air-core toroidal magnets provides a magnetic field with a bending integral of about 2.5 Tm in the barrel and up to 6 Tm in the endcaps, respectively. The muon chambers are aligned with a precision between 30 μm and 60 μm.

3 Muon reconstruction

In this section it will be described the tecnique used to reconstruct a muon. It depends on different muon parameters, such as the value of the η coordinate and of the momentum, but also on the detector involved in the muon identification. First of all, each muon is indipendently reconstructed in the ID and in the MS; concerning the calorimeter, the most useful information is related to the energy deposit left in the calorimeters by the muon. After that, all this information is combined to reconstruct the muon track as best as possible.

3.1 Combined reconstruction

The combined muon reconstruction is performed according to various algorithms, based on the information provided by ID, MS and calorimeters. Four muon types are defined depending on which subdetectors are used in the reconstruction:

- Combined (CB) muons: this tecnique needs the information from ID and MS, after that muon track reconstruction is first indipendently performed in the two subdetectors and then the information will be combined. The hits from both ID and MS are fiited, in order to get the combined muon track.

- Segment-tagged (ST) muons: this tecnique is used to detect muons with low p_T, that are not able to reach the outer MDT layer in the MS due to the magnetic field, so a track detected in the ID is associated with a muon if, once extrapolated to the MS, there is at least one local track segment in the MDT or CSC layer that matches with the extrapolated track.

- Calorimeter-tagged (CT) muons: this algorithm is useful to identify muon in the pseudorapity range $|\eta| < 0.1$, where the MS is not efficient due to geometrical vetoes. A track in the ID is classified as a muon if it can be macthed to an energy deposit in the calorimeter compatible with the one left from a minimun ionizing particle.

- Extrapolated (ME) muons: they are used to recover the acceptance in the region $2.5 < |\eta| < 2.7$, where the ID is not able to work. After reconstructing the track in the MS, a compatibilty with the interaction point is the only requirement to identify this track as a muon. The muon parameters are defined considering the energy deposit in the calorimeter.

4 Muon identification

In this section a dedicated description of the criteria used to selected muons with the highest possible efficiency and purity is reported. The q/p significance, where q and p are the charge and momentum of the muons, respectively, is a very powerful variable used to discriminate the good muons from the others, and is defined in the following way:

$$(q/p)_{\text{significance}} = \frac{|q/p|_{\text{MS}} - |q/p|_{\text{ID}}}{\sigma_{q/p}}. \quad (1)$$

In Eq. 1, $|q/p|_{\text{ID}}$ is the charge-to-momentum-ratio measured by the Inner Detector and $|q/p|_{\text{MS}}$ is the same measured by the MS. $\sigma_{q/p}$ is the sum in quadrature of the corresponding uncertainties.

Different physics analyses need different requirements, so four different selections are provided: medium, loose, tight and high-p_T. The loose, medium and tight selections are inclusive, so muons included in the tight working point are also included in the medium and loose categories.

- Medium: this is the most common selection used in the ATLAS physics analyses. Only CB adn ME muons are included; it is required at least three hits on two precision MDT or CSC layers.

- Loose: this category is used to increase the reconstruction efficiency and all muon types are used. All CB and ME muons that passed the medium selection are included; ST and CT muons are restricted in region $|\eta| < 0.1$, which is not covered by the MS.

- Tight: the aim of this working point is to maximise the purity of the muons, only CB able to satisfy the medium requirements are considered, a cut based on the q/p significance is also applied to reject the backgorund as much as possible.

- High-p_T: this is the last selection, made to maximise the momentum resolution for muons with a p_T larger than 200 GeV. CB muons that passed the medium selection and have hits on the three precision layers are the only ones that belong to this group.

5 Muon reconstruction efficiency

In this section, after a short description of the data sets and MC samples used in this study, the muon reconstruction efficiency as a function of η, for the different categories discussed in the section before, is showed. A comparison with the MC samples is reported too. As far as data sets are concerned, we have considered $Z \to \mu\mu$ and $J/\Psi \to \mu\mu$ events reconstructed from pp collisions at $\sqrt{s} = 13$ TeV, recorded at LHC in 2015. MC samples for the process $pp \to X(Z/\gamma^*) \to X\mu\mu$ are generated using the POWHEG BOX [8] interfaced to PYTHIA 8 [9] and CT10 [10] parton distribution functions. All MC samples are

Table 1: *Efficiency for prompt muons from W decays and hadrons decaying in flight. Possible misidentification of prompt muons, computed using a $t\bar{t}$ MC sample, is accounted for. The results are shown for the four identification criteria considering the p_T range* 20 GeV $< p_T <$ 100 GeV. *The statistical uncertainties are negligible.*

	20 GeV $< p_T <$ 100 GeV	$20 < p_T <$ 100 GeV
Selection	$\epsilon_{\mu}^{\mathrm{MC}}$[%]	$\epsilon_{\mathrm{hadrons}}^{\mathrm{MC}}$[%]
Loose	98.1	0.76
Medium	96.1	0.17
Tight	91.8	0.11
High-p_T	80.4	0.13

passed through the simulation of the ATLAS detector based on GEANT4 [11] and are reconstructed with the same tecniques used for the data. An accurate determination of the muon-reconstruction efficiency is obtained with the tag-and-probe method [12]. In Table 1 it is reported a comparison between the efficiencies for prompt muons and hadrons decaying in flight, accounting for possible misidentification of prompt muons by using a $t\bar{t}$ MC sample. The results for the four different working point (medium, loose, tight and high-p_T) are presented. In Fig.(1) it is illustrated the muon-reconstruction efficiency trend as a function of η: this result is obtained considering reconstructed muons, with a p_T spectrum from 4 to 100 GeV. Loose and medium categories have a costant efficiency close to 98%, except in the region $|\eta| < 0.1$, where the medium selection, due to MS geometrical vetoes, leads a value of 60%. Muons selected with the tight criteria have the same problems as the medium ones, and in the region $|\eta| < 0.1$ the efficiency is around 55%, while in the other ranges of $|\eta|$ the trend is almost constant around 94%.

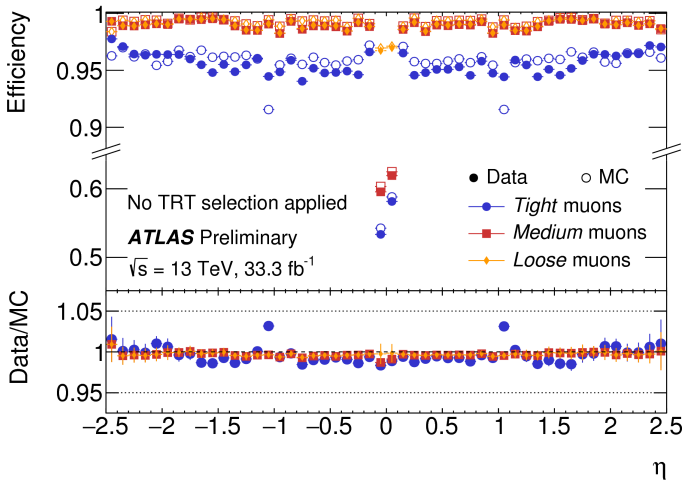

Figure 1: *Muon-reconstruction efficiency trend, as a function of η, for three different selections (loose, medium and tight). A comparison with MC simulations is also shown.*

6 Conclusion

The performance of the ATLAS muon reconstruction has been measured using 3.2 fb^{-1} of data from pp collisions at $\sqrt{s} = 13$ TeV recorded during the 25 ns run at the LHC in 2015. The muon-reconstruction

efficiency is close to 99% over most of the pseudorapidity range $|\eta| < 2.5$ for $p_T > 5$ GeV. The $Z \to \mu\mu$ sample enables a measurement of the efficiency with a precision at the 0.2% level for $p_T > 20$ GeV. The $J/\Psi \to \mu\mu$ sample provides a measurement of the reconstruction efficiency for transverse momenta between 5 and 20 GeV with a precision better than 1%.

References

1. ATLAS Collaboration, The ATLAS Experiment at the CERN Large Hadron Collider, JINST 3 (2008) S08003.

2. ATLAS Collaboration, Observation of a new particle in the search for the Standard Model Higgs boson with the ATLAS detector at the LHC, Phys. Lett. B716 (2012) 129, arXiv:1207.7214 [hep-ex].

3. ATLAS Collaboration, Measurement of the transverse momentum and $\phi\,\eta$ distributions of Drell-Yan lepton pairs in proton-proton collisions at $\sqrt{s} = 8$ TeV with the ATLAS detector, Eur. Phys. J. C76 (2016) 291, arXiv:1512.02192 [hep-ex].

4. ATLAS Collaboration, Measurement of the ZZ Production Cross Section in pp Collisions at $\sqrt{s} =$ 13 TeV with the ATLAS Detector, Phys. Rev. Lett. 116 (2016) 101801, arXiv:1512.05314 [hep-ex].

5. ATLAS Collaboration, Search for high-mass dilepton resonances in pp collisions at $\sqrt{s} = 8$ TeV with the ATLAS detector, Phys. Rev. D90 (2014) 052005, arXiv:1405.4123 [hep-ex].

6. ATLAS Collaboration, Search for new particles in events with one lepton and missing transverse momentum in pp collisions at $\sqrt{s} = 8$ TeV with the ATLAS detector, JHEP09 (2014) 037, arXiv:1407.7494 [hep-ex].

7. ATLAS Collaboration, Combination of searches for WW, WZ, and ZZ resonances in pp collisions at $\sqrt{s} = 8\ TeV$ with the ATLAS detector, Phys. Lett. B755 (2016) 285, arXiv:1512.05099 [hep-ex].

8. S. Alioli et al., A general framework for implementing NLO calculations in shower Monte Carlo programs: the POWHEG BOX, JHEP06 (2010) 043, arXiv:1002.2581 [hep-ph].

9. T. Sjöstrand, S. Mrenna and P. Skands, A brief introduction to PYTHIA 8.1, Comput. Phys. Commun. 178 (2008) 852, arXiv:0710.3820 [hep-ph].

10. H.-L. Lai et al., New parton distributions for collider physics, Phys. Rev. D82 (2010) 074024, arXiv:1007.2241 [hep-ph].

11. S. Agostinelli et al., Geant4, a simulation toolkit, Nucl. Instrum. Meth. A506 (2003) 250.

12. ATLAS Collaboration, Muon reconstruction performance of the ATLAS detector in protonproton collision data at $\sqrt{s} = 13$ TeV, Eur. Phys. J. C76 (2016) 292.

Frascati Physics Series Vol. 67 (2018)
6th Young Researcher Workshop 'Physics Challenges in the LHC Era'
May 7 and 10, 2018

SEARCH FOR NEW PHENOMENA IN DIJET EVENTS WITH THE ATLAS DETECTOR AT LHC

Simone Francescato
University of Rome "La Sapienza" and INFN, Sezione di Roma

Abstract

Final states with two jets represent one of the main channels when searching for new phenomena in high-energy experiments, because of the high statistics. Dijets events are recorded by ATLAS during the Run2 period at the centre-of-mass energy of 13 TeV. Invariant-mass and angular distributions are analyzed and compared to Standard Model background predictions, seeking for evidence of New Physics signals over the dominant QCD contribution. Information from the dijet angular correlations has been deployed to improve the sensitivity towards broad resonances. Results are interpreted in the context of Standard Model extensions, focusing on a particular dark-matter model.

1 Introduction

New phenomena beyond the Standard Model (SM) are expected to exist, given the large number of measurements and observations in various sectors of physics.
The existence of an extra component of matter in the Universe is one of the major unknowns in the current understanding of the Universe. From cosmological observations, this kind of matter should not be interacting with SM particles via electromagnetism or strong force but only via gravity: in this sense this matter is dark [1].
The assumption that the Universe is filled with dark matter (DM) is supported by a large number of astrophysical observations: the rotational speed of stars in galaxies, the gravitational lensing measurements and so on. The Cosmic Microwave Background (CMB) spectrum measurement gives also an estimate of the amount of DM in the Universe. However, the nature and properties of DM remain largely unknown. Searches for DM can be performed using different and complementary approaches summarized in Figure 1: the measurement of elastic scattering of DM with nuclei, the detection of SM particles produced

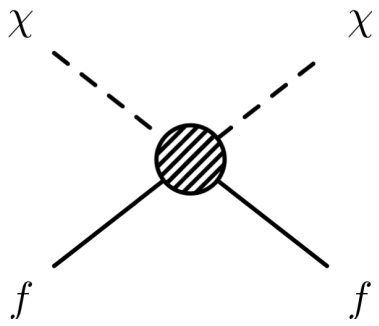

Figure 1: General scheme summarizing Dark Matter detection processes: changing the arrow of time one can obtain direct detection experiment, indirect detection of dark matter and dark matter production at colliders.

in the annihilation of DM or the production of DM particles at colliders. The content of the vertex in Figure 1 specifies the model used to describe DM.

In the context of DM searches at collider experiments, it is possible to assume that DM is made of weakly-interacting massive particles (WIMPs). Furthermore, it can be assumed that WIMPs are Dirac fermions which are pair-produced in the LHC pp collisions. These particles, denoted with the symbol χ, are assumed to be invisible for the detector. One needs to rely on an object X in order to tag the events and measure recoiling WIMPs as missing transverse momentum (E_T^{miss}). The visible object can come from initial-state radiation or from a more complex decay chain producing the WIMPs, depending on the model considered. If DM candidates can be produced at the LHC through an s-channel mediator, then this mediator could also decay back to SM particles: resonance searches can hence be used to investigate DM. The interplay of resonance and $X + E_T^{\text{miss}}$ searches depends heavily on the model and couplings considered.

A rich experimental programme of searches for DM models is performed by the ATLAS experiment using 13 TeV proton-proton collisions data collected in 2015-2016. One of the most used DM model is a simplified $U(1)$-type extension of the SM, in which a DM fermion candidate can interact with SM particles only via a massive-vector mediator. This model is powerful due to the low number of free parameters (see Section 3 for a more complete description). In this framework, final states with two jets represent an important channel for a mediator-based search.

2 The ATLAS detector

The ATLAS experiment [2] at the LHC [3] is a multipurpose particle detector with a forward-backward symmetric cylindrical geometry with layers of tracking, calorimeter and muon detectors over nearly the entire solid angle around the pp collision point. The directions and energies of high-p_T hadronic jets are measured using silicon tracking detectors and a transition radiation straw-tube tracker, hadronic and electromagnetic calorimeters, and a muon spectrometer. Hadronic-energy measurements are provided by a calorimeter with scintillator active layers and steel absorber material for the pseudorapidity range $|\eta| < 1.7$, while electromagnetic (EM) energy measurements are provided by a calorimeter with liquid-argon (LAr) active material and lead-absorber material covering the pseudorapidity range $|\eta| < 3.2$. The endcap and forward regions, extending up to $|\eta| = 4.9$, are instrumented with LAr calorimeters for both EM and hadronic-energy measurements. The lower-level trigger is implemented in hardware and uses a subset of

the detector information to reduce the accepted rate to 100 kHz. This is followed by a software- based high-level trigger that reduces the rate of events recorded to 1 kHz.

3 Vector/axial-vector mediator

One of the most powerful models considered in several DM searches is a simplified model with a single spin-1 particle that composes a new mediator sector [4]. This model is a natural extension of the SM via the simplest gauge symmetry and provides a scenario to describe a portal from SM to DM sector.
This new mediator is assumed to be a vector or an axial-vector and arises from an additional $U(1)$ gauge symmetry. The new mediator is called Z'. The model has only five free parameters: the masses of the mediator and of the DM particle, the coupling of the Z' boson to quarks g_q, leptons g_ℓ (both are assumed to be flavour universal) and DM g_χ. Since DM particles are invisible to detectors by construction, searches can only look for the additional mediator. It is possible to look for Z' decays to either a pair of quarks or a pair of leptons, defining the so-called dijet or dilepton searches, respectively [5, 6]. If the Z' decays to a pair of DM particles, an additional visible object X has to be produced, e.g. a jet or a photon from initial-state radiation (ISR), defining the so-called mono-X searches. Several scenarios for the parameters are recommended, in order to highlight the complementarity of all these searches, for both vector and axial-vector couplings. It is possible to write the most general interaction lagrangian for Z' mediator as:

$$\mathcal{L}^{Z'} = \sum_{f=q,\ell} Z'_\mu \, \bar{f} \, \gamma^\mu (g_f^V - g_f^A \, \gamma^5) f + Z'_\mu \, \bar{\chi} \, \gamma^\mu (g_\chi^V - g_\chi^A \gamma^5) \chi, \tag{1}$$

with index V for the vector couplings and A for the axial-vector ones. The partial decay width of this mediator are:

$$\begin{aligned} \Gamma(Z' \to \chi\bar{\chi}) &= \frac{M_{Z'}}{12\pi} \sqrt{1 - 4\, z_\chi} \, \left[(g_\chi^V)^2 + (g_\chi^A)^2 + z_\chi \left(2(g_\chi^V)^2 - 4(g_\chi^A)^2 \right) \right] \, , \\ \Gamma(Z' \to f\bar{f}) &= \frac{M_{Z'} \, N_c}{12\pi} \sqrt{1 - 4\, z_f} \, \left[(g_f^V)^2 + (g_f^A)^2 + z_f \left(2(g_f^V)^2 - 4(g_f^A)^2 \right) \right] \, , \end{aligned} \tag{2}$$

with $z_{\chi,f} = m_{\chi,f}^2 / M_{Z'}^2$, $N_c = 3$ for quarks and $N_c = 1$ for leptons.

4 Dijet searches

Given the theoretical framework described in the previous Section, a dijet search for high-mass mediators can be used to set constraints on the Z'. Since previous dilepton searches excluded a great part of the phase space of this model, it is convenient to set $g_\ell = 0$. For sake of simplicity, since the region of interest for $m_{Z'}$ is 1-10 TeV, it is useful to set also the mass of the DM particle to high values, e.g. $m_\chi = 10$ TeV, in order to suppress kinematically the decay into a DM pair. The goal is to produce a 2D scan in the $g_q - m_{Z'}$ plane, putting a limit on such a mediator, if no significant deviations are observed.
The dijet analysis is based on the reconstruction of two high-energy jets in the final state. Possible new-physics signals are expected to be visible as a resonance peak in the dijet invariant-mass spectrum, over a smoothly falling background mainly due to t-channel jet production described by QCD. The resonance search is based on a fit of the dijet invariant-mass spectrum to the data, using an analytical function in sliding windows. A bump-hunter algorithm searches for significant peaks over the smoothly falling QCD background. The results of this analysis are reported in Figure 2: in the plot, observed and expected 95% confidence-level (CL) upper limits are shown [7]. The resonance search is bounded at low masses due to trigger constraints. Several techniques can be used to extend the exclusion curve: one can require

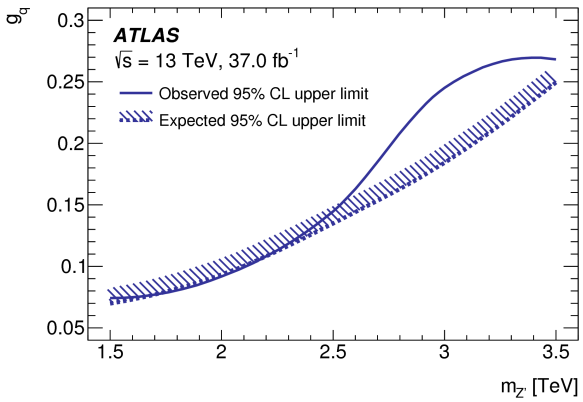

Figure 2: Observed and expected 95% CL upper limits on the Z' model the in $g_q - m_{Z'}$ plane, obtained with 37 fb^{-1} collected in 2015-2016 with the ATLAS detector [7].

a dijet final state with an additional ISR or perform the so-called dijet Trigger Level Analysis. Instead, at high mass the limitation comes from the fact that the dijet analysis is sensitive to the relative width of the Z' up to $\Gamma/m_{Z'} = 15\%$. Above this threshold, the resonance is so broad that all background-fitting techniques cannot distinguish the signal over the SM spectrum.
In order to improve the sensitivity of the analysis to broad resonances, additional information on the dijet system has to be used. Wider resonances would also modify the two-jet angular correlation, with excesses corresponding to central events, in contrast with more forward (-backward) events with jets closer to the beam axis.

5 Dijet angular analysis

As described before, the choice of the mediator mass and coupling affects the resonance position in the dijet invariant-mass spectrum and its width. For resonance widths up to 15% of the mass, the resonant search has been found to perform well. For widths greater than 15% of the mass, however, the background-fitting technique is not well behaving, due to the fact that the wider resonance is spread over a wide part of the spectrum. Studying the angular correlation between jets some conclusions can be drawn on the search for wider resonances. The sensitivity of the angular analysis towards wider resonances, corresponding to larger couplings of the mediator g_q, is currently being studied, with the goal to complement the other searches by probing the presence of an axial-vector mediator with masses larger than those explored by the resonance search.
The target of this search is the model phase space starting from A/V mediator masses of 2.5 TeV and coupling $g_q = 0.3$, for which the current result from the resonance search is quickly losing sensitivity. The focus on the region with $m_{jj} > 2.5$ TeV is motivated firstly by the trigger turn-on for the dijet angular pre-selection and secondly by the fact that a wider mediator signal at lower masses would have been detected by the standard dijet resonance searches, due to its significantly larger cross sections in this mass range.
The dijet angular variable considered is the Lorentz-invariant $\chi = e^{|y_1 - y_2|}$, where $y_{1,2}$ are the rapidities of leading and subleading jets. The strategy of this analysis is to perform a combined fit of χ in bins of m_{jj}, the invariant mass of the dijet system, in order to increase the sensitivity through a constraint

on the background contribution in different m_{jj} bins, which act as control regions. In such a fit, a dijet Monte Carlo (MC) simulation, corrected to next-to-leading order (NLO) theoretical predictions through event reweighting, is compared to the recorded data. As mentioned before, QCD processes are expected to be more abundant for small values of the polar angle θ in spherical coordinates [1].

The differential distribution $dN/d\chi$ is expected to be almost flat for SM events, besides NLO effects, and with a small logarithmic dependence on m_{jj}. In some sense, χ is the variable equivalent to the Rutherford scattering angle and its flatness represents the dominant contribution of t-channel processes. Events from an s-channel produced Z' mediator, in contrast, are expected to be more isotropic, resulting in an excess in the angular variable distribution at low χ values. One basic assumption of this fit strategy is to consider all the nuisance parameters corresponding to the systematic (described later in this paragraph) uncertainties as completely correlated in all m_{jj} windows. A strong constraint on the parameters corresponding to the background prediction is expected, in particular from high-statistics m_{jj} bins. This should help improving the sensitivity to the aforementioned mediator.

For each event it has been required that the highest unprescaled jet trigger, HLT_j380 is fired. This trigger has an efficiency greater than 99.5% for leading-jet transverse momenta $p_T > 428$ GeV, thus the leading jet is required to have a turn-on for $m_{jj} < 2500$ GeV: this has therefore to be considered as a lower bound for the analysis. In order to optimize the sensitivity, the conditions $y^* = |y_1 - y_2|/2 < 1.7$ and $y_B = |y_1 + y_2|/2 < 1.1$ are requested as well.

Since χ is a spatial variable, its binning has been decided on the basis of the detector granularity and spatial properties, with the upper bound depending on the y^* cut. The m_{jj} binning is motivated by the comparison of statistical and systematic uncertainties in each bin, and constrained by the binning of the NLO electroweak (EW) corrections evaluated by theorists (mentioned later in this paragraph). In Figure 3 angular distributions are shown as reported in the previous stage of this analysis for Contact Interaction (CI) models. With respect to previously published results, the phase space considered in the fit has been modified; the m_{jj} range has been extended by 900 GeV on the lower side of the spectrum to target lowest-mass Z' signals (while Contact Interaction signals are usually present in the high-mass region). MC background predictions are obtained via PYTHIA 8 [8] at LO, while Z' signals are produced with MadGraph5 [9]. SM predictions are corrected to include NLO effects applying to the angular distributions (in fixed bins of $\chi - m_{jj}$) some correction factors, containing NLO QCD and EW corrections. In this fit several systematic effects are included, due to both theoretical and experimental contributions. In particular, uncertainties on the Jet Energy Scale are considered. Jet Energy Resolution and η-Intercalibration non-closure effects are included, although less relevant. Non-negligible uncertainties come from theoretical assumptions: systematic uncertainties due to the choice of renormalization and factorization scales, PDFs and tuned parameters in the MC codes are taken into account. These uncertainties are reported in Figure 3 as shaded bands around the SM predictions, where it can be seen that theoretical uncertainties are dominating.

6 Conclusions

Even if the Standard Model is a self-consistent theory of the fundamental interactions, evidences for the existence of new phenomena are well supported by several observations in different field of physics. The explanation of Dark Matter and its properties is one the most questioning problem of modern physics.

[1] The rapidity y of a particle of energy E and momentum $\vec{p}$ is related to the angle θ with respect to the beam axis by the relation $y = \frac{1}{2} \ln \frac{E+|\vec{p}|\cos\theta}{E-|\vec{p}|\cos\theta}$.

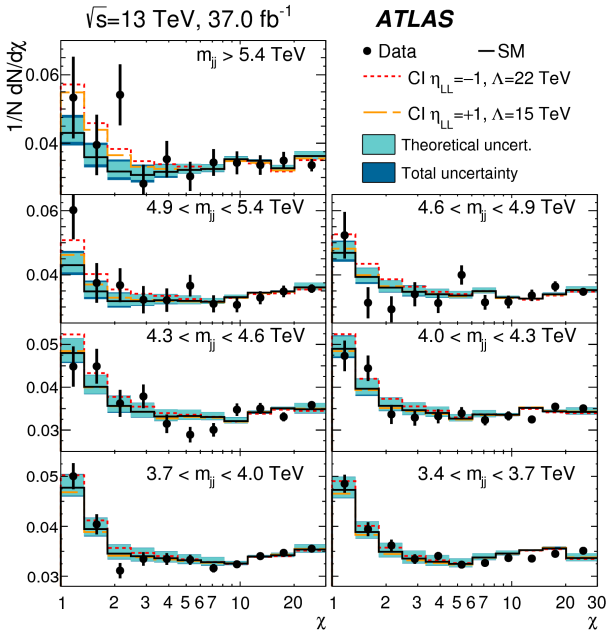

Figure 3: Distributions of the dijet angular variable χ in different regions of the dijet invariant mass m_{jj} for events with $|y| < 1.2$, $|y_B| < 1.1$ and $p_T > 440$ (60) GeV for the leading (subleading) jet [7]. The data (points), PYTHIA [8] predictions with NLO and EW corrections applied (solid lines), and several CI signals (red dashed lines) are shown. The theoretical uncertainties and the total theoretical and experimental uncertainties in the predictions are displayed as shaded bands around the SM prediction. Data and predictions are normalised in each m_{jj} bin.

Dark Matter can be assumed to exist as an elementary particle and thus it should be possible to observe indirectly its properties at colliders. More generally, the existence of a massive neutral mediator between the SM and the Dark Sector is a reasonable hypothesis. One can assume a simplified model in which this mediator, called Z', can mediate $2 \to 2$ s-channel processes with quarks in the final state, e.g. dijet events. Several analyses have been performed searching for high-mass resonances, looking at the final-state invariant mass. All these searches are limited and not effective for very broad resonances. In order to improve the sensitivity towards high-mass mediators with $\Gamma/m_{Z'} > 15\%$, information from the dijet angular correlations can be deployed. The idea is to perform a combined 2D fit in both angular and mass distributions. Standard Model differential distributions in the angular variable χ are expected to be flat; New Physics can then be seen as an excess at low χ. Studies are being performed, improving the previous strategy, and promising results are being achieved.

References

1. K. Garrett and G. Duda, Adv. Astron. **2011** (2011) 968283 [arXiv:1006.2483].
2. G. Aad *et al.* (ATLAS Collaboration), JINST **3** (2008) S08003.
3. L. Evans and P. Bryant, JINST **3** (2008) S08001.
4. D. Abercrombie *et al.*, [arXiv:1507.00966].

5. R. M. Harris and K. Kousouris, Int. J. Mod. Phys. A **26** (2011) 5005 [arXiv:1110.5302].

6. M. Chala, F. Kahlhoefer, M. McCullough, G. Nardini and K. Schmidt-Hoberg, JHEP **1507** (2015) 089 [arXiv:1503.05916].

7. M. Aaboud *et al.* (ATLAS Collaboration), Phys. Rev. D **96** (2017) 052004 [arXiv:1703.09127].

8. T. Sjostrand, S. Mrenna and P.Z. Skands, Comput. Phys. Commun. **178** (2008) 852 [arXiv:0710.3820].

9. J. Alwall *et al.*, JHEP **1407** (2014) 079 [arXiv:1405.0301].